THE SUN AND SUN-LIKE STARS

Gothard Astrophysical Observatory
Loránd Eötvös University

WORKSHOP ON

THE SUN AND SUN–LIKE STARS

9–11 AUGUST 1999
SZOMBATHELY, HUNGARY

PROCEEDINGS

Edited by I. Jankovics, J. Kovács and I.J. Vincze

SCIENTIFIC ORGANIZING COMMITTEE

Béla Szeidl (chair)

István Jankovics

Katalin Oláh

Lídia van Driel-Gesztelyi

LOCAL ORGANIZING COMMITTEE

István Jankovics (chair)

József Kovács

Ildikó Vincze

Loránd Eötvös University

Gothard Astrophysical Observatory

Szent Imre Herceg u. 112.

H-9707 Szombathely, Hungary

obs@gothard.hu

http://www.gothard.hu

Typesetting: Camera-ready by the authors/editors
Cover design: J. Kovács

Printed by Sylvester Ltd Company, Szombathely, Hungary

ISBN 963 00 3492 1

PostScript version is available at
http://www.gothard.hu/tse1999

Preface

The international workshop "The Sun and Sun-like stars" organised by Gothard Astrophysical Observatory took place 9-11 August 1999 in Szombathely, Hungary. The primary motivation to initiate this meeting was, that our observatory is located in the totality strip of the last total solar eclipse of the millennium on 11 August 1999. The workshop was also dedicated to the memory of Eugene von Gothard, the founder of the observatory, who died 90 years earlier.

Before this eclipse, the umbral shadow of the Moon last swept across Hungary in 1842 and next time it will come only in 2081. During the partial eclipse on 16 May 1882 Eugene von Gothard took a series of photographs of the Sun obscured by the Moon. His observatory was located far from the great scientific centres of that time, but his work in the field of astrophotography and the instrumentation made Gothard's name known throughout Europe.

The program of the workshop began on 8 August in the garden of the observatory. The participants unveiled two statues: statue of Eugene von Gothard (1857-1909) made by István Tóth and a statue by Elisabeth Ledersberger-Lehoczky named "Atrelios" was dedicated to this solar eclipse.

The workshop was officially opened the next morning by Dr. Emil Prugberger, Vice Mayor of Szombathely, who welcomed 33 participants from 8 countries.

During the course of two-day meeting 14 oral papers and numerous posters were presented on solar and stellar activity. The workshop discussed the important problems of coronal heating both from theoretical and observational points of view, the magnetic evolution and plasma dynamics of solar active regions, the relationship between magnetic loops of different temperatures, flare and CME activity, and the fine structure and modellisation of filaments. There were talks on solar-stellar analogies, modelling the Sun as a star, and the radiophysics of the solar corona.

The workshop was closed with a summary talk by K.D. Leka.

Each day ended with social programs and discussions focused on the problems of the stellar and solar activity.

Altough the early morning on 11 August was quite worrying for all of us because of the bad weather over Europe, the conditions changed very rapidly, and at the beginning of the partial phase we had good chances to observe the full eclipse. Unfortunately, the phase of the totality was slightly disturbed by a thin layer of clouds in Szombathely, but the sight will certainly remain an indelible and wonderful memory for all of our guests - astronomers, diplomats accredited to Hungary, local authorities - and many others.

We would like to thank Lídia van Driel-Gesztelyi, Katalin Oláh and Brigitte Schmieder for their help in organizing and running the workshop.

We are very grateful for the generous financial support received from the Ministry of Education, Loránd Eötvös University, the National Committee for Technological Development, Council of Szombathely, Alexander von Humboldt Foundation, Council of County Vas, and Gothard Astrophysical Observatory Foundation.

Finally, we would like to thank all the workshop participants for the stimulating atmosphere they fostered during the workshop and their contributions to the proceedings.

The Editors

Statue of Eugene von Gothard and "Atrelios"

Table of contents

List of participants

Spiro Antiochos
Code 7675, Naval Research Laboratory, Washington DC, 20375-5352, USA

János Bartus
Konkoly Observatory, Budapest, Pf. 67, H-1525, Hungary

Bob Bentley
Mullard Space Science Laboratory, University College London
Holmbury St. Mary, Dorking, Surrey RH5 6NT, UK

Péter Berczik
Main Astronomical Observatory, Ukrainian National Academy of Sciences
Golosiiv, Kiev-022, Ukraine, 252650

János Bergou
Hunter College, Manhattan, New York

Pascal Démoulin
Observatoire de Paris, DASOP/LPSH
5, Place Jules Janssen, F-92195 Meudon Cedex, France

Lídia van Driel-Gesztelyi
Observatoire de Paris, DASOP/LPSH
5, Place Jules Janssen, F-92195 Meudon Cedex, France

Wim van Driel
Observatoire de Paris, Unite Scientifique de Nancay
5, Place Jules Janssen, F-92195 Meudon Cedex, France

Louise Harra
Mullard Space Science Laboratory, University College London
Holmbury St. Mary, Dorking, Surrey RH5 6NT, UK

István Jankovics
Gothard Observatory, Szombathely, Szent Imre Herceg u. 112., H-9707, Hungary

Ádám Kiss
Ministry of Education, Budapest

József Kovács
Gothard Observatory, Szombathely, Szent Imre Herceg u. 112., H-9707, Hungary

László Kovács
Berzsenyi Dániel Teacher Training College, Dept. of Physics
Szombathely, Berzsenyi tér 4., H-9700, Hungary

Zsolt Kővári
Konkoly Observatory, Budapest, Pf. 67, H-1525, Hungary

Joachim Krautter
Landessternwarte Heidelberg, Königstuhl, D-69117, Heidelberg, Germany

K.D. Leka
Colorado Research Associates, 3380 Mitchell Ln., Boulder, CO 80301, USA

Carla Maceroni
Osservatorio Astronomico di Roma, Via Frascati 33, I-00040 Monteporzio C. (RM), Italy

Sarah A. Matthews
Mullard Space Science Laboratory, University College London
Holmbury St. Mary, Dorking, Surrey RH5 6NT, UK

Nariaki Nitta
Lockheed Martin Solar and Astrophysical Laboratory
O/H1-12, B/252, 3251 Hanover Street, Palo Alto, CA 94304, USA

Katalin Oláh
Konkoly Observatory, Budapest, Pf. 67, H-1525, Hungary

László Patkós
Konkoly Observatory, Budapest, Pf. 67, H-1525, Hungary

Gothard Richter
Astrophysikalisches Institute Potsdam, an der Sternwarte 16, D-14482, Germany

Dominik Schäfer
Landessternwarte Heidelberg, Königstuhl, D-69117, Heidelberg, Germany

Brigitte Schmieder
Observatoire de Paris, DASOP/LPSH
5, Place Jules Janssen, F-92195 Meudon Cedex, France

Jörg Schweickhardt
Landessternwarte Heidelberg, Königstuhl, D-69117, Heidelberg, Germany

Sami Solanki
Institute of Astronomy, ETH-Zentrum, CH-8092 Zurich, Switzerland

Jan Straka
GKSS Research Center, Institute of Astmospheric Physics, 21502 Geesthacht, Germany

Béla Szeidl
Konkoly Observatory, Budapest, Pf. 67, H-1525, Hungary

Mózes Székely
Ministry of Education, Budapest

Emőke Tasnádi
Loránd Eötvös University, Budapest, Pázmány Péter sétány 1., H-1117, Hungary

Péter Tasnádi
Loránd Eötvös University, Budapest, Pázmány Péter sétány 1., H-1117, Hungary

Frans van't Veer
Institut d'Astrophysique, Paris, 98 bis Boulevard Arago, 75014, France

Ildikó Vincze
Gothard Observatory, Szombathely, Szent Imre Herceg u. 112., H-9707, Hungary

Spatially photospheric-coronal connections in SV Cam

L. Patkós

Konkoly Observatory of the Hungarian Academy of Sciences
H-1525 Budapest XII, Box 67, Hungary

Abstract. The short period RS CVn binary SV Cam has been monitored at Konkoly Observatory since 1972. The collected homogeneous data allows us the study of the long-therm behaviour of the system. An important question in RS CVn studies is whether photospherically observed spots do correlate with observed phenomena at other layers of the stellar surface. To study spatial connections to other surface layers we needed additional spectroscopic (Doppler imaging) and X-ray observations. As result we could establish clear spatially existing correlations between photosphere and corona in the system.

1. Introduction

The eclipsing binary system SV Camelopardalis is one of the closest systems of the short period group of RS CVn systems. Basic data of the system are: $P_{orb} = P_{rot} = 0.5930$ day, $a = 4\,R_{\odot}$, $i = 90°$, $r_2/r_1 = 0.64$, $r_1 = 1.3\,R_{\odot}$, $T_1 = 5750$ K, $T_2 = 4500$ K, $d = 74$ pc.

SV Cam has been monitored at Konkoly Observatory for more than 25 years. Photoelectric UBV photometry was used to observe the system. The collected homogeneous data allowed us the study of the long-therm behaviour of this short period eclipsing binary. Unfortunately because of the complex behaviour of the system UBV photometry alone is not enough to study SV Cam.

We organized therefore simultaneous X-ray, spectroscopical and optical observations of SV Cam. An international team was formed to carry out this work. Members of the group were the following astronomers: A. Hempelmann (Astrophysikalisches Institut Potsdam, Germany), A.P. Hatzes (McDonald Observatory, The University of Texas at

Austin, U.S.A.), M. Kürster (Max-Planck-Institut für Extraterrestrische Physik, Garching, Germany) and L. Patkós (Konkoly Observatory of the Hungarian Academy of Sciences, Hungary). Our aim was to establish spatial connections between photosphere and corona in the system SV Cam.

2. Observations

We observed SV Cam photometrically between J.D. 2,449,254-57 with the 50 cm telescope at Piszkestető Mountain station of Konkoly Observatory. A second complete light curve was observed with the same instrument at J.D. 2,449,310-11.

In the X-ray spectral region 0.1-2.4 keV we observed SV Cam with the ROSAT PSPC. The total exposure time was 35.5 ksec. This total exposure time between J.D. 2,449,225-229 was distributed over eleven half an hour exposures and seven exposures lasting only a few minutes. Main part of these observations covered 3.5 consecutive binary orbits of SV Cam.

The spectroscopic observations were carried out at Sandiford Cassegrain Echelle spectrograph of the 2.1 m telescope of McDonald Observatory. Because of some technical difficulties our spectroscopic observations (J.D. 2,449,288-357) were delayed in comparison to the X-ray and optical observations. We obtained 13 spectra which were well distributed in phase. Exposure times were limited to 20 min to minimize phase smearing.

3. Results

To construct the light curves we used the ephemeris given by Patkós (1982):

$$\mathrm{J.D.}_{\odot} = 2,433,777.42453 + 0.5930718E \tag{1}$$

In the optical light curve it was obvious that there was a significant deviation from a light curve without any spots. This deviation was more pronounced in the J.D. 2,449,254-57 light curve than the one obtained two month later at J.D. 2,449,310-11. We assumed photospheric spots only on the surface of the primary star, because the possible contribution of spots over the secondary star were to small to account significantly to the light curve changes.

According to our analysis in the case of the first light curve there was a round dark spot with a radius of $27° \pm 12°$ at latitude $50° \pm 20°$ and longitude $78° \pm 2°$. In the light curve at 2,449,310-11 the maculation effect was much smaller. In that case we couldn't do detailed spot model analysis. We could only determine the latitude of this smaller spot to be at $37° \pm 7°$. The spot modelling procedure is described in detail in the papers by Hempelmann & Schöneich (1987) and Patkós & Hempelmann (1994).

As a first step to produce the X-ray light curve we binned photon counts into time-intervals of maximum 200 sec. Then to reduce scatter we binned the observational points in phase intervals of about 0.02. The resulting X-ray light curve shows the minimum bit later than photospheric mid-eclipse.

We modelled the X-ray light curve with two coronal emission regions over the primary star. (A detailed description of the model we used can be found at: Ottman, Schmitt and Kürster 1993). The X-ray spectrum of SV Cam can be explained by a two temperature plasma of $T_1 = 3 \times 10^6$ K and $T_2 = 1.5 \times 10^7$ K.

SV Cam is a single lined binary. The mutual blending of the absorption systems originating from the two components is therefore no problem, but because of the high rotational velocity neighbouring lines can blend each other significantly. This blending can affect the derived spot distribution by altering the shape of spectral lines. Therefore we had to use only lines which seemed to be blend-free. Our analysis was based on four absorption lines: CaI 6102.8 Å, CaI 6122.0 Å, Fe I 6400.0 Å and CaI 6439.1 Å.

First we determined $v \sin i = 117 \pm 3$ km s^{-1}. Together with i = 90° and $P_{rot} = 0.5934$ day this value yields a stellar radius of the primary of 1.3 $R_{\odot}$ and a radius of the secondary star 0.83 $R_{\odot}$ ($r_2/r_1 = 0.64$).

We obtained independent Doppler images of the four lines. A description of the technics we used can be found at; (Vogt, Penrod and Hatzes 1987). These maps we got are not identical, but are very alike, and first of all, they agree well with the map we obtained analysing the photometrical data.

According to the averaged picture, we got a spot distribution which is dominated by a strong circular spot around latitude 60° and longitude 75°. There seems to exist also an appendage to this spot with a longitude similar to the one we got from the J.D. 2,449,310-11 optical light curve. This also coincides with the position of one of the derived coronal X-ray emission regions. One possible explanation could be, that the at J.D. 2,449,254-57 observed spot might have vanished by J.D. 2,449,310 or drifted to a new position. As the spectroscopic observations were done later (between J.D. 2,449,288 and J.D. 2,449,357) - a new strong spot might have emerged at the original position.

This kind of rapid spot evolution seems to be the regular behaviour of SV Cam (Patkós 1982; Zeilik et al. 1988). Note, that because of the 90° unambiguouty we cannot distinguish between spots on the "northern" and "southern" hemispheres. The spots might be on one or on both hemispheres. May be the above mentioned spot and its appendage are not connected, they might be at different hemispheres, and therefore physically not related.

A third active region was also derived from the spectroscopic observations. It seemed to be near the equator at around latitude 270°. It had a lower contrast in our Doppler image map. Despite this, it had a position near the second coronal X-ray source which we derived from the ROSAT light curve. This indicates a complete magnetically active region at this position. The reality of this spot is further strengthened by the fact, that surface spots have been frequently observed at the same position (see e.g. Zeilik et al. 1988).

The large wavelength coverage of the Sandiford Echelle Spectrograph made it possible to acquire data simultaneously on Hα. These spectral profiles were examined to see if any rotational modulation which may be an indication of surface plage could be detected.

There is a strong distortion (pseudo-emission bump) in the red wing of phase 0.004 that might be due to the secondary. The secondary star with an estimated spectral type of K4 is considerably cooler than the primary and when it transits it appears as a dark spot against the primary's surface. It thus produces a pseudo-emission distortion in the spectral line profile in the same manner as does a cool surface spot.

4. Conclusions

The binary system SV Cam is one of the closest binaries among the RS CVn class and hence, if the binary nature of these stars is responsible for their apparently enhanced activity then SV Cam should exhibit a much higher coronal X-ray emission as expected from two normal active G2/K4 MS stars. However, the observed X-ray count-rate of this star corresponds to the expected value which has been derived from the Rossby number.

The X-ray light curve can be explained with a model of two localized coronal sources in the binary system. One source is located closer to the primary star (most probably 0.8 $R_{\odot}$ above its surface), the other source lies in the middle between the two stellar components. Therefore, it remains somewhat open whether this source has its origin in magnetism of the secondary star or the primary one or whether it results from an interaction of the two stellar magnetospheres.

We found two photospheric active regions on the primary star. The first active region has been exhibited by Doppler tomography to be of complex nature. Its main structure is a large spot of almost circular shape. This spot was also found from optical light curve analysis.

The optical light curve was completely explained with this spot alone. However, the Doppler image showed an additional feature in this active region: an appendage to the circular spot. The whole region looks similar to a spot group on the Sun although one has to keep in mind that there is latitude ambiguity with respect to the equator, so that the circular spot may be in the one hemisphere while the appendage might be in the other hemisphere.

The presence of this appendage (a second spot inside a common active region) produces a noticeable change in the light curve and this would have been detected by the photometric measurements. There are, two explanations to solve this contradiction. The first but less likely possibility is that it is an artifact in the Doppler image resulting from observational errors and noise. However, this feature is evident in all four spectral lines analyzed. Hence, we felt its existence was real. The other possibility was the assumption of a temporary development of an active region. The spectrograms were measured one month later than the light curve. Such rapid changes of spottedness might not be abnormal in case of SV Cam as some of the figures in the paper by Patkós (1982) demonstrate.

The finding of spots exclusively on the primary star does not imply inactivity or absence of spots on the secondary star. Normally they cannot be seen, neither in broad-band light curves nor in the absorption lines outside the primary eclipse because of a too little contribution of the secondary star to the total light output. However, this may not be the case during the primary eclipse. During this phase all the photospheric lines in the primary show absorption features that are believed to come from the secondary star. However, no such absorption feature is seen in the Hα profile, which should be present if the secondary were an inactive K4 star. The implication is that at primary eclipse the light from the secondary (at the wavelength of Hα) is predominantly continuum or possibly even in emission.

Further evidence of such activity is seen at secondary eclipse. The Hα line strength of the primary increases at this phase. This is expected because outside of eclipse light from the secondary fills in the absorption lines of the primary making them shallower. However, the increase in Hα line strength is a factor of 1.6 greater than that expected from the continuum (at 6563 Å) expected from the secondary for its spectral type. Again the conclusion is that the secondary is chromospherically active.

The Hα variations show rotational modulation with a maximum near phase 0.8 and minimum at near phase 0.3. It is not known whether the origin of this variation - if it is indeed real - originates with surface features on the primary or secondary stars. If the chromospheric plages which may be responsible for this variation are located on the primary, then they may be associated with the large photospheric spot found by the Doppler imaging and photometry. If the secondary star produces this variation then the stellar surface region below one X-ray source is the more active one. In each case, the conclusion is that the strong spot on the primary star, the enhanced chromospheric activity of the secondary star and an intermediate coronal X-ray source are correlated with each other in a physical sense.

It seems that the light from the secondary can have a strong influence on the Hα line strength and this will complicate interpretations of the Hα variations. Furthermore, there is some evidence for transient variations.

References

Hempelmann, A. and Patkós, L. 1991, Astron. Nachr., 312, 19

Hempelmann A., Schöneich W., 1987, Astron. Nachr. 308, 201

Ottmann R., Schmitt J.H.M., Kürster M., 1993, Ap.J. 413, 710

Patkós, L. 1981, Astrophysical Letters 22, p:1-3,

Patkós, L. 1982, Comm. Konkoly Obs. No. 80. p:1-99

Patkós L., Hempelmann A., 1994, A&A 292, 119

Vogt S.S., Penrod G.D., Hatzes A.P.,1987, Ap.J. 321, 496

Zeilik M., De Blasi C., Rhodes M., Budding E., 1988, Ap.J. 332, 293

Discussion

B. Schmieder: What is the difference of your two coronal sources? How they are related to the spots that you observed or you modeled from Ca I observations?

L. Patkós: The main difference between the two coronal sources is that one source seems to be connected with the magnetic field of both star components while the other one belongs only to the corona of the primary component. Both coronal sources are connected to spots in the photosphere of the primary component.

S. Antiochos: Is it possible to say anything about the magnitude of the magnetic field in the star spots?

L. Patkós: Unfortunately in the case of SV Cam we can only speak about the existence or non-existence of spots on the primary component. To discuss the magnitude of the magnetic field we would need much more detailed knowledge about these spots ...

Zs. Kővári: You were talking about a binary with a K and G component. Which one is supposed to be spotted and why? Can we exclude the possibility of spot activity on both components?

L. Patkós: Both components are supposed to be spotted, but because of the great brightness difference between the two stars photographically we can only measure the ones over the surface of the primary component. However Hα measurements give us strong evidences the secondary to be spotted too.

Active stellar chromospheres: AR Lac

Zs. Kővári[1] and I. Pagano[2]

[1] Konkoly Observatory of the Hungarian Academy of Sciences
1525 Budapest, P.O. Box 67, Hungary
[2] Osservatorio Astrofisico di Catania
Via S. Sofia 78, 95125 Catania, Italy

Abstract. The UV Spectral Imaging method is shortly overviewed and then applied to map the active stellar chromospheres of the two components of the RS CVn-type eclipsing binary system AR Lacertae. We show the preliminary results for the Oct 1994 IUE data. From the decomposition of the series of Mg II k spectra chromospheric plages were identified and some flares were also detected. At the centre of mass of the system a bright plasma concentration was found suggesting a connection between the extended stellar magnetospheres.

1. Introduction to the UV Spectral Imaging method

Plage regions and flare events in the activity nests produce most of the UV variability of active stars. According to the solar-stellar analogy we expect these emitting centers to be physically connected with the photospheric spots. Usually, spot modelling and/or imaging techniques are applied to map the active stellar photospheres. However, comparing to the photosphere, mapping the chromospheric activity has more restrictions (cf. Neff 1992).

To map the chromospheric activity Walter et al. (1987) and Neff. et al. (1989) introduced the UV Spectral Imaging method, which is here shortly overviewed. The basic concept of this technique is, that an active stellar atmosphere produces a homogeneous, symmetric UV line profile and if there is a local additive emitting source, for instance a plage on the star, its emission component will be added to the homogeneous UV base. Since the additive component is Doppler-shifted by the stellar rotation, the sum-profile will be asymmetric and phase dependent. Thus, the UV line profile variation through the rotational cycle provides information about the spatial distribution of such individual

SOURCE	SPECTRAL MARK
homogeneous background	symmetric and constant
hemispheric inhomogeneities	symmetric, phase-dependent
global stochastic processes	symmetric, phase-independent, varying in time
large scale outflows	asymmetric, constant
plages	asymmetric, phase-dependent
flares	asymmetric, phase-dependent, varying in time

Table 1: Different kind of emitting sources with the spectral marks of their contribution.

emitting sources. To obtain this information we need to decompose the spectra to their parts.

Now let us take an additive emitting source (e.s.) above the stellar surface somewhere at β latitude! One can immediately write the Doppler shift $\Delta\lambda_D$ of its radiative contribution to the spectrum as:

$$\Delta\lambda_D = \frac{\lambda}{c}\, v_{rot,e.s.} \sin i \cos\beta, \tag{1}$$

where λ is the appropriate wavelength in vacuum, c is the speed of light, $v_{rot,e.s.}$ is the rotational velocity of the emitting source (corotation with the stellar surface is supposed), and finally, i is the inclination of the rotation angle. Measuring the Doppler shift, however, one cannot know β, only the product of $v_{rot,e.s.}\cos\beta$, because the vertical position (and vertical extension) of the emitting source is not known. These features can easily extend over the whole upper atmosphere (contrary to the photospheric spots which are *on* the stellar surface). However, a lower limit can be given to β if the measured $\Delta\lambda_D < \frac{\lambda}{c}\, v_{rot,e.s.} \sin i$ over a whole rotation, assuming, that the source is *on* the surface. Alternatively, an approximation can be given for the distance of the centre of the e.s. from the surface of the star (i.e., for the vertical extension) if it is supposed to be located in the equatorial plane (see Eq. 2 later in Section 2.3). An additional emitting source, however, can originate either from a long duration event (plage) or from a short duration one (flare) as well. Thus, to have also time resolution, one need to collect a series of spectra covering at least two rotations. As a brief summary of the different kind of emitting sources and their characteristics, in Table 1 we listed some of the most probable UV sources with their spectral marks (Neff 1992).

2. Application for AR Lac

2.1. The star

AR Lac (= HD 219334, $V = 6.1$ mag.) is an RS CVn-type eclipsing binary ($i = 87°$) with K0 IV and G2 IV components. The synchronous rotation period is near 2 days, however, this disadvantage is of no consequence using satellite measurements. AR Lac was observed by the International Ultraviolet Explorer many times during its operation between 1978-1996. IUE data on the system from 1981-1994 reflected an enhanced chromospheric activity on both stars (e.g., Rodonò et al. 1986, Neff et al. 1989, Pagano, et al. 1992, 1996). Spectral images from the past showed numerous plage regions on the cooler component, sometimes elongating towards the hotter star. Furthermore, a strong bright arch on the reconstructed X-ray image of the system from 1993 (Siarkowsky 1995) suggested the presence of hot plasma in the interbinary medium. We think, that both stars of this close binary system are embedded in a hot, extended and very active plasma (similar to the solar cromosphere-corona), moreover, these active envelopes are physically connected to each other.

2.2. The data

The 51 IUE LWP spectra (1800 – 3200 Å, $\Delta\lambda = 0.2$ Å) of the present analysis were collected in Oct 1994, covering about 2.2 consecutive rotation periods. For the data reductions we used the improved NEWSIPS (New Spectral Image Processing System) instead of the former standard IUESIPS (IUE Spectral Image Processing System) that has been affected by some systematic calibration errors (see, e.g., Busà et al. 1999). The new calibration procedure provided also a better S/N. The ephemerid constants were HJD 244795.6369 at $\phi = 0$ primary minimum and $P_{orb} = 1.983164$ days after Lanza et al. (1998). The observational log can be seen in Table 2. The physical parameters of the system is summarized in Table 3 (Marino et al. 1998).

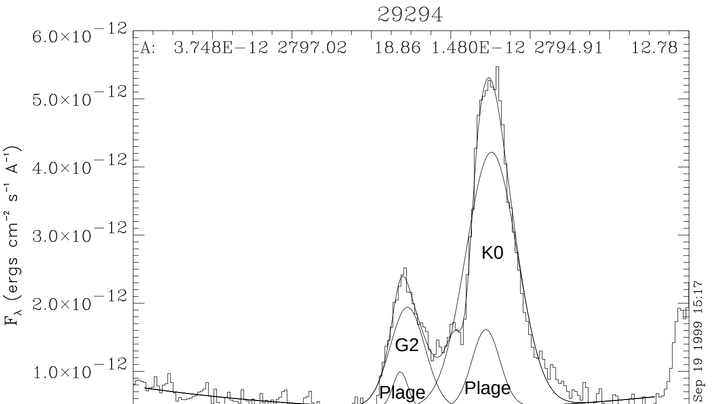

Figure 1: A sample 5-Gaussian-component fit to the Mg II k spectrum (see as frame #4 in Table 2).

For our analysis the Mg II k line (≈ 2796 Å) was used. For the decomposition of the spectra we used the "ICUR Spectral Analysis Package" developed by F. Walter and J. Neff (1992). The code is able to fit one dimensional datasets (spectra) with a maximum of five Gaussian curves. In Figure 1 a sample fit for the Mg II k line is seen using 5 Gaussian components.

2.3. Results

Decomposing the spectra requires an iterative, step-by-step analysis which can result in a series of multi-component fits using a minimum of two and a maximum of five Gaussians

#	LWP	HJD*	ϕ	remark	#	LWP	HJD*	ϕ	remark
1	29290	9627.7340	0.0987		27	29321	9629.9738	1.2282	
2	29291	9627.8225	0.1434		28	29322	9630.0430	1.2630	
3	29293	9627.9611	0.2133		29	29323	9630.1260	1.3049	
4	29294	9628.0328	0.2494		30	29324	9630.1977	1.3410	
5	29295	9628.1057	0.2861		31	29325	9630.2692	1.3771	
6	29296	9628.1766	0.3219		32	29326	9630.3437	1.4147	
7	29297	9628.2590	0.3635		33	29327	9630.4452	1.4658	sec. min.
8	29298	9628.3314	0.4000		34	29328	9630.5183	1.5027	sec. min.
9	29299	9628.4016	0.4354	sec. min.	35	29329	9630.5906	1.5392	sec. min.
10	29300	9628.4720	0.4709	sec. min.	36	29330	9630.6649	1.5766	sec. min.
11	29301	9628.5424	0.5064	sec. min.	37	29331	9630.7347	1.6118	
12	29302	9628.6130	0.5419	sec. min.	38	29332	9630.8039	1.6467	
13	29303	9628.6851	0.5783		39	29334	9630.9310	1.7108	
14	29304	9628.7614	0.6168		40	29335	9631.0030	1.7471	
15	29305	9628.8302	0.6515		41	29336	9631.0818	1.7868	
16	29306	9628.9015	0.6875		42	29337	9631.1545	1.8235	
17	29308	9629.0443	0.7594		43	29338	9631.2262	1.8596	
18	29309	9629.1198	0.7975		44	29339	9631.3041	1.8990	
19	29310	9629.1956	0.8358		45	29340	9631.3908	1.9427	pri. min.
20	29311	9629.2671	0.8718		46	29341	9631.4922	1.9938	pri. min.**
21	29312	9629.3454	0.9113		47	29342	9631.5747	2.0354	pri. min.
22	29313	9629.4176	0.9477	pri. min.	48	29343	9631.6459	2.0713	pri. min.
23	29314	9629.4895	0.9840	pri. min.**	49	29344	9631.7180	2.1076	
24	29315	9629.5623	1.0206	pri. min.**	50	29345	9631.7893	2.1436	
25	29316	9629.6343	1.0569	pri. min.	51	29348	9631.9625	2.2309	
26	29318	9629.7759	1.1284						

* 2440000+, mid-exposure time ** totality

Table 2: The observational log of the data.

(for a more detailed description see Rodonò et al. 1989). The main goal is to get such a result that is free of controversion. To achieve this, first one should synchronize the radial velocities of the stars with the respective Doppler shifts of the Gaussian components. To get a consistent model, it is also necessary to filter out the causeless sudden changes in the Gaussian parameters (position, FWMH, maximum) from one spectrum to the next. The results of this step-by-step process is displayed in Figure 1, where we used two Gaussians for fitting the base-profiles of the K0 and the G2 star at their radial velocities, a third Gaussian component with the instrumental width (FWMH = 0.25 Å) to fit the absorption of the IS medium moving by $v_{rad} = -34.54$ km/s, and another two Gaussian components to fit the residuals. Sudden enhancement in the C IV emission, that most probably are flare signatures, helps us to make a decision whether the residuals are the reason of plages or flares. Figure 2 suggests at least three short duration flare events. From those three, finally two were identified in frame #11 at $\phi \approx 0.5$ and in frame #29 at $\phi \approx 1.3$. The third flare at $\phi \approx 0.16$ could not been found in the spectra because of the lack of IUE LWP observations in this phase range.

Figure 3 shows the final solution in the phase-wavelength frame. The two stellar background lines moved with their radial velocities and the IS line has a time-independent position, as expected. However, four other emitting sources were found that were present

parameter	G2 IV	K0 IV
mass $[M_\odot]$	1.23	1.27
radius $[R_\odot]$	1.54	2.82
$v \sin i$ [km/s]	38	72
K [km/s]	119.43	106.73
$a \sin i$ $[10^6$km$]$	3.257	2.911

Table 3: AR Lac system parameters.

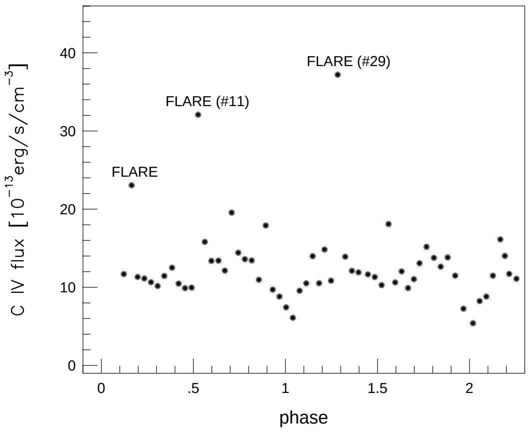

Figure 2: C IV flux variation. Three flare events are clearly seen. The first one at $\phi = 0.16$ could not been found in the Mg II spectra because of the lack of observations, however, the other two were identified easily in the frames #11 and #29.

for different phase ranges. The following equation helps to estimate the positions of these plages if co-rotation is supposed:

$$\Delta\lambda_D = \Delta\lambda_0 + \frac{\lambda}{c}\left[K_{K0}\sin\phi + \frac{2\pi}{P} r_{pl}\sin(\phi - \phi_{pl})\right]. \tag{2}$$

where $\Delta\lambda_D$ is the Doppler shift of the given Gaussian component, $\Delta\lambda_0$ is the radial velocity shift of the system's center of mass, K_{K0} is the orbital velocity of the K0 star, P is the period, ϕ is the phase, while r_{pl} and ϕ_{pl} are the polar coordinates of the plage in a coordinate system tied to the centre of mass of the K0 star.

In Figure 4 the reconstructed pole-on cartoon of the system is displayed with the two stellar disks and the four plages. Plage I and II are probably near, or on the surface of the K0 star, because their velocity shift in the K0 star frame is smaller than the stellar equatorial rotational velocity. Furthermore, these two plages are supposed to be polar features: from Eq. (1) $\beta_{PI} \approx 63°$ and $\beta_{PII} \approx 74°$. These plages are probably on different hemispheres, however, since the inclination is $\approx 90°$ there is no way to make distinction between the northern and the southern side. Plage III is far from the stars, deeply in the interbinary environment. We think, that such interbinary plages are possible, and could be the result of the interacting magnetic fields of the active components (cf. Siarkowski 1995). Such an interaction due to the strong magnetic activity can yield to variations in the orbital period (Applegate 1992), which, in the case of AR Lac, was reviewed recently by Lanza et al. (1998).

The fourth plage (Plage IV) is clearly connected to the G2 star, however, spectral images of the system between 1983-1991 (Pagano et al. 1996) did not show any plage on the hotter component. This considerable difference can be due to the new data reduction

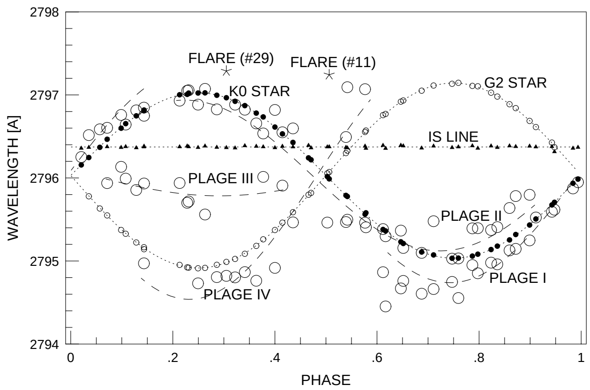

Figure 3: Wavelength changes of the Gaussians. Small marks show the stellar base profile changes and the position of the interstellar component. The two flares identified in LWP frames #11 and #29 are marked by asterisks. The big open circles show the positions of the additional Gaussians which are thought to be plages.

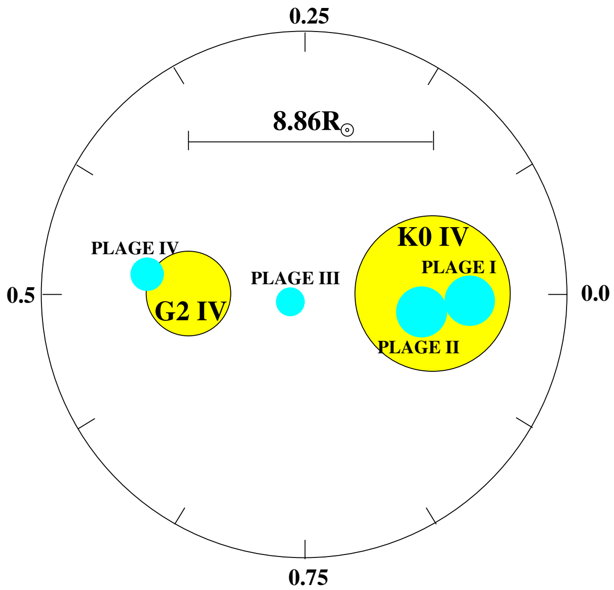

Figure 4: The reconstructed image of AR Lac in Oct 1994 on the real scale. The cartoon shows the system pole-on. The two big gray circles illustrate the two stars, while the darker circles are the extra emitting regions.

procedure (NEWSIPS) applied first for the Oct 1994 dataset. The authors strive to repeat all the UV spectral analysis for the IUE observations of AR Lac re-reduced by NEWSIPS.

Acknowledgements

Zs.K. wish to thank for the inspiring discussions with Dr. J. Jurcsik, Dr. K. Oláh and Dr. L. Van-Driel Gesztelyi. Financial supports from the LOC and from the Hungarian Government through OTKA T-026165 are kindly acknowledged.

References

Applegate, J.H. 1992, ApJ 385, 621

Busà, I., Pagano, I., Rodono, M., Neff, J.E., Lanzafame, A.C. 1999, A&A 350, 571

Lanza, A.F., Catalano, S., Cutispoto, G., Pagano, I., Rodonò, M. 1998, A&A 332, 541

Marino, G., Catalano, S., Frasca, A., Marilli, E. 1998, IBVS No. 4599

Neff, J.E. 1992, in: *Surface Inhomogeneities on Late-Type Stars*, Proc. Coll. Armagh Obs., eds. P.B. Byrne, D.J. Mullan, Springer-Verlag, Heidelberg, p. 54

Neff, J.E., Walter, F.M., Rodonò, M., Linsky, J.L. 1989, A&A 215, 79

Pagano, I., Rodonò, M., Neff, J.E. 1992, in: *Cool Stars, Stellar Systems and the Sun*, eds. M. Giampapa & J.A. Bookbinder, ASP Conf. Ser., Vol. 26, 362

Pagano, I., Rodonò, M., Walter, F.M., Neff, J.E. 1996, in: *Magnetodynamic Phenomena in the Solar Atmosphere - Prototypes of Stellar Magnetic Activity*, IAU Coll. No. 153, eds. Y. Uchida, T. Kosugi & H.S. Hudson, Kluwer, Dordrecht, p. 631

Rodonò, M., Cutispoto, G., Pazzani, V., et al. 1986, A&A 165, 135

Siarkowski, M. 1995, in: *Stellar Surface Structure, Poster Proceedings*, IAU Symp. No. 176, ed. K.G. Strassmeier, p. 190

Walter, F.M., Neff, J.E., Gibson, D.M., Linsky, J.L., Rodonò, M., Gary, D.E., Butler, C.J. 1987, A&A 186, 241

Discussion

L. van Driel: This is a very exotic binary system for a solar physicist with the chromospheric and coronal emission coming from between the stars. Do you have some data on the density of the emitting plasma?

Zs. Kővári: Yes, I refer to the paper of Byrne et al. (1987, A&A 180, 172) where the authors made attempts to derive the physical parameters of the upper atmosphere of AR Lac. On the basis of some density sensitive lines they estimated a solar-like density value of $\log N_e = 10.5\,\mathrm{cm}^{-3}$.

B. Schmieder: C IV emissions could, may be, correspond to other events than flares. In the Sun "C IV explosive events" have no real signatures in X rays.

Zs. Kővári: It's true. However, while refining the decomposition of the spectra the C IV abrupts were identified even in the Mg II spectra, and we think the flare events to be the most plausible explanation.

S. Antiochos: Is it possible that the emission between the two stars is due to an interaction of the winds of the stars?

Zs. Kővári: I should say that this possibility cannot be excluded. However, I'm not sure that the winds without magnetic field can reach the necessary density between the stars. I'm much more inclined to think that the interaction between the magnetically driven and compressed winds produces the observed interbinary UV emission.

Magnetic braking in Solar-type close binaries

C. Maceroni[1] and S.M. Rucinski[2]

[1] Rome Astronomical Observatory, Monteporzio, Italy
[2] David Dunlap Observatory, Toronto, Canada

Abstract. In tidally locked binaries the angular momentum loss by magnetic braking affects the orbital period. While this effect is too small to be detected in individual systems, its signature can be seen in shape of the orbital period distribution of suitable samples. As a consequence, information on the braking mechanisms can be obtained – at least in principle – from the analysis of the distributions, the main problems being the selection of a large and homogeneous sample of binaries and the appropriate treatment of the observational biases.
New large databases of variable stars are becoming available as by-products of microlensing projects, which have the advantage of joining, for the first time, sample richness and homogeneity. We report the main results of the analysis of the eclipsing binaries in OGLE-I catalog, that contains several thousands variables detected in a pencil-beam search volume towards the Baade's Window. By means of an automatic filtering algorithm we extracted a sample of 74 detached, equal-mass, main-sequence binary stars with short orbital periods (i.e., in the range $0.19 < P < 8$ days) and derived from the presently observed period distribution, after correction for selection effects, the expected slope of the braking law.
The results suggest an AML braking law very close to the "saturated" one, with a very weak dependence on the period. However we are still far from constraining the precise value of the slope, because of the important role played by the observational bias.

1. Introduction

The evidence that stellar rotation depends on spectral type was given by Struve and Elvey (1931), but the idea of evolution with time came much later: Kraft (1967) found a relation between age and rotational velocity for late-type stars in open clusters, and Skumanich (1972) quantified it in a time decay with a dependence of the form: $v_{rot} \propto t^{1/2}$. That is equivalent to a variation of the angular velocity $\dot{\omega} \propto \omega^3$, and applies to the slow rotation regime ($10 - 20$ km/s).

The first physical interpretation of these facts – and of the slow rotation of the Sun as well – was the magnetic braking model by Schatzman (1959), who pointed out that a relevant angular momentum loss can be produced even with negligible mass loss, if the star has a magnetic field forcing the corotation of the outgoing stellar wind. Then the lever arm of the braking torque is comparable to the Alven radius that in late-type stars, which have convective envelopes and host a dynamo, can be much larger than the stellar radius.

Schatzman's model set the general framework of rotational evolution in late-type stars, whose details turned out to be much more complex than initially thought. Stauffer & Hartmann (1987) and Soderblom et al. (1993) surveyed rotation among the late type stars of clusters of different ages, down to a treshold of ~ 10 km/s and showed the existence of very fast rotators (up to 200 km/s) in young clusters (as α Per and the Pleiades). The evolution of the $v \sin i$ distribution, and in particular the rapid convergence in rotation rates for small masses at the Hyades age, cannot be explained by the Skumanich relation, and possibly a model with a different (saturated) braking law is necessary.

Tidally locked binaries, with at least one late-type dwarf component, can be an independent important source of information on the braking mechanism. Their most useful property – in this respect – is that thanks to the efficient synchronization mechanisms, the angular momentum taken away from the outgoing wind is actually subtracted from the orbital reservoir and affects the orbital period, which is an easily measurable quantity. The final result of angular momentium loss (AML) is shrinkage of the orbit, period decrease and spin-up of the components. The evolution of the orbital period contains therefore, information on the braking mechanism and indirectly on the star internal structure.

While the AM losing late-type stars that are single or form wide binaries experience a decay of rotation, those in tidally locked binaries spin faster and faster, while approaching to each other, and eventually form a contact binary.

The typical time-scale of AM evolution in these binaries (of the order of the Gyr, depending on model details) is too long to expect a measurable effect in the period of individual systems (Maceroni, 1999), as the timespan of observations for the best studied binary is still around a hundred years. However, the signature of AML can be in principle seen in the evolution of the orbital period distribution of binary samples.

An initial period distribution will evolve into the presently observed one according to the details of the model for AM loss and transfer. The main difficulty to face in handling this problem is sample selection. Previous woks were based either on the all-sky late type Main Sequence binary sample (Maceroni and Van 't Veer 1991=MV91, Maceroni, 1992), or on the Hyades one (Stepien 1995 = ST95). The former is a rich but unavoidably inhomogeneous sample, the latter is homogeneous and coeval, but very small. When, recently, large and homogeneous catalogs of binaries were published as by-products of microlensing searches, new possibilities were open for these studies.

We present in this paper the results obtained from the first of these catalogs that has been made public and accessible on-line, that from the OGLE-I experiment (Udalski et al. 1994). This provides a sample of $\sim$ 1200 eclipsing and in great majority close binaries, in the Baade's window direction.

We will first shortly describe the theoretical model of AML evolution and the algorithm used for the automatic extraction of the binary sample of interest, and then compare our results relative to the period distribution evolution with those of previous works. The general properties of the OGLE-I sample of pre-contact eclipsing binaries are presented in Maceroni and Rucinski (1999, MR99).

2. The evolution of the orbital period distribution

The evolution of the angular momentum of a tidally locked binary is determined by:

- the braking law, which is usually expressed as $\dot{\omega} \propto \omega^{\alpha}$. This corresponds to a variation of the rotational AM, $H_{rot} \propto P_r^{-\alpha}$.
- the AM transfer between spin and orbit because of tidal locking. Studies on tidal coupling in a close binary with late-type dwarf component (P_{orb} of a few days) show that the phenomenon has a time-scale much shorter than the others of relevance here, so that the coupling can in practice be considered istantaneous. Hence, $\dot{H}_{orb} \equiv \dot{H}_{rot}$, and thanks to spin- orbit synchronization $P_{orb} \cong P_{rot} = P$, dropping the suffixes.
- the internal rotational profile of the star. This is often assumed to be uniform (i.e. rigid body rotation).

As by definition $\dot{H}_{orb} \propto P^{-2/3}\dot{P}$, the rate of period change is $\dot{P} \propto P^{2/3-\alpha}$ which can also be written, introducing the time scale of period evolution, as:

$$\left|\frac{\mathrm{d}\log P}{\mathrm{dt}}\right| = \tau \propto P^{\alpha+1/3}. \tag{1}$$

The way a period distribution will look because of evolution depends on the period evolution function (PEF), on the distribution at formation time and its time dependence. The simplest case is that of a sample of binaries all formed at the same time t_0. If their initial period distribution (IPD) is $f_0(\log P)$ the evolved one at a later time t_* (e.g. the present time of observation), $f_*(\log P)$, results from the requirement of constancy of the total number of the systems:

$$f_*(\log P) = f_0(\log P)\left|\frac{\mathrm{d}\log P(t_0)}{\mathrm{d}\log P(t_*)}\right| = f_0(\log P)\frac{\tau_*}{\tau_0} \tag{2}$$

which contains the period evolution from the time t_0 to t_* as: $P_* = P_*(P_0)$ (for brevity, we use P_n to signify $P(t_n)$).

Thus, the present period distribution function $f_*(\log P)$ is proportional to the ratio of the present and the initial time-scales (i.e. rapid evolution will locally deplete the distribution). Obviously, in the more realistic case of time-independent formation process

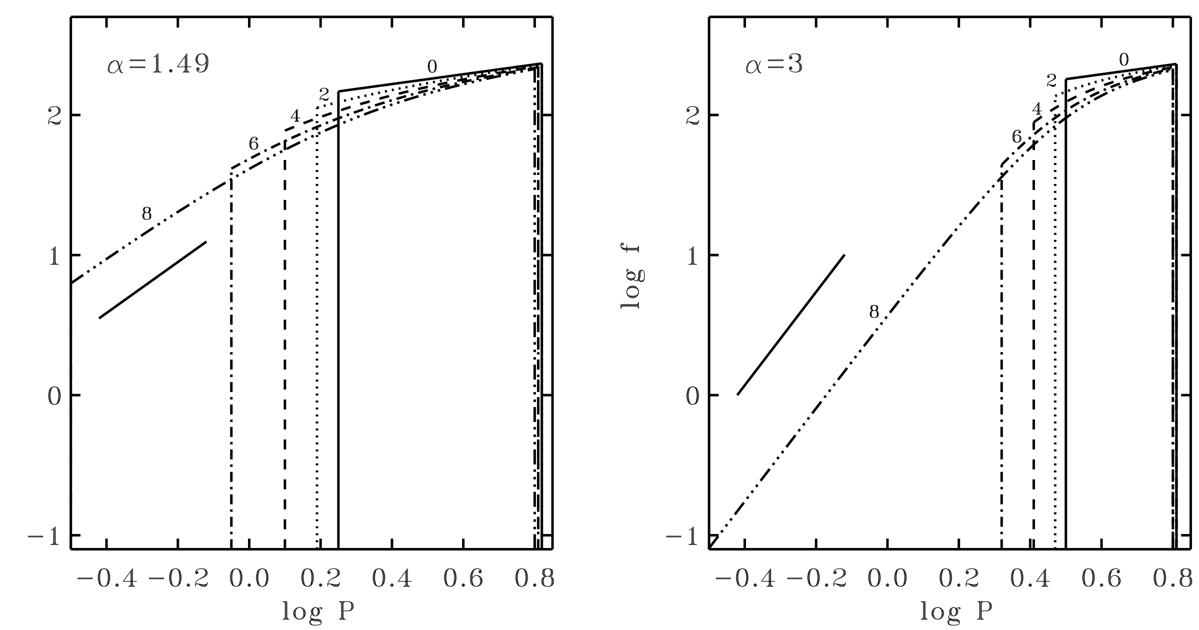

Figure 1: The figure shows the expected evolution of the period distribution for two values of α, 1.49 and 3, following the theoretical predictions of Stępień (1995) and Skumanich (1972). The starting distribution in both cases have the same, gently-positive slope $\beta = 0.35$, as in $f_0 \propto P^\beta$. The initial period ranges are different for each panel; they have been adjusted to populate the distribution down to 0.3 days after the time interval of 8 Gyrs. The numbers by the lines give the ages of the repective populations in Gyr. The short vectors in the left parts of the panels give the asymptotic slopes $\alpha + 1/3$, as expected from considerations in the text.

over some time interval, the present period distribution would be a result of an integration of the right side of Eq. 2 over the whole time interval.

The stars in Baade's Window are not coeval but in their majority probably belong to a relatively old population, possibly older than $\sim$ 5 Gyr (Ng et al. 1996, Kiraga et al. 1997), so that products of recent formation events are quite unlikely to be seen there. In this case, the existing PEF models (as those of MV91 or ST95) predict that the systems presently observed as pre-contact binaries come from a initial period range where the time-scale of period change was very long and weakly time dependent for the first few Gyr of evolution. As a consequence the result of the integration over the formation time will be proportional to $f_0\tau_*/\tau_0$, where τ_0 will actually be a mean over the formation time. Thus, as long as we study only the shape of the period distribution, we can just use the expression in Equation 2.

The analytical form of the initial period distribution is somewhat uncertain for binaries of short period. A possible and reasonable choice is the extrapolation of the period distribution of Duquennoy and Mayor (1991). That has the shape, in the logarithm of the period, of a wide Gaussian with a maximum at $\log P = 4.8$ and $\sigma \log P = 2.3$ (with the period P expressed in days); it can be approximated, within the range $0 < \log P < 1$ days, by $N(\log P) \propto P^\beta$ with $\beta = 0.35$.

The present period distribution obtained from the initial distribution and Eqs. 1, 2, will then be:

$$f_*(\log P) \propto P^{\beta} \left[1 + (\alpha + 1/3)\, \frac{T}{\tau_*}\right]^{\frac{\beta-\alpha-1/3}{\alpha+1/3}} \tag{3}$$

This turns out to be simply proportional to the IPD for $t \ll \tau$ and to the timescale τ_* for $t \gg \tau$.

Figure 1 shows, as example, two evolving distributions, which have been computed using the α value of Skumanich relation ($\alpha = 3$) and the lower one, $\alpha = 1.49$, corresponding to a local fit of the braking law as derived in ST95. In both cases one can notice that the slope of short period part of the initial distribution quickly converges to the $\alpha+1/3$ value. We can therefore expect to derive, by comparison of IPD with the present distribution of the Baade's window sample, the α value. To this purpose we should first find a criterion to extract the sample of pre-contact MS binaries and a way to correct the observed distribution for the selection effects.

3. The sample of equal mass pre-contact MS binaries

The OGLE-I catalog of eclipsing binaries provides for each system the period, the $B-V$ color at maximum, and the I light curve.

The extraction of the sample of pre-contact MS binaries was performed by means of a filtering procedure based on the first coefficients of the Fourier decomposition of the light-curve, similar to that formulated by Rucinski (1997, R97). As shown in that paper, the pair of coefficient a_2 and a_4 from the light curve decomposition

$$l(\phi) = \sum_i a_i \cos{(2i\pi\phi)} \tag{4}$$

form a powerful separator of contact and non-contact systems. That because the various coefficients contain different information on the light curve shape. In particular a_1 reflects the difference between the two eclipses and for equally-deep minima goes to zero; the second, a_2 is the largest of the coefficients and represents the total amplitude of the light variations; a_4 expresses the light curve "peakedness" and goes to small values for the light curves of contact systems. Figure 2 shows an example of the various Fourier components for the pre-contact system BW3 V38 (Maceroni and Rucinski 1997).

The details of the filtering procedure are fully described in MR99, we recall here its steps:

- non-contact/ contact binary separation by means of the locus $a_4 = a_4(a_2)$ (see Fig. 5 of R97).

- selection of systems whose light curves display similar depth minima. This was necessary because of the limited information contained in the single color light curves. The only way to reject, without color information, the unwanted evolved Algol-type systems was the selection on the basis of unequal minima. That, unfortunately but unavoidably, rejects as well unevolved systems with components of unequal temperature (that is equivalent on the MS to unequal masses). This selection was performed by means of the a_1 and a_2 coefficients, taking into account a necessary scaling of the accepted difference in depth with the light curve amplitude, and comparing the sample distributions of a_1 and a_1/a_2 with those of in a typical similar eclipse depth sample (W UMa system) and our sample. The result were boudary conditions on $|a_1|$ and $|a_1/a_2|$, namely $|a_1| \leq 0.017$ and $|a_1/a_2| \leq 0.2$ (see Fig 4 of MR99).

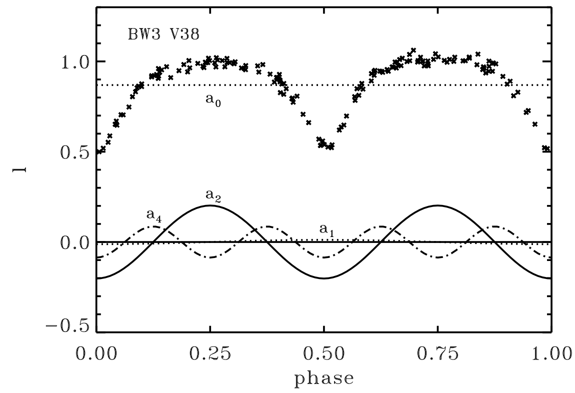

Figure 2: The light curve of the OGLE system BW3 V38 and some of its first Fourier components. Each cosine curve is labeled with the corresponding coefficient as defined in the text. The constant term a_0 is also shown. It is evident that a_2 gives the main contribution to the light curve amplitude, a_1 to the difference between minima (in this case very small), and that a_4 expresses the eclipse "peakedness", giving the main contribution to minimum wing shape.

As the resulting sample still retained a few systems with long period and evolved (presumably giant) components, we set an upper limit to the period of dwarf tydally locked systems to 8^d.

The final sample contained 77 systems. For all of these the distance, d, the unreddened colors and absolute magnitudes were derived by an iterative process, in an approach somewhat similar to that described in R97, and identical to that used in the study of the system BW3 V38 (MR97). An adopted absolute-magnitude calibration $M_I = M_I((V-I) - E_{V-I}(d))$ for the main sequence (Reid and Majewski 1993), shifted by 0.75 magnitude to allow for two identical stars, was used for a first guess of d and reddening E_{V-I}. An iterative procedure was then started with the reddening allowed to vary linearly with distance between zero and the maximum value derived from the background Bulge giants by Stanek (1996), and assuming that E^{max}_{V-I} is reached at the distance of 2 kpc, and then does not increase.

After determination of the unreddened colors, three too blue systems were rejected. The sample of pre-contact late-type systems from OGLE-I sample eventually contains 74 systems. While its size is still moderate, it has to be noticed that it less than a factor of two smaller than the previously known sample of all-sky binaries studied by Maceroni and Van't Veer (1991) and much larger than the Hyades one (12 systems).

The main advantage of the automatic filtering still is, in this case, the objectivity of the selection, as a manual selection could still be considered feasible, though long, for the OGLE-I catalog. However, the same procedures used in this study can be applied, as they are, to the larger samples from other surveys, when those will be available to the scietific community.

4. The period distribution of OGLE-I pre-contacts

The complete study of the properties of the OGLE-I sample can be found in MR99. Here we briefly present those relevant to the definition of the period distribution and describe a simple way to correct it for observational selection effects.

From the $V - I$ color we inferred the spectral types and tried to check if the period distribution, and the AML loss features, showed any dependence on it. Our main concern was that fully convective M-type systems, could show a different distribution related to peculiar AML mechanisms, but statistical test on the (small) sample of 10 presumably M-type stars and the remaining 64 F-G-K systems (MR99), in which the sample could be splitted, gave no indication of such a dependence. Moreover, no correlation was found between the periods and colors or absolute magnitudes. One does not expect, therefore, dependence of the distribution on the distance, that makes easier the treatment of the data in a magnitude limited sample as OGLE is.

The final observed period distribution of the whole sample, in bi-logarithmic form, is shown in Fig. 3. Contrary to the models of Fig. 1, the slope of the distribution is negative. A weighted linear least square fit to the histogram of Fig. 3, as $\log N = A_0 + A_1 \log P$ (with weigths given by poissonian errors in bins $\Delta \log P + 0.2$), gives for the whole sample $A_0 = 1.05 \pm 0.06$, $A_1 = -0.79 \pm 0.16$, or $A_0 = 1.02 \pm 0.07$, $A_1 = -0.80 \pm 0.17$ for the FGK sub-group. The values of χ^2 for the fits were 3.1 and 3.7 for the 6 log-period bins. The linear fits are thus only marginally appropriate, but definitely much better than flat distributions.

To better define the uncertainty limits on the coefficients A_0 and A_1, a Monte-Carlo experiment has as well been conducted in which weighted fits were made to several thousand artificial Poisson distributions with the same *mean* values for each log-period bin (because the mean values do not form a linear dependence, such fits provide more realistic estimates of the uncertainties of the coefficients A_0 and A_1). The results, expressed in terms of the distributions of the individual determinations of the coefficients around their median values, are given in Table 1.

We think that the reason of the negative slope is to be found in selection against discovery scaling in proportion to the orbital period. The chances of eclipse detection rapidly decrease with increasing separation of the components because:

- the range of inclination yielding eclipses shrinks
- the eclipses become pregressively shorter
- in a time limited survey as OGLE is, fewer orbital cycles are observed

A simple way of estimating probability of discovery of a system is the evaluation of solid angle subtended by the sum of the fractional radii $(r_1 + r_2)/a$, relative to hemisphere visible by a distant observer, i.e. by dividing it by 2π steradian. This takes into account the first two effects of period lengthening mentioned above. This relative solid angle is given by the integral of the eclipse relative durations over the range of inclinations that can

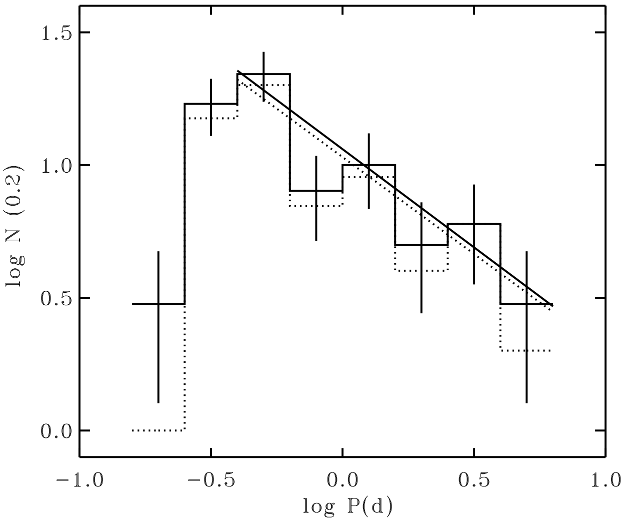

Figure 3: The orbital period statistics in logarithmic units of the number of systems in bins $\Delta \log P = 0.2$. The histogram is shown for the full sample of 74 systems (solid lines) and the FGK group of 64 systems (dotted line), but – for clarity – the Poisson errors are shown as vertical bars for the full sample data only. The sloping lines show the linear fits, as described in the text.

result in eclipses, which evaluates to $1 - \left(\sqrt{1 - \left(\frac{r_1 + r_2}{a}\right)^2}\right) \approx \left(\frac{r_1 + r_2}{a}\right)^2$. For fixed radii, the probability of discovery of an eclipsing system scales as the inverse of its orbital separation in square, $\propto a^{-2}$. A discovery-probability scaling according to a^{-2} should be a particularly reasonable assumption for the equal-mass, hence presumably equal-radius component systems that we selected. The correction factor that we should use to multiply the statistics of periods is then expected to behave as: $corr \propto a^2 \propto M_{tot}^{2/3} P^{4/3}$. The mass dependence can be further removed by observing that, as we described above, the orbital periods in our sample do not correlate with the color or absolute magnitude. We can therefore assume that they do not correlate with the total mass of the system, M_{tot}. The correction factor to apply to the histograms in Figure 3 would be then: $corr \propto P^{4/3}$. Thus the correction to the slope in the bi-logarithmic distribution, C, turns out to be $C = 4/3$.

The relation between the braking-efficiency exponent, α, the observed slope, A_1, and the observational selection correction, C is: $\alpha = A_1 + C - 1/3$. As any results will in fact be dominated by the systematic effects characterized by C, we set $A_1 = -0.75 \pm 0.20$, that is an intermediate value between the directly derived value and that from the Montecarlo experiment of Table 1 (the error estimate comes from the Monte Carlo experiment). The corresponding value for the braking exponent is:

$$\alpha = 0.25 \pm 0.20 \qquad (5)$$

Therefore, the material from the OGLE-I survey favours a quite flat (saturated) braking law, this result in good agreement with the known saturation of the activity indicators at short periods first pointed out by Vilhu (1982).

Actually subsequent work (see for instance Wichmann et al. 1998) shows that the activity indicators, which can be related to the AML rate, show a change of slope – from a saturated to a steeper law – at rotation periods around 3–4 day. The small size of our sample and the consequent relatively coarse binning did not allow us to properly analyze this feature: the expected change of the slope would fall in the tail of our distribution

Term	median	1-sigma range	2-sigma range
Ful l			
A_0	1.07	$-0.07, +0.05$	$-0.14, +0.11$
A_1	-0.74	$-0.18, +0.21$	$-0.40, +0.38$
FGK			
A_0	1.03	$-0.08, +0.06$	$-0.15, +0.11$
A_1	-0.73	$-0.22, +0.22$	$-0.43, +0.49$

Table 1: Results of the Monte-Carlo determinations of the coefficients A_0 and A_1.

since we currently have only three systems in the bin $P > 5$ days. On a qualitative ground, Figure 3 does suggest that an exclusion of the last bin from the fit would result in a slightly flatter braking law, but we feel that an estimate of the slope based on such reduced data would actually be an over-interpretation of the available material.

5. Discussion and conclusions

Our results strongly depends on the power of the correction applied to the distribution because of observational biases, however there are some plausibility arguments in favour of values of C not too different from that we derived.

For instance, a genuine negative slope of the distribution could be obtained if there were no selection effects ($C = 0$) and that would be in agreement with the distribution of short-period systems in Hyades as found by Griffin (1985). However, it is hard to assume the OGLE survey free from observational biases.

The result by Stepien (1995), with its local linear fit for $\log P \leq 1^d$ giving $\alpha = 1.49$, would instead imply a C almost twice our value, $C = 2.57$. A stronger selection cannot be excluded, but we consider it unluckily.

On the basis of the available data we can draw at least one firm conclusion on the general shape of the distribution. There is no evidence in our homogeneous sample for any bimodal period distribution, similar to that found by Farinella et al. (1979) with a dip at $\log P \simeq 0.2$. We believe that this dip and a secondary maximum in the distribution were most probably produced by misclassification of evolved systems as consisting of main-sequence components. Our smooth period distribution, without any structure, implies quite a different form of the braking law with respect to that derived by MV91 and Maceroni (1992). Though the functional form remains partly similar, in the sense of a "saturated" braking at short orbital periods ($\alpha = 0$), the other main feature, namely the sudden increase of the braking efficiency for rotation of $\sim 10\omega_\odot$ is no longer mandated by the data. That feature was the necessary to reproduce the bimodality of field G-type system distribution which showed a pronounced dip around $\log P = 0.2$ days (Farinella et al., 1979).

The highly desiderable improvements for future are in two different directions: first that of richer sample, which would allow more detailed studies on the spectral type dependence of the distribution and hence of the AML properties. But a meaningful improvement could as well be achieved if multi-band similar catalogs were available, since the single color curves implied a too selective filtering, which excluded potentially interesting system from our study.

References

Duquennoy, A., & Mayor, M. 1991, A&A, 248, 485 (DM91)

Farinella, P., Luzny, F.,Mantegazza, L., & Paolicchi, P. 1979, ApJ, 234, 973

Griffin, R.G. 1985, in Interacting Binaries, eds. P.P. Eggleton and J.E. Pringle, Reidel, Dordrecht, p.1

Kraft R. P., 1967 ApJ 150, 551

Kiraga, M., Paczynski, B., & Stanek, K.Z. 1997, ApJ, 485, 611

Maceroni, C. 1992, in 'Inside the stars', W. Weiss & A. Baglin Eds, ASP Conf. Ser. 40, 374.

Maceroni C., 1999, New Astronomy, in press

Maceroni, C., & Rucinski, S.M. 1997, PASP, 109, 782 (MR97)

Maceroni C. & Rucinski, S. M. (1999) AJ 118, 1819 (MR99)

Maceroni, C., Van 't Veer F., 1991, A&A 246, 91 (MV91)

Ng, Y.K., Bertelli, G., Chiosi, C., & Bressan, A., 1996, A&A, 310, 771

Reid, N., & Majewski, S. R. 1993, ApJ 409, 635

Rucinski, S.M. 1997, AJ, 113, 407 (R97)

E. Schatzman *Ann. Astrophys. Suppl.* 8 (1959) 129

Skumanich, A., 1972, ApJ 171, 565

Stanek, K. Z. 1996,ApJ, 460, L37

Stepien, K. 1995 MNRAS 274, 1019 (ST95)

Struve, O. Elvey C.T., 1931 MNRAS 91, 663

Stauffer J. R. & Hartmann, L. W., 1987, ApJ, 318,337

Soderblom, D. R., Stauffer, J. R.,Mc Gregor, K. B., Jones, B. F., 1993, ApJ 409, 624

Udalski, A., Kubiak, M, Szymanski, M., Kaluzny, J., Mateo, M., & Krzeminski, W. 1994, AcA, 44, 317

Vilhu, O. 1982, A & A, 109, 17

Wichmann, R., Bouvier, J., Allain, S., & Krautter J., 1998, A&A, 330, 521

Solar-stellar connections - modelling the Sun as an active star

K. Oláh

Konkoly Observatory of the Hungarian Academy of Sciences
H-1525 Budapest XII, Box 67, Hungary

Abstract. A diagnosis of photometric starspot models is given through modelling active areas on the Sun using softwares originally written for starspot modelling. One-dimensional measurements of the Sun in radio (10.7cm, DRAO, Canada) and in soft X-rays (GOES satellites) were used for the modelling and the results were compared to the contemporaneous direct images of the solar disc made in similar wavelengths at Nobeyama and with the Yohkoh spacecraft.
Conflicting results are found in recovering spot coordinates. The resulting latitudes of the spots are uncertain, artificially high latitude spots appear to account for global brightness changes. The flux ratio between the spotted and undisturbed areas are evolving with the active region, following a power law. The modelled spot areas are close to the reality when this change is taken into account. On a longer time base the flux of the disturbed areas (active nests) comes from co-existing emerging and decaying spots, thus the flux ratio has an almost constant average value. Using this average flux ratio the long-term changes of the spot area could be recovered well. This means, that in starspot modelling, if a well-established spot temperature is found, on a long-term base the resulting changes of spottedness are probably real. However, this is not necessarily true for shorter terms.

1. Introduction

The precise photometric databases are almost three decades long for some well observed active stars (see e.g. Strassmeier et al. 1997). With the general use of automated photometric telescopes (APTs) the databases are continuously growing. It is very important to extract as much information as possible out of those data, that are often used to study the patterns of spottedness using spot modelling codes. It is of crucial importance to test the reliability of the spot modelling results. Since the photometric data have only one dimension and thus have limited information content, simplified assumptions are used: two, or as a maximum, three co-existing spots are assumed. The modelling codes need physical input parameters like the unspotted brightness of the star, the temperature of the spots compared to the quiet photospheric temperature, the inclination angle and the limb darkening coefficients. The stability of spot modelling results (resulted spot locations) and the effects of the physical input parameters were thorougly investigated by Kővári and Bartus (1997).

The ideal test of the reality of any starspot model would be to compare the modelling result with a direct image of the star. This experiment became possible since contemporaneous one-dimensional measurements and images are taken on the Sun every day. This possibility was used first by Catalano et al. (1998) who modelled C II line flux at 133.5 nm and compared the results to direct Hα images, and by Peres et al. (1998) who synthesized solar spectra as if it were measured from a point source (a star) by a satellite (like ROSAT), using Yohkoh images. The opportunity to test photometric starspot modelling arose with the 1996 solar activity minimum when the Sun's activity was very simple, on the other hand, images were taken and one-dimensional flux measurements were gathered each day in several wavelengths.

An important question in starspot modelling is the value of the spot temperature that directly affects the resulting spot area (and through that even the latitude). The long-term databases of the stars do not have sufficient colour information to derive spot temperature for each light curve, therefore usually one constant spot temperature (deduced from recent photometric observations which have V and I colours or for some stars from TiO bands) is used when modelling photometric data. Another question is, how reliable the derived change of spottedness of an active star could be. The existing observations around the solar activity minimum made possible to investigate this problem as well.

2. Method and data

The first step of the work was the modelling of one active region on the Sun. This was possible using the solar data between mid-July and the end of October, 1996, when only one major active region existed on the Sun. Since the amplitude of the flux variability caused by the single active region of the Sun in the radio and X-ray wavelengths was similar to those we observe on stars, we could use these observations to test our spot modelling results. We run our modelling code on the solar one one-dimensional data and compared the results with the direct images (Oláh et al. 1999a, Oláh et al. 1999b, hereafter Paper I).

The second step of the work was modelling an active nest on the Sun. This nest existed between March-December, 1996, including the time when the nest consisted of only one active region. The modelling of the active nest could test how reliable the spot area results could be on a longer time-base.

We used two one-dimensional datasets: daily 10.7cm solar radio flux measurements recorded at DRAO (Dominion Radio Astrophysical Observatory, Tapping and Charrois 1994) Penticton, Canada and soft X-ray irradiance measurements in the 1-8 Å flux range provided by GOES9 (Geostationary Orbiting Environmental Satellites) satellite. Transient (flare) events were removed from the data since we were interested in only the slow flux variability caused by the rotation of the Sun. The GOES9 data were averaged to three datapoints/day; this way the number of data were similiar in the two wavelength range investigated.

The two-dimesional datasets (images) that were used for comparing the modelling results with the reality were full-disc radio images taken with the Nobeyama Radioheliograph at 17GHz ($\lambda = 1.7635$cm, Nishio et. al. 1994, Hanaoka et. al. 1994) and soft X-rays full-disc images recorded with the grazing incidence soft X-ray telescope (SXT) onboard Yohkoh (Tsuneta et. al 1991). The same images were also used for direct area measurements.

For modelling the solar radio and X-ray data we used a software package TISMO (*TI*me-series *S*pot *MO*delling, Bartus, 1996) without major modification. In case of stars dark (cool) spots cause the rotational modulation, i.e. the star is fainter when the spot is facing towards us. whereas on the Sun in radio and X-rays we observe bright features. As it was mentioned already the amplitude of the flux variation caused by these bright spots are similar to those we observe on stars caused by dark spots, only the sign of the variability is opposite, i.e., the Sun is brighter in X-rays and radio when the active region is in view. That makes no difference using the spot modelling code. As in most cases of starspot modelling we used one- and two-spot fits. The free parameters were only the spot coordinates and sizes, other physical parameters like inclination, limb-darkening and, in the second step of our work the spot temperature was fixed (about varying spot temperature see the next section).

3. Results

3.1. Models compared to the images

The solar flux measurements together with the two-spot fit are displayed in Figure 1 both in radio and X-ray wavelengths. An example for the comparison between the model and the image is given in Figure 2.

It is well seen from Figure 1 that the rotational modulation given by the one-dimensional data is well approximated by the model. The place and size of the resulting main spot agrees with the image in both wavelengths (Figure 2), where, during the modelling, spot latitudes were fixed to the solar equator.

We made several test runs for the August-October part of the dataset, when only a single active region existed on the Sun. The main task was, as mentioned earlier, to test the reality of photometric starspot modelling. The procedure and the results are given in details in Paper I. We made spot solutions with the code TISMO on solar one-dimensional measurements and compared the results with the direct images made on similar wavelengths. Our most important findings were as follows:

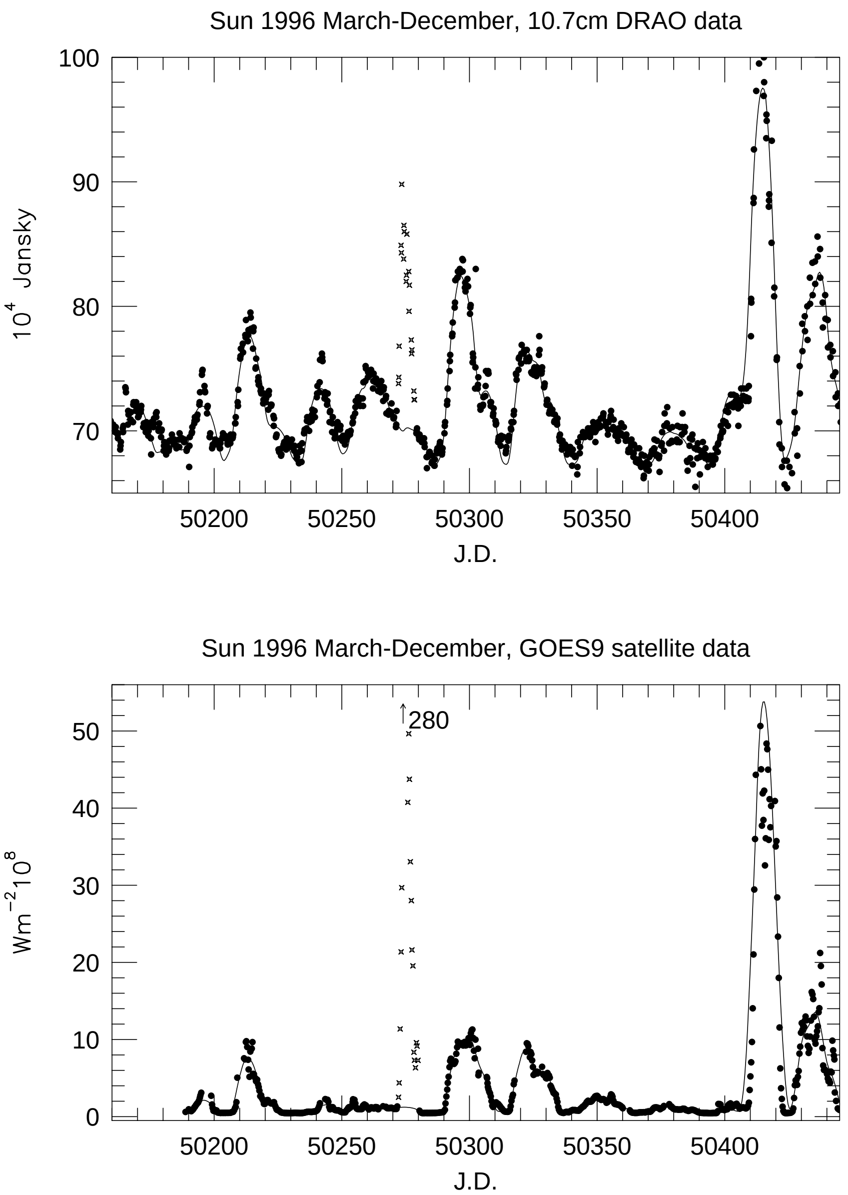

Figure 1: Fitted solar radio (up) and X-rays (bottom) data, March-December 1996. The emergence of the new active region at the beginning of July is plotted by crosses; the latter event was very fast and was not modelled by TISMO.

1. When all the spot coordinates (longitudes and latitudes) and spot sizes were free parameters in the modelling, we found artificially high latitude spot(s) both in the one- and two-spot models. To account for the general (long-term) variability this result is inevitable, since a (changing) spotted area that shows no rotational modulation is necessary, and its proper place is the polar region of a star or of the Sun. (It is noteworthy that the high latitude spots are commonly resulting both in photometric and spectroscopic (Doppler Imaging) starspot modelling. The reality of those results should be strenghtened by independent observations (direct images!) and theoretical considerations.

2. In most cases using two spots is enough to model the deviations from pure sinusoidal light curves (see for more details Kővári and Bartus 1997). However, when a resulting spot is small, it can be put nearly anywhere in the star (with other words

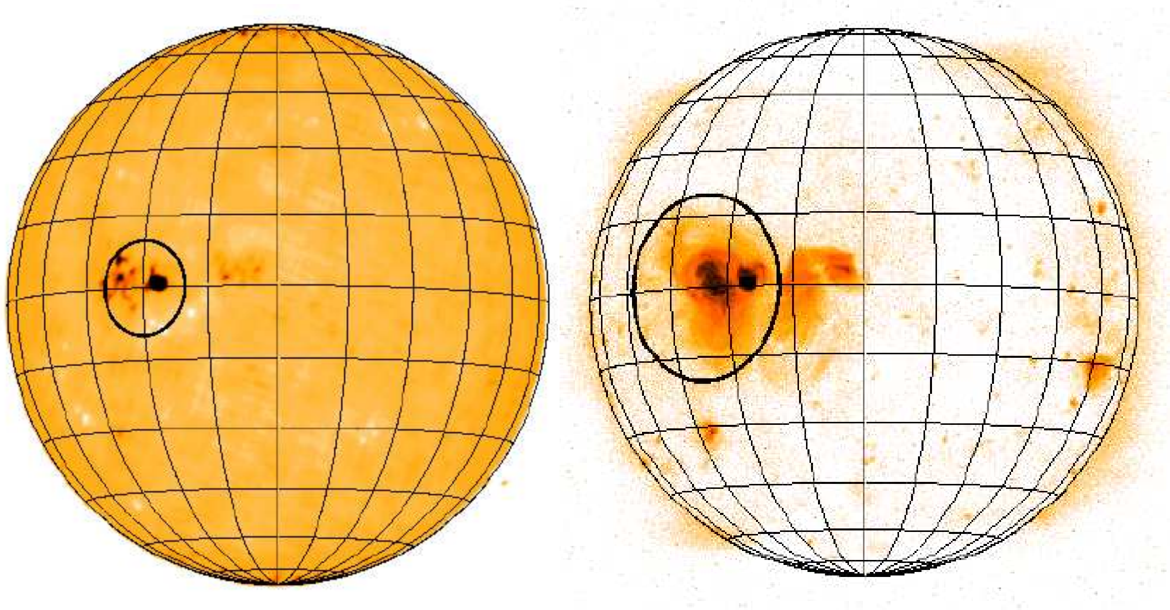

Figure 2: Solar radio (left) and X-ray (right) images overlayed with results of spot modelling on May 11, 1996.

its coordinates are totally unstable), especially in case of high latitudes. These small spots can account for short living spots at different locations on the stars that modify the light curves. Only clearly double-humped light curves caused by two (modelled) spots of similar size suggest two active longitudes with certainty.

3. The spot area could be derived with the highest accuracy using photometric spot modelling. Using the solar one-dimensional data, the modelled spot areas are close to the areas measured on direct images, provided that the intensity of the undisturbed surface and the flux ratio between that and the active region is well known. If we observe systematic changes in spot areas (growing or shrinking spots), that, beside the real area changes, could also mean changes of the flux ratio (warming or cooling active region). The flux ratio and its changes are of crucial importance and is discussed in detail in the next section.

3.2. The flux ratio problem

During the first test runs modelling the August-October dataset, when only one major active region existed on the Sun, we used a constant flux ratio that was calculated using a typical large active region size (5%) and average intensity ratios between the spot and the background given by the measurements. We found that the area of the resulting spot was decreasing in time between August-October. The images, on the contrary, showed that the area of the bright region was growing, as usual, when an acive region is aging. We found that the average temperature difference between the surface and the disturbed area was continuously decreasing, following approximately a hyperbolic function. We then took this change into account and modelled the data with changing flux ratio. The spot area results obtained this way were similar to those we got from direct measurements.

Using constant flux ratios is typical in starspot modelling, since the long datasets usually do not have appropriate colour information to derive spot temperature for each light curve for decades. We saw that the average contrast of a single active region to the background was continuously decreasing. On the other hand, we also know that inside a long-living active nest (or active longitude) the active regions are continuously born and decay. Supposing that during the lifetime of the active nest the temperature changes caused by emerging and decaying active regions were levelling up, we hoped that a constant flux ratio on a longer time-base would give reliable results. To test this hypothesis we modelled the active nest that existed on the Sun between March-December 1996.

We made direct area measurements both in radio and X-ray images on several days during the lifetime of the active nest. Using those areas and the one-dimensional measurements we calculated the flux ratios (FR) using the following expression:

$$\frac{\mathrm{I}}{\mathrm{I}_0} = \frac{FR \times \mathrm{A}_{\mathrm{spot}} + (\mathrm{A}_{\mathrm{disc}} - \mathrm{A}_{\mathrm{spot}})}{\mathrm{A}_{\mathrm{disc}}},$$

where I and I_0 were the spot and background intensities, and $\mathrm{A}_{\mathrm{spot}}$ and $\mathrm{A}_{\mathrm{disc}}$ were the areas of the active region and the solar disc, respectively. The background intensities were derived using the measurements on those days when no active region was visible on the Sun. We formed average flux ratios for the whole investigated time-base and modelled the one-dimensional dataset. Figures 3 and 4 show the results: the determination of the background intensities, the average flux ratios and the modelled area results compared to the direct measurements. The upper panels of Figures 3 and 4 show that the determination of the background intensity of the Sun is not straightforward. Even when no active area is seen on the solar disk, its X-ray and radio intensities are not constant. After the emergence of the large active region in July, an intensity increase was seen even on the other side of the Sun, half a rotation later. Moreover, the DRAO data, at least partly, were uncertain at the end of the year because of the low altitude of the Sun at the latitude of DRAO. The solar minimum occurred in mid-October 1996. Taking all these into account we fixed the unspotted intensity to the values given in Figures 3 and 4.

The flux ratio calculated using the above equation showed strong variability as the active regions emerged and decayed. In Figures 3 and 4 on the left side of the middle panels we also gave the extreme high values of this parameter. The hyperbolic decay of the flux ratio is seen starting around J.D. 50298, when only a large single active region was present on the Sun (for more details see Paper I). We calculated an average flux ratio that we could use in modelling the whole active nest. The highest values corresponding to active regions' emergence were left out of consideration when we made the averages, since extremely high flux ratio values would strongly distort the mean. Additionally, the time-scale of an active region emergence is very short (few days) comparing to the time-scale of the rotational modulation (27 days), and we did not calculate flux ratio values for each day of the observations.

The bottom panels of Figures 3 and 4 show the measured and modelled spot areas in percentages of the total solar surface. We got the modelled spot areas using the average flux ratios. The changes of the modelled spot areas thus follow the changes of the

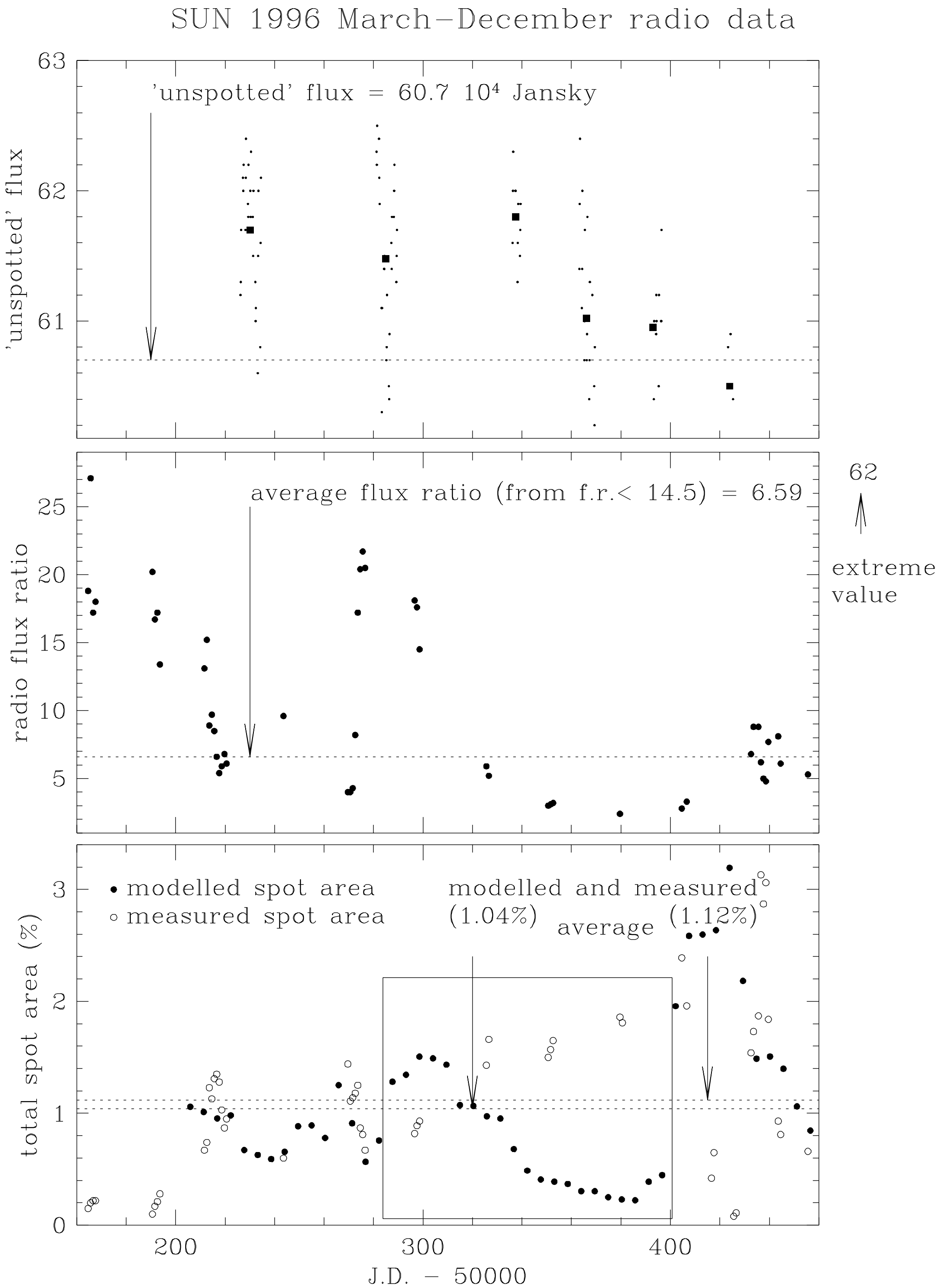

Figure 3: The unspotted flux (top), the flux ratio (middle) and the resulting spot areas in percents of the solar surface (bottom), in radio wavelength. A strong variability of the flux ratio is well seen. The resulted spot area varied following the flux ratio changes, since we used a constant flux ratio during the modelling. The measured and modelled spot areas disagree but their average values are very close to each other.

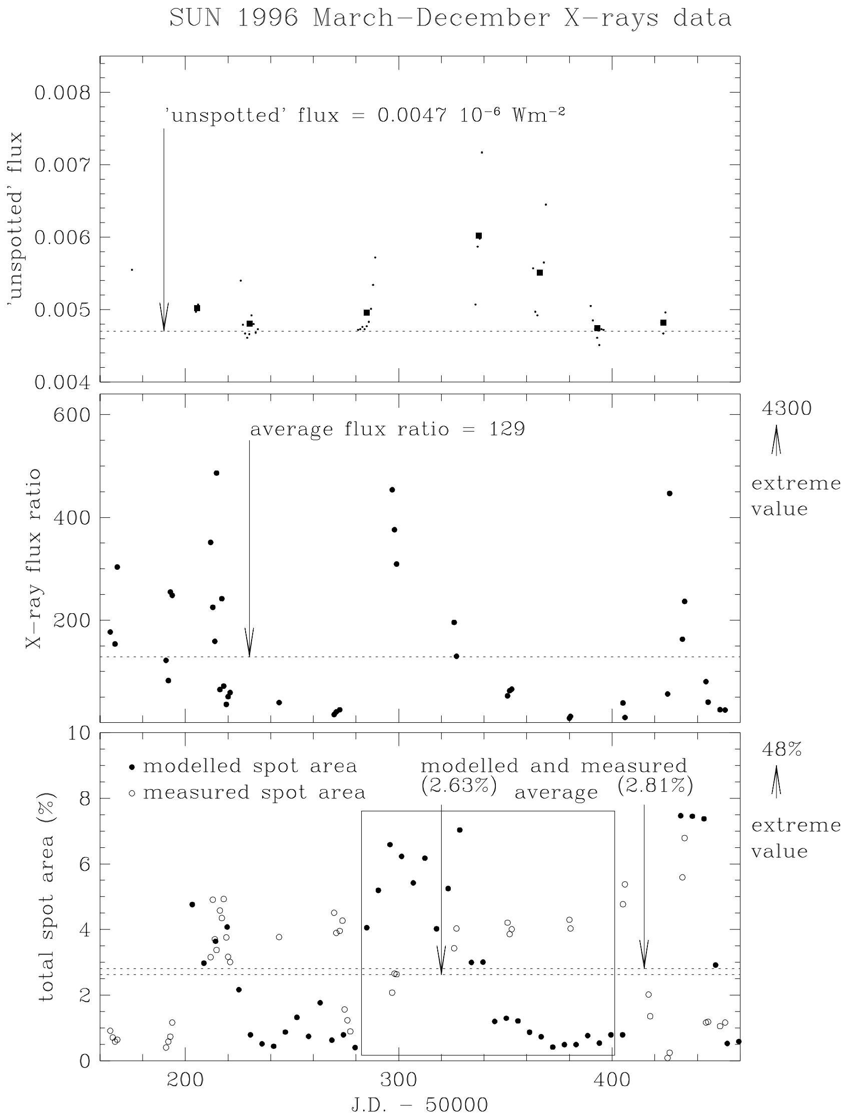

Figure 4: The same as in Figure 3, but in X-ray wavelength.

calculated flux ratios, but the averages of the modelled and measured spot areas between March-December 1996 are in good agreement. On the other hand, on a short time-base, using constant flux ratios, the resulting spot areas do not reflect the reality well. Figure 5 shows the results only for the August-October data that are marked with boxes in the bottom panels of Figures 3 and 4. During this time only a single active region was present on the Sun, and was decaying alone for four rotations. Using a constant flux ratio when modelling this part is grossly in error. If someone wishes to get a reliable spot area value for a single spot (and not for a complex where spots born and die), the variability in the flux ratio should be taken into account in the modelling. This way the spot area could succesfully be recovered (Paper I).

Our hypothesis thus turned out to be true: using constant flux ratios, starspot modelling could give reliable results on a longer time-base, when the changes of the flux ratios caused by the emerging and decaying spots level up each other.

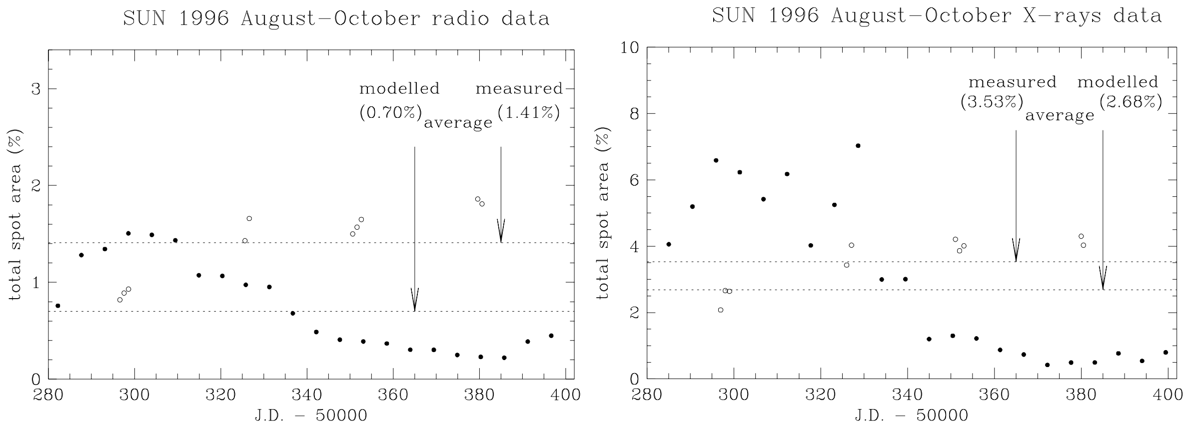

Figure 5: Details from Figures 3 and 4. The measured (open circles) and modelled (dots) spot areas are compared to each other in radio (left) and in X-ray (right) wavelength, only for the August-October 1996 dataset. The mean values of the measured and modelled spot areas disagree.

4. Summary

Using a stellar spot modelling technique on one-dimensional solar measurements and comparing the results with direct images we tested different aspects of photometric starspot modelling.

Recovering spot coordinates we found that long-term overall brightness variations (that are added to the rotational modulation) may result in artificially high latitude spots. The reason of this problem is that the overall brightness change requires spotted areas without rotational modulation, and to obtain this spots are placed to the polar region of the star by the modelling code. In two- or multi-spot models the coordinates of a resulting small spot (beside a big one) is totally unstable, and that can account for short living spots anywhere on the star.

We discussed the validity of using constant flux ratios when calculating photometric spot models of active stars. When we used one dimensional measurements and contemporaneous direct images of the Sun in radio and X-ray wavelengths we found a hyperbolic decrease in the flux ratio between the studied single active region and the undisturbed area (Paper I). On short time-scale the change of the flux ratio must be well known to succesfully recover spot areas. Using constant flux ratio may cause systematic change in spot size that could be partially due to flux ratio changes.

Using a longer dataset we studied the evolution of an active nest, between March-December 1996, as it was reflected in the total soft X-ray and radio emission of the Sun. For both wavelengths we investigated the flux ratios and their variations, and calculated the average flux ratio between the undisturbed background and the active nest as a whole that consists of old and new active regions together, at the same time.

Using the average flux ratio we could succesfully recover the average area of the active nest. Thus, if the stellar spots are analogous with active nests on the Sun, using constant temperature difference in spot modelling may give reliable results on the spot area changes on long time-scales.

Acknowledgements

The author is grateful to Dr. I. Jankovics, the Director, and to the staff of Gothard Observatory for the generous support to take part in the meeting, and who made the whole event unforgottable. I am indebted to Dr. L. van Driel-Gesztelyi, who helped me very much in understanding the solar activity features. She and Drs. Zs. Kővári and B. Szeidl critically read the manuscript. Support from OTKA T-026165 grant is acknowledged. Special thanks are due to the Sun, as the primary target of the present investigation, for performing the most spectacular event, the total eclipse.

References

Catalano S. et al. 1998, in: *Cool Stars, Stellar Systems and the Sun*, 10th Cool Star Workshop, Boston July 1997, Eds. R.A. Donahue and J.A. Bookbinder, p. 584

Hanaoka Y. et al. 1994, in: *New Look at the Sun with Emphasis on Advanced Observations of Coronal Dynamics and Flares*, Proc. Kofu Symposium, S. Enome & T. Hirayama (eds.), NRO Report No. 360, p. 35

Kővári Zs., Bartus J. 1997, A&A 323, 801

Nishio M. et al. 1994, in: *New Look at the Sun with Emphasis on Advanced Observations of Coronal Dynamics and Flares*, Proc. Kofu Symposium, S. Enome & T. Hirayama (eds.), NRO Report No. 360, p. 19

Strassmeier K.G., Bartus J., Cutispoto G., Rodonó M. 1997, A&AS 125, 11

Oláh K., van Driel-Gesztelyi L., Kővári Zs., Bartus J. 1999a, in: *Solar and Stellar Activity: Similarities and Differences* eds. C.J. Butler and J.G. Doyle, ASP Conference Series Vol. 158, p. 170–173

Oláh K., van Driel-Gesztelyi L., Kővári Zs., Bartus J. 1999b, A&A 344, 163 (Paper I)

Peres G. et al. 1998, in: *Observational Plasma Astrophysics: Five Years of Yohkoh and Beyond*, T. Watanabe, T. Kosugi & A.C. Sterling (eds.), Kluwer, p. 29

Tapping K.F., Charrois D.P. 1994, Sol. Phys. 150, 305

Tsuneta S. et al. 1991, Sol. Phys. 136, 37

Discussion

L. van Driel: Can we decide merely from stellar spot modelling whether stellar activity is due to one big AR, or a cluster of coming-and-going ARs?

K. Oláh: From photometric starspot modelling we cannot decide whether the light variability is due to one or two big AR('s), or several spots clustering in the stellar surface. Test results show that light curves generated by a lot of spots can well be modelled using two big spots (see Kővári and Bartus, 1997). On the other hand, using Doppler Imaging Technique on high dispersion spectra, details of the stellar surface can be recovered. The results show several spots that are coming and going, but these spots are still much larger than the sunspots. In case of simultaneous photometric and spectroscopic spot modelling the spectroscopic result may give positions of 2-3 activity centers, or clusterings of spots, that the photometric modelling describes by 2-3 single spots.

Radio observations of the Sun at Nançay

W. van Driel

Unité Scientifique Nançay, Observatoire de Paris, France

Abstract. At the Nançay Radio Observatory, in central France, observations of the Sun have always been performed since its foundation in 1952. At present, two main instruments, the Radioheliograph and the Decametric Array, are used for monitoring solar activity, as well as a few smaller monitoring antennas. The Radioheliograph is a unique 43-element interferometer dedicated to solar imaging in the metre wavelength range (0.6-2 m). Its powerful new correlator allows the imaging of the solar corona at a rate of 20 images per second in 5 frequency bands. Its rapid, multi-frequency capability enables the study of events in the corona between heights of about 0.1 to 0.5 solar radius. The Decametric Array is a unique 144-element interferometer dedicated to observations at very long wavelengths (3-30 m). At this instrument the upper solar corona is monitored at high time and spectral resolution.

Keywords: solar activity, flare, CME

1. Introduction

At the Nançay Radio Observatory, located 200 km due South of Paris, observations of the Sun have always been a constant activity from its foundation in 1952 (see also our Website http://www.obs-nancay.fr), as the Sun was the first celestial object to be studied at radio wavelengths by French physicists and astronomers, and a series of solar radio telescopes has since its beginning been erected on the Nançay site (see Figure 1). At present, two main instruments (the Radioheliograph and the Decametric Array) are used for monitoring solar activity, as well as a few smaller monitoring antennas.

Figure 1: Nançay – the early years (1955). Left: elements of the solar interferometer in use at the time, these dishes are still printed on the packages of the famous Nançay *sablé* shortbread cookies; to the right: one of the converted 8-meter German Wurzburg radar antennas buot in 1943, part of a large interferometer used to study Galactic structure.

2. The Radioheliograph

The radioheliograph (see Figure 2) is a unique 43-element radio interferometer dedicated entirely to solar imaging in the metre wavelength range (0.6-2 m). For more detailed descriptions of the instrument, see Kerdraon & Delouis (1997) and Radioheliograph Group (1993).

As a result of a long evolution initiated in 1982, it now consists of a cross-shaped multi-antenna array, comprising an East-West branch with 19 antennas along a 3.2 kilometer long baseline and a North-South branch of 24 antennas over a total length of 3 kilometer, with minimum baselines of about 50 meters. This configuration allows the two-dimensional imaging of the Sun with a beamsize of about 0.4 to 1.8 arcmin (at 0.6, resp. 2 m. wavelength) during summer months; during winter months the beam is more elongated in the North-South direction.

The rapid structural variations in the (radio) corona require fast imaging capabilities. It has recently been equiped with a digital correlator, which permits the true two-dimensional imaging of the solar corona, using all possible baselines of the T-shaped array, at a maximum rate of 20 images per second in each of 5 fixed wavelengths between 60 cm and 2 meter wavelength. Observations at different wavelengths probe different heights in the corona, in the case of the Nançay radioheliograph regions between 0.1 and 0.5 solar radius above the visible surface.

It is an instrument dedicated to solar observations, and presently the only instrument to provide the astronomical community with radio observations of the solar corona at metric wavelengths during 8 hours each day, all year round; the other dedicated solar radio telescope, at Nobeyama Radio Observatory in Japan, observes at much shorter, centrimetric, wavelengths which probe the solar atmosphere much closer to the visible surface, and other radio telescopes, like the Very Large Array (VLA) in the U.S.A. or the Giant Metre wave Telescope (GMT) in India, observe the Sun only infrequently, and have not been designed for such specialized observations of a highly variable, very intense radio source.

A series of radio images taken during the total solar eclipse of August 11, 1999, is shown in Figure 3. These images were made at the longest of the 5 wavelengths observed, 1.8 meter. These images clearly show the extension of the radio corona with respect to that of the optical disk (plotted as a white circle). The eclipse was about 95% in the optical at Nançay; the image taken at the maximum occultation (10:23 UT) shows the offset of the lunar shadow against the radio corona from the outline of optical disk. Clearly, any solar eclipse which is total in the optical will always remain annular at these radio wavelengths. Note the CME occuring around 09:43 UT.

Figure 2: Antennas of the North-South branch of the Nançay Radioheliograph, an interferometer dedicated to observations of the middle solar corona at metric wavelengths. The 5-meter diameter antennas operate between λ 0.6 and 2 meter.

Radioheliograph images are stored on CD-ROMS and made available on a daily basis to the astronomical research community through the BASS 2000 solar database (see Website http://mesola.obspm.fr/nancay2d.html).

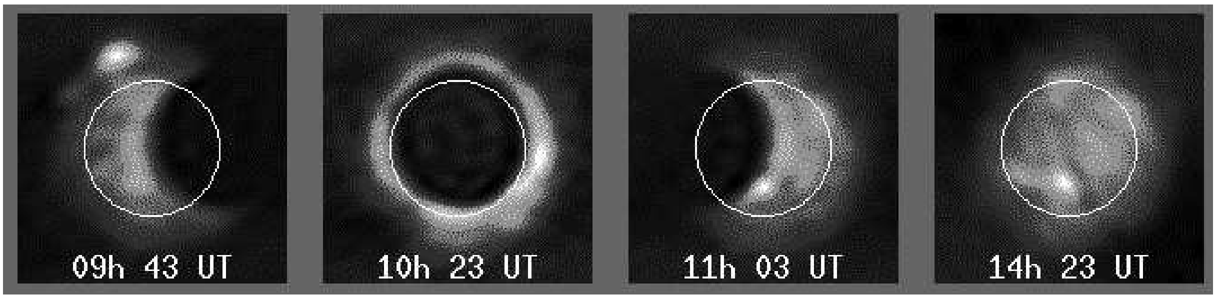

Figure 3: Radio images of the total solar eclipse of August 11, 1999, obtained with the Radioheliograph at 1.8 meter wavelength. The white circle denotes the size of the optical solar disk. Note that the lunar disk will never cover the entire solar radio image during any eclipse, as the middle solar corona (at a height of about 0.5 $R_\odot$ above the visible surface) is detected at this metric radio wavelength. The maximum occured at 10:23 UT; note the Coronal Mass Ejection (CME) occuring around 09:43 UT.

The Radioheliograph imaging data provide a complementary, radio view of events like flares and coronal mass ejections (CMEs – see Figure 3); e.g., Maia (1999) and Pick et al. (1999). Comparison with observations made in other wavelength domains, from the ground as well as with spacecrafts (like ULYSSES, SOHO, YOHKOH and TRACE), combined with modelisation of the underlying magnetic field structures and their evolution allow a fuller understanding of solar physics (e.g., Manoharan et al. 1997).

3. The Decametric Array

The Decametric Array (see Figure 4) is a unique 144-element interferometer dedicated to radio observations at the longest wavelengths (3-30 m) which can still penetrate the Earth's ionosphere (even longer wavelengths are reflected back into Space by the ionosphere). With this instrument the upper solar corona is monitored when there are no ongoing observations of the radio activity of Jupiter. At these long wavelengths the solar corona cannot be resolved by it, which is compensated by high time-resolution over a broad frequency range.

The Decametric Array is dedicated to the study of the magnetic and ionized environment of the Sun and planets (mainly Jupiter). In these plasmas not only the low-frequency emission (decametric radio waves) detected with the Decametric Array are produced, but also very low frequency emission (at kilometric wavelengths, observable by spacecraft only; e.g., Barrow et al. 1996) and ultraviolet radiation (planetary aurorae, observed with the HST; e.g., Prange et al. 1998). The radio observations show a variety of phenomena (down to time scales of less then a second: the so-called millisecond bursts of Jupiter, and solar and stellar eruptions) which allow the study of the dynamics of these ionized plasma environments.

Figure 4: The Decametric Array consisting of 144 antennas. The 144 "teepee" type antennas are fixed and pointed towards the South, where the Sun and Jupiter can be observed. Their field of view is very large (about 60°, pointing and tracking is done completely electronically.

The Decametric Array, developped in the years 1975-1978, is an interferometer consisting of 144 antennas of 9 meter high and 5 meter in diameter at their base, distributed over an area of 10,000 square meter. The 8 conducting wires on each antenna have been wound in a spiral pattern on a conical surface - giving them the nickname of teepee antennas, after the American-indian conical tents. The wires on the antennas are wound in either a left- or a right-handed winding spiral pattern, making them sensitive to either left- or right-hand circularly polarized radio waves. Thus, the Decametric Array exists in fact of two sub-arrays of 72 antennas each, and is capable of measuring circular polarisation, which is very important since the radiation from Jupiter is highly polarized. The broad-band spectroscopy of the emissions, often very variable, requires specialized, very fast receivers which can take several thousand measurements per second.

The principal beam, i.e. the spatial resolution, has a size of 7 by 14 degrees - large compared to the actual size of a few degrees for the solar corona or only a fraction of a degree for Jupiter's magnetosphere, as seen from the Earth. This "nearsightedness" remains the weak point of observations at such long wavelengths (except for very-long baseline interferometry, VLBI). It does not permit detailed imaging and prevents therefore the localization of the radio emission in or near the observed radio source. Fortunately, this lack of spatial resolution is compensated by the high frequency and time resolution of the observations made with the Decametric Array.

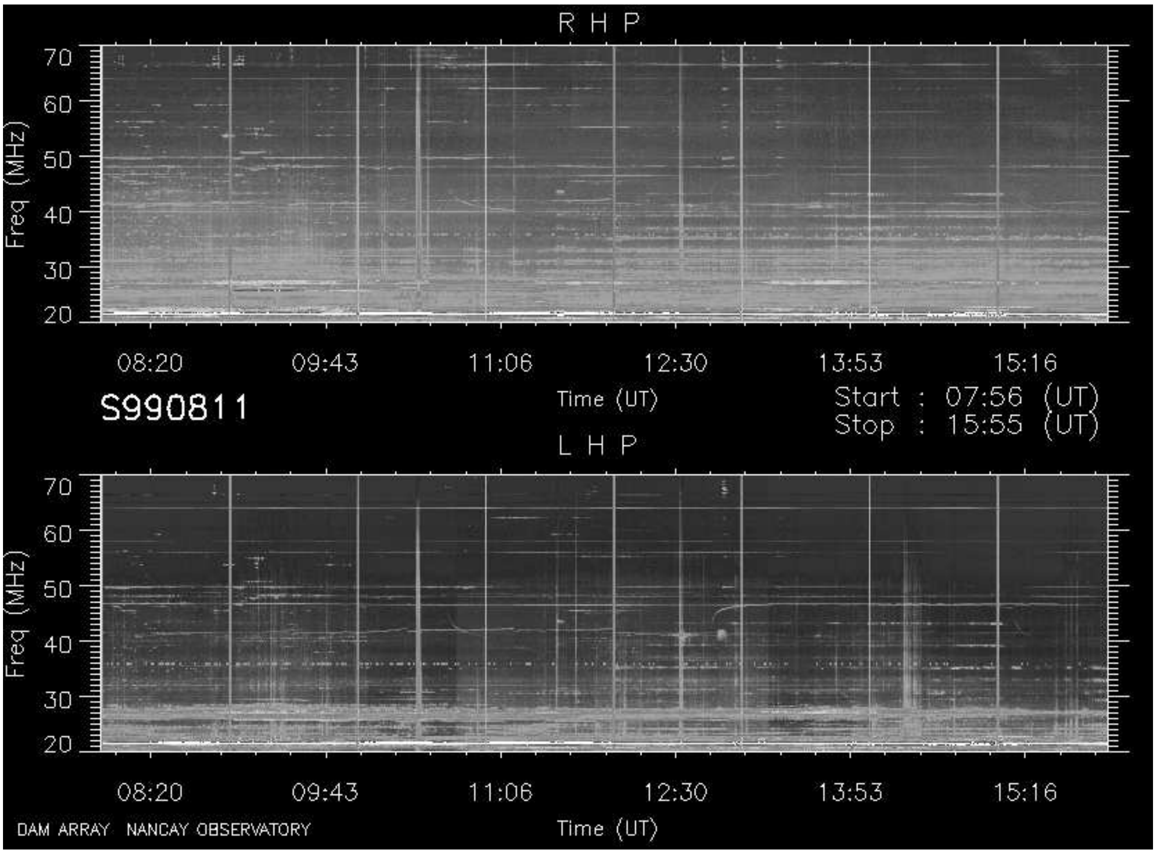

Figure 5: Dynamic spectra of the Sun made with the Decametric Array during the day of the total solar eclipse of August 11, 1999. The vertical axis shows frequency, the horizontal axis time and the greyscale indicates the intensity of the emission. Observations were made in two polarisations: left-hand (LHP) and right-hand (RHP). The lunar disk occults only a small fraction of the upper solar corona detected at these very long radio wavelengths, hence the effect of the eclipse at these wavelengths is much less clear than in the images obtained with the Radioheliograph. The maximum occured at 10:23 UT.

Far prior to any other wavelength domains, decameter wave radioastronomy became a challenging task because of man-made radio interference due to the increasing needs in telecommunications. However, most of the astrophysical studies in this frequency band – particularly those of non-thermal radiations from magnetized objects – require high gain, multi-polarisation antennas and the use of high sensitivity, high dynamic range spectroscopy techniques. Actually, the observations are essentially digital, and made with four complementary receivers, including:

A frequency-sweeping spectral analyzer (ASB): this provides us with systematical broadband observations of the Sun and Jupiter, with a time resolution of about 1 second, during about 6 to 8 hours per day around the meridian passage of each object. It records both left- and right-hand polarized radiation. The observed data (1 to 3 Mbyte per hour) are stored on CD-ROMs and made available to the scientific community (see the Website http://www.obs-nancay.fr/quest/index_se.htm). As an example, the routine observational solar data are shown here (Figure 5) for August 11, 1999, the day of the total solar eclipse.

Digital receiver: a new generation of wide band spectrum analyzers, well suited to overcome the interference constraints, are presently being developed. They are based on the utilization of newly available, high performance, programmable digital circuits for signal processing, arranged in an architecture which can directly compute the power spectrum of the input signal (e.g., Lecacheux et al. 1998). The possibility of processing the telescope signal in real time appears a key to maintaining acceptable sensitivity in an increasingly 'hostile' radio electric environment. The bandwidth of the prototype receiver will be increased and more sophisticated algorithms will be developed for the recognition and elimination of interference, both in real time and for further off-line data reduction.

Acknowledgements

The Nançay Radio Observatory, the Unité Scientifique Nançay of the Observatoire de Paris, is associated as USR No. B704 to the French Centre National de Recherche Scientifique (CNRS). Nançay also gratefully acknowledges the financial support of the Région Centre in France and of the European Union.

References

Barrow C.H., Woan G., Macdowall R.J. 1996, Astron. Astrophys. 316, 413

Kerdraon A., Delouis J-M. 1997, Lecture Notes in Physics 483

Lecacheux A., Rosolen C., Clerc V., Kleewein P., Rucker H.O., Boudjada M., van Driel W. 1998, Proc. SPIE Vol. 3357, Advanced Technology MMW, Radio, and Terahertz Telescopes, Ed. Thomas G. Phillips, p. 533

Maia D., Pick M., Kerdraon A., Howard R., Brückner G.E., et al. 1998, Solar Phys. 181, 121

Manoharan P.K., van Driel-Gesztelyi L., Pick M., Démoulin P. 1997, Astrophys. J 468, L73

Pick M., Maia D., Kerdraon A., Howard R., Brückner G.E., et al. 1998, Solar Phys. 181, 455

Prange R., Rego D., Pallier L., Connerney J.E.P., Zarka P., Queinnec J. 1998, Journal of Geophysical Res. 103, 2664

Radioheliograph Group 1993, Adv. Space Res., 13, 94

The influence of an inclined rotation axis on solar irradiance variations

R. Knaack[1], M. Fligge[1], S.K. Solanki[1,2], Y.C. Unruh[3]

[1] Institute of Astronomy, ETH Zentrum, CH-8092 Zürich, Switzerland
[2] Max-Planck Institut für Aeronomie, D-37191 Katlenburg-Lindau, Germany
[3] Institute of Astronomy, University of Vienna, Türkenschanzstr. 17, A-1180 Vienna, Austria

Abstract. The irradiance variations of the Sun over the solar cycle are relatively small compared with sun-like stars (Radick et al., 1998). It has been proposed that a random distribution of stellar rotation axes relative to the ecliptic plane could explain their larger variability (Schatten, 1993). We examine the influence on total irradiance variations of the inclination of the solar rotation axis relative to an observer. A three-component model is used to calculate the relative flux variations of a given distribution of active regions on the surface of the Sun as a function of the inclination. One component is the quiet Sun, another is a sunspot component and the third describes the faculae. We find that the inclination effect increases the total irradiance variations of the Sun maximally by 40%. The most probable value is approximately 5%. This is much less than former studies (Schatten, 1993, Radick et al., 1998) suggested.

1. Introduction

The total irradiance of the Sun exhibits a prominent eleven-year cycle, which is correlated to the sunspot cycle. The cyclic variation of solar total irradiance, which has an amplitude of about 0.1% (Fröhlich & Lean, 1998), is caused by the small imbalance between the excess flux of faculae and the flux deficit of sunspots (Foukal & Lean, 1998). Compared with sun-like stars, the long-term photometric variations of the Sun are subdued by a factor of 2–3 (Lockwood et al., 1992, Radick et al., 1998). One possible explanation [Schatten 1993] might be the special position of a terrestrial observer which confines solar active regions to low and intermediate latitudes. An observer high above the ecliptic plane, however, would see a different distribution of sunspots and faculae, i.e. the active regions would appear closer to the limb, as is shown in Figure 1 for two zonal bands. This affects the observed solar irradiance and its variations, mainly because white-light faculae are better seen at the limb than at disk centre whereas the Wilson depression reduces the visibility of sunspots near the limb. Altogether, an increase of the total irradiance variation is expected when viewing the Sun out of the equatorial plane. Taking into account a random distribution of stellar rotation axes relative to the ecliptic plane, this inclination effect should enhance the apparent variability of sun-like stars.

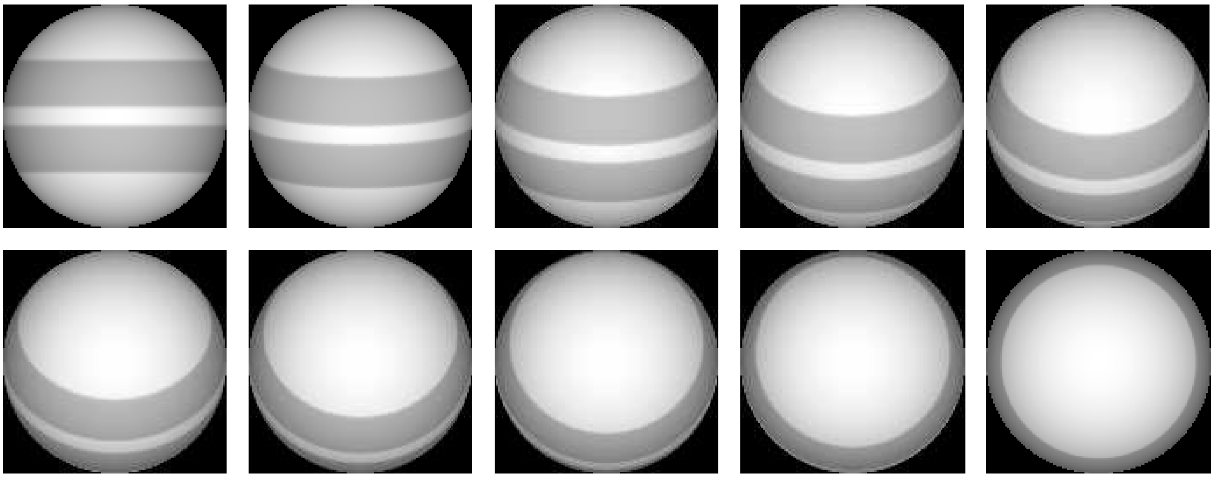

Figure 1: The geometric effect of a rotation axis tilted relative to the observer for two zonal latitude bands between $\pm 5°$ and $\pm 30°$. The inclination i decreases in steps of $10°$ from the upper left ($i = 90°$) to the lower right ($i = 0°$).

In order to calculate the relative flux variations caused by active regions as a function of inclination, the intensity as a function of limb angle has to be known for the faculae, sunspots and the quiet Sun. For this purpose we use a three component model according to Unruh et al. [1999], which is introduced in the next section and was originally proposed by Solanki & Unruh [1998].

2. The model

The model consists of three components, namely quiet-sun, faculae and spots. In order to calculate intensities and limb-dependent contrasts for each of these components under the assumption of LTE, Kurucz's ATLAS9 program was applied (Kurucz, 1992, Castelli & Kurucz, 1994). The quiet-sun intensities were obtained by Kurucz's solar model atmosphere with $T_{\rm eff} = 5777$ K. The spot intensities (averaged over umbra and penumbra) were calculated from a model atmosphere of 5150 K which in turn was interpolated from the Kurucz grid of model atmospheres. This temperature corresponds to a ratio of umbral to penumbral area of approximately 1:3.

Model P of Fontenla et al. [1993] was used as a starting point for the facular model. Slightly modified, this model was remarkably successful in fitting the spectral irradiance variations and also data obtained by VIRGO (see Unruh et al. 1999 and Fligge et al. 1999 for details).

In principle, this model allows us to calculate the inclination effect for any wavelength range between 160 nm and 160'000 nm. In this publication, however, only the total wavelength range is considered. The resulting contrasts C for spots and faculae are shown in Figure 2 as a function of $\mu = \cos\theta$, with θ being the heliographic angle between the observer and the normal to the Sun's surface. The contrast is defined by

$$C_{\mu,\Lambda} = \frac{\int_\Lambda I_\mu(\lambda)\, d\lambda}{\int_\Lambda I_\mu^{qs}(\lambda)\, d\lambda} - 1 \qquad \mu \in [0,1],\ \lambda \in \Lambda\,, \tag{1}$$

where the integration runs over the total wavelength range Λ. I_μ denotes the intensity spectra of spots or faculae, I_μ^{qs} stands for the intensity spectrum of the quiet Sun. Obviously the spot contrast remains practically constant, if foreshortening effects like the Wilson depression are neglected.

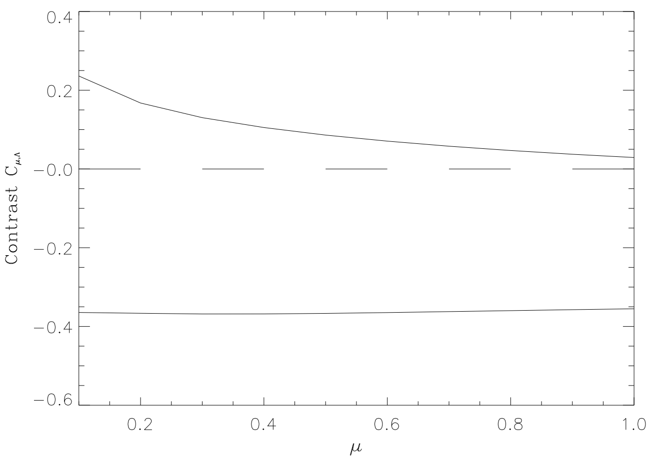

Figure 2: Facular contrast ($C_{\mu,\Lambda} > 0$) and spot contrast ($C_{\mu,\Lambda} < 0$) vs. μ for the total wavelength range $\Lambda = [160\,\mathrm{nm}, 160'000\,\mathrm{nm}]$.

3. The inclination effect

We modified a Doppler imaging code written by A. Collier Cameron (see e.g. Collier Cameron 1997), to calculate the relative flux variations of a given distribution of faculae and spots on the surface of the Sun as a function of the inclination i. For this purpose, we placed in each hemisphere a facular and a sunspot belt, each totally smeared in latitude. This approximation neglects short-term variations due to the rotation of the Sun. The facular and sunspot belts were then filled with a certain percentage of faculae and spots, thereby fixing the total facular and spot coverage, A_f and A_s, respectively. Denoting the fluxes of the quiet Sun, the sunspots and the faculae with F_{qs}, F_s and F_f, the relative flux variation becomes

$$\frac{\Delta F}{F} \equiv \frac{F_{tot} - F_{qs}}{F_{qs}} = \frac{F_s + F_f}{F_{qs}}, \tag{2}$$

where $F_{tot} = F_{qs} + F_s + F_f$ is the sum over all three components.

We first tried to reproduce the inclination effect as predicted by Schatten [1993] or Radick [1998] to test our program. The results are shown in the next two subsections.

3.1. Schatten's prediction

Schatten [1993] used the active-region model of Sofia et al. [1982], where the limb-darkening and the contrast of faculae and sunspots are described by polynomials of second degree. The coefficients for the contrast functions were obtained by least square fits to the ACRIM data in the early 1980s. To investigate the inclination effect, Schatten placed groups of small individual faculae and spots within two bands ranging from 10° to 40° on each hemisphere. The areas were adjusted to provide a cyclic variation of about 0.18%, which is about twice as much as the value of 0.1% suggested by Fröhlich and Lean [1998]. The facular-to-spot flux ratio was fixed to about 5:4. The influence of the inclination on the relative flux variation obtained by Schatten is shown on the upper left diagram of Figure 3. We define here the inclination i as the angle between the solar rotation axis and the line-of-sight. The relative flux variation $\Delta F/F$ (bold line) starts at 0.18% ($i = 90°$) and increases up to 1.1% ($i = 30°$), i.e. a factor of 6 higher, followed by a pronounced decline. The statistically most probable value for the increase, corresponding to an inclination of approximately 57° (Radick et al., 1998), is a factor of about 3. The dotted line shows the contribution of the spots (F_s/F_{qs}) and the dashed line the contribution of the faculae (F_f/F_{qs}).

The upper right diagram of Figure 3 shows our calculations. We employed the same limb-darkening function for the undisturbed photosphere as Schatten and the same contrast functions for the active regions. We placed our bands for faculae and spots between 10° and 40° in each hemisphere. It was necessary to use very large values for the facular and spot areas to fulfil Schatten's boundary conditions of $\Delta F/F = 0.18\%$ and $F_f : F_s = 5 : 4$, namely $A_f = 34\%$ and $A_s = 2.4\%$, which is a factor of about 10 larger than observations of the active Sun imply. In agreement with Schatten we then obtain a maximal increase between $i = 90°$ and $i = 0°$ of a factor of 6, the value for the most probable inclination is a factor of about 2. The obvious qualitative difference between Schatten's result and our reproduction is probably due to the different distributions applied. Schatten has employed discrete groups of active regions whereas we have used zonal bands, that have been smeared between 10° and 40° latitude as well as over all longitudes.

As a next step we replaced the limb-darkening function of the quiet Sun and the contrasts for the spots and faculae with the calculated intensity spectra of our model and tuned the relative flux variations to fulfil Schatten's boundary conditions. The values needed were $A_f = 14\%$ and $A_s = 1.9\%$, which is still too much but remarkably less than above. The result is shown in the lower diagram of Figure 3. The variation increases now maximally by a factor of 2.7, in the most probable case, however, only by a factor of 1.3.

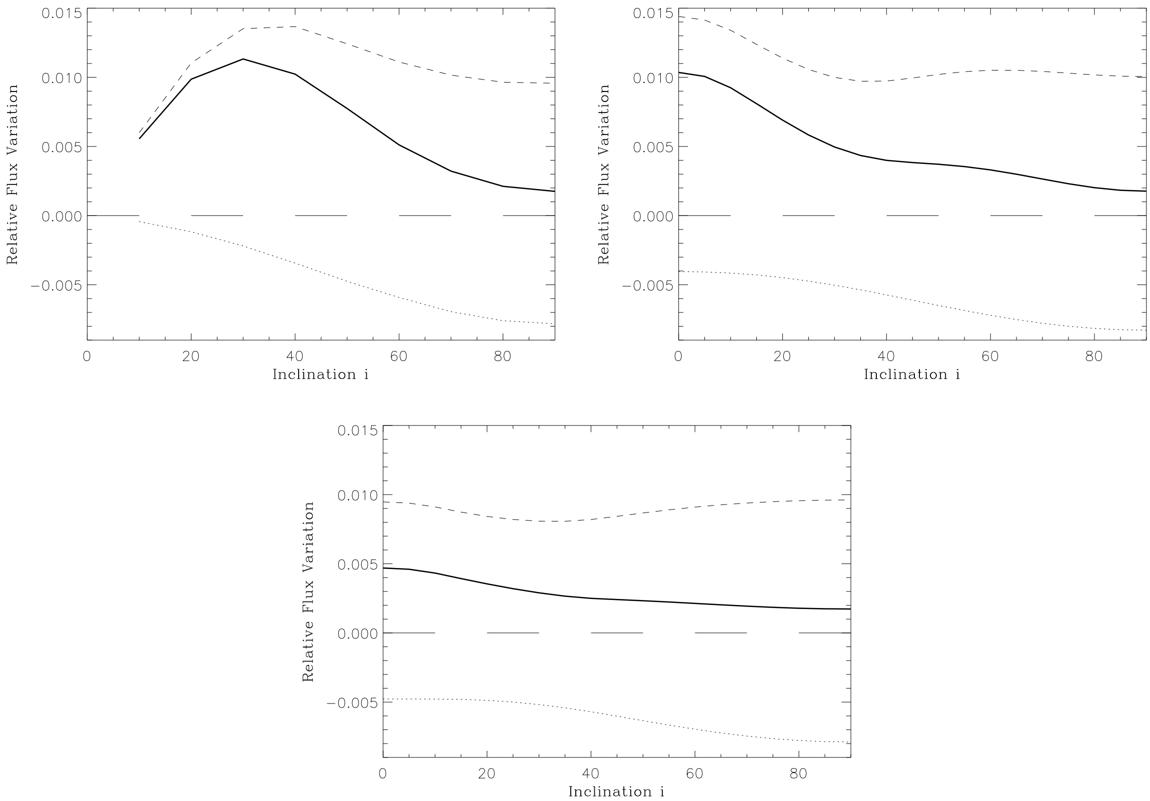

Figure 3: Relative flux variation $\Delta F/F = (F_s + F_f)/F_{qs}$ vs. inclination i (bold line) and the contribution of spots (F_s/F_{qs}; dotted) and faculae (F_f/F_{qs}; dashed). The diagram on the upper left shows Schatten's results for an initial variation of 0.18% and a flux ratio of $F_f/F_s = 5:4$ ($i = 90°$), using limb-darkening and contrast functions as described in the text. The diagram on the upper right is our reproduction under the same boundary conditions and for the same limb-darkening function and contrasts. There is a qualitative discrepancy due to different active-region distributions, but the maximum values $\Delta F/F \approx 1.1\%$ agree. The lower diagram has been calculated by replacing the limb-darkening and the contrast functions with the spectra of our model. The increase of $\Delta F/F$ is already much smaller.

Our model hence predicts a much smaller inclination effect, even if we employ Schatten's cyclic variation of 0.18% and his flux ratio of 5:4.

3.2. Radick's prediction and our results

Radick et al. [1998] applied the same limb-darkening and contrast functions as Schatten. They used an initial cyclic variation of 0.10% and a flux ratio of 2 : 1. The sunspot belts were confined to a band between 15° and 30° in each hemisphere. The facular zones ranged between 5° and 40°. These distributions were smeared completely in latitude, similar to our model. Under these conditions they found a most probable cyclic variation of 0.136% (i.e. at an inclination angle of 57°) and a maximum increase by a factor of about 2.

Again we tried to reproduce their results by employing exactly the same boundary conditions and the same limb-darkening and contrast functions. Because of the equivalent use of smeared distributions we expected better accordance this time. The left diagram of Figure 4 shows our reproduction for $A_f = 7\%$ and $A_s = 0.28\%$. We calculated a most probable variation of 0.133% and a maximum variation of 0.231%, i.e. a factor of about 2. This is in good agreement with Radick et al.

The disagreement between Schatten's prediction and the one of Radick et al. is a first clue that the inclination effect might not explain the larger variability of sun-like stars. Our calculations have introduced the spot and facular areas as a new criterion to determine the plausibility of the assumptions made by Schatten or Radick et al. Schatten's boundary conditions required an unrealistically large area for the active regions. The values assumed by Radick et al. imply a spot area of 0.28% and a ratio of $A_f/A_s = 25$. While the spot coverage of 0.28% implies a very active Sun, the facular to spot ratio is typical for a solar minimum. Measurements made during solar cycle 22 by Chapman et al. [1997] suggest a ratio of $A_f/A_s \approx 14$ and a spot area of $A_s \approx 0.2\%$ during maximum activity.

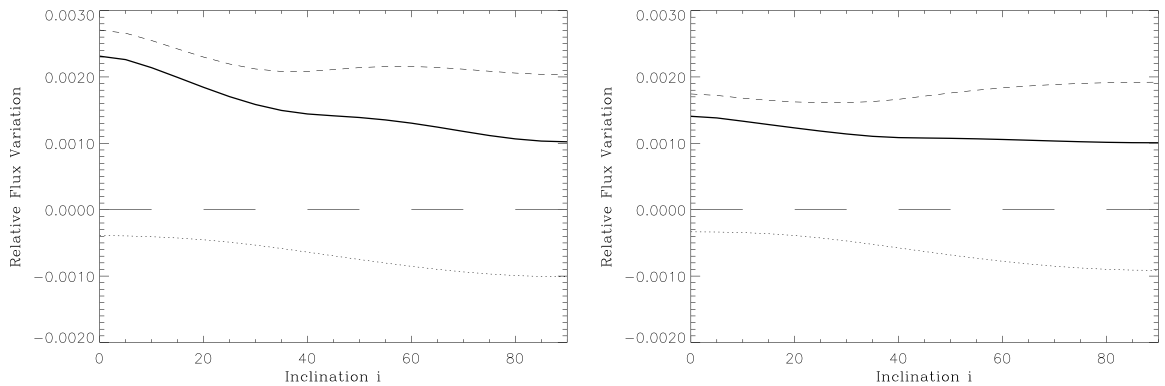

Figure 4: The left plot shows our reproduction of the inclination effect on the relative flux variations $\Delta F/F = (F_s + F_f)/F_{qs}$ (bold), F_s/F_{qs} (dotted) and F_f/F_{qs} (dashed) according to Radick et al. The right plot shows our prediction of the inclination effect, which has been calculated with the intensity spectra of our model (see text for details).

In addition, butterfly diagrams show that during activity maximum, sunspots are mainly confined to a band between 5° and 30° in each hemisphere. We hence fixed our sunspot belts in accordance with these observations and allowed the associated faculae to range between 5° and 40°. According to the observations, the spot area was fixed to $A_s = 0.20\%$ and the cyclic variation at $i = 90°$ was set to 0.10%. This yields a facular area of $A_f = 2.80\%$ and a facular to spot ratio of 14, which agrees well with what is observed for the Sun. The diagram on the right of Figure 4 shows the inclination effect calculated with our model.

We obtain a most probable amplitude for the cyclic variation of 0.106% and a maximum amplitude of 0.141%. These variations are much smaller than the values of Radick et al. This is mainly due to our different centre-to-limb variations of the facular contrasts. Radick et al. tried a second facular contrast function and found a most probable variation of 0.117% which is closer to our result. Further investigations with our model showed that changes in the spot contrast function hardly affect the gradient of $\Delta F/F$ relative to the inclination angle i, whereas changes in the facular contrast do have a great influence.

4. Conclusion

We have found that the inclination effect for the total irradiance variations of the Sun has been overestimated. Figure 5 shows our prediction in comparison with the calculations considering the model and boundary conditions used by Radick et al. [1998] and Schatten [1993]. It is very unlikely that the Sun's offset in terms of its irradiance variations (see Fig. 1b) is due to an inclination effect. We find that for a star with a similar active-region distribution as the Sun, the increase in its irradiance level does not exceed a factor of 1.5. We also find that the amount of the flux increase depends sensitively on the facular contrasts. For our input parameters, variations of the order of 10% for both the spot filling factor and the total irradiance variations resulted in a range of 1.3 to 1.5 for the maximum flux change with inclination.

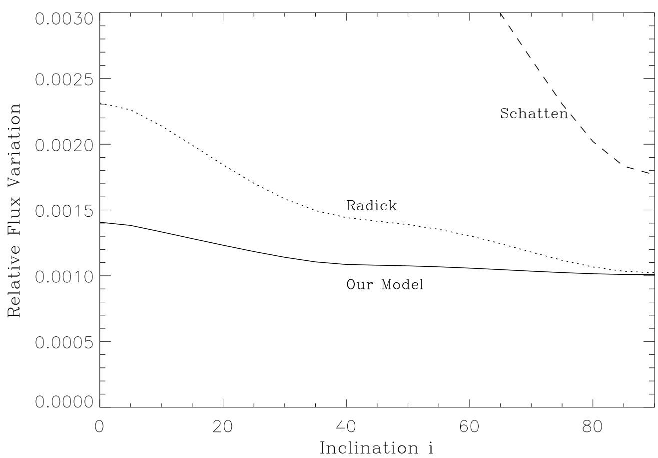

Figure 5: The inclination effect calculated with our model, respectively with the model used by Schatten and Radick.

References

Castelli, F., Kurucz, R.L. 1994, A & A, 281, 817
Chapman, G.A., Cookson, A.M., Dobias, J.J. 1997, ApJ, 482, 541
Collier Cameron, A. 1997, MN, 287, 556
Fligge, M., Solanki, S.K., Unruh, Y.C., Fröhlich, C., & Wehrli, C. 1998, A & A, 335, 709
Fontenla, J. M., Avrett, E. H., & Loeser, R. 1993, ApJ, 406,319
Foukal, P., & Lean, J. 1988, ApJ, 328, 347
Fröhlich, C. & Lean, J., Geophys. Res. Lett., 25, 4377
Kurucz, R.L. 1992, Rev. Mex. Astron. Astrofis., 23, 45
Lockwood, G.W., Skiff, B.A., Baliunas, S.L., & Radick, R.R. 1992, Nature, 360, 653
Radick, R.R., Lockwood, G.W., Skiff, B.A., & Baliunas, S.L. 1998, ApJS, 118, 239
Schatten, K.H. 1993, J. Geophys. Res., 98, 18907

Sofia, S., Oster, L., Schatten, K.H. 1982, Sol. Phys., 80, 87
Solanki, S.K., & Unruh, Y.C. 1998, A & A, 329, 747
Unruh, Y.C., Solanki, S.K., & Fligge, M. 1999, A & A, 345, 635

The spatial distribution of EUV emission in active regions

S.A. Matthews[1], J.A. Klimchuk[2], L.K. Harra[1]

[1] Mullard Space Science Laboratory, University College London, Holmbury St. Mary, Dorking, Surrey RH5 6NT, U.K.
[2] Space Science Division, Code 7675, Naval Research Lab., Washington D.C. 20375-5352, U.S.A.

Abstract. The full version of this paper will be published elsewhere. We give here only an extended abstract.

In order to understand fully how active regions are heated we need not only to be able to find a mechanism that will meet the observed energy requirements, but also to be able to explain the thermal structure of the region. Previous studies of active region structure and dynamics have indicated that there are significant differences in the properties and relationships between structures of different temperatures. For example, it has become clear that non-thermal velocities, Doppler flows and dynamics or time variability of high arching cooler loops are much greater than in hotter loops.

Using observations from the Coronal Diagnostic Spectrometer (CDS) on SoHO and the Soft X-ray Telescope (SXT) on *Yohkoh* we investigate how some of the properties of active region loops observed in the EUV and X-ray range vary with temperature. We examine the spatial distribution of the emission using correlation techniques and Fourier methods with which we obtain the two dimensional power spectrum of the intensity distribution for a number of lines at different temperatures. Integrating this over polar angle we find isotropic power-law behaviour at all temperatures in a number of topologically different active regions, with a tendency for flatter spectra at lower temperatures. The existence of power-law spectra indicates that there is no preferred length scale within the regions, while flatter spectra at lower temperatures indicate that the structures are relatively smaller in this temperature range, possibly providing support for the idea of a multi-component transition region (TR).

Our results show that a change in behaviour of the plasma can be found between temperatures of approximately < 5.9 in the log and > 5.9 when we take correlations between intensity maps at adjacent temperatures and relative to the coolest line in our disk studies. This behaviour is seen for four different active regions and appears to be independent of position on the disk. The contrast of loops on the limb and on the disk relative to the background emission also shows a similar difference in these two temperature regimes, remaining uniformly low at higher temperatures. In terms of standard static loop models the behaviour of the correlations could be understood if we assume that the emission at lower temperatures comes from a combination of cool loops and the footpoints of hot loops. In this case we would expect only limited correlation with hotter emission. If the emission in the intermediate temperature range, log T=5.9-6.0, comes exclusively from the footpoints of hot loops, and the emission hotter than this from the coronal parts of the loops, then again we would expect little correlation with hotter material for the intermediate range. The behaviour of the contrast on the disk at coronal temperatures is however not well understood in terms of the standard model. We would expect greater contrast in the corona than in the transition region. The fact that we see the opposite behaviour could be due to a greater filling factor in the corona, as suggested by Schrijver et al. (1999), or it could be that the assumption that all the emission comes from loops well described by the standard model is incorrect.

The existence of broad-band power-law spectra at all temperatures in topologically different active regions indicates that there is no preferred size scale for this emission. It may also indicate that turbulence plays a role in determining the structure and ultimately the heating of the corona. Hollweg (1983) suggested that kinetic energy injected over large scales by sub-photospheric convective motions might cascade down through non-linear interactions to scales where viscosity and resistivity could produce effective dissipation. In Fourier terms this translates into a broad-band isotropic spectrum with energy injected at low wavenumbers and the dissipation region at high wavenumbers. The region between, the inertial regime, is dominated by non-linear interactions, and this region is characterized by the power-law index. However, the value of this index is -5/3 for hydrodynamic turbulence (Kolmogorov, 1941) and -3/2 for the MHD case (Kraichnan 1965), considerably less negative than the -2.1 to -3 reported from NIXT, SXT and EIT observations (Gomez et al. 1993; Martens & Gomez 1992; Benz et al. 1997 and Berghmanns et al. 1998) and the -1.6 to -3.5 that we have found from CDS observations. There may be several reasons for this discrepancy. Firstly, if the coronal magnetic field is passively controlled by the sub-photospheric turbulence, then the power-law index of the coronal emission is not expected to be the Kolmogorov or Kraichnan values (Gomez et al. 1993). But even if turbulence develops in the corona itself, the intertial regime is likely to begin near the smallest observable scales and extend to sub-resolution sizes; most of the observed spectrum is outside of this range. Finally, it is not obvious how the kinetic energy density spectrum of the turbulent eddies - to which the Kolmogorov and Kraichnan indices apply - is related to the power spectrum of the resulting emission pattern.

Our results show that the steepness of the omni-directional spectra changes with temperature, becoming steeper at higher temperatures. The enhanced power at high wavenumbers for low temperatures could be consistent with the bulk of this emission originating in low-lying loops and the footpoints of hotter loops. What this, together with the results for the intensity correlations and contrast, are almost certainly telling us is that the transition region is made up of several components. It appears, when the results of this study are considered in parallel to other investigations, that there are indeed real physical differences between these different temperature plasmas which must be taken into account when modelling potential heating processes. The finer scale structure, sharper contrast and more dynamic behaviour of the cooler plasma suggests a very high degree of both spatial and temporal intermittency in the heating of these structures. The suggestion by Schrijver at al. (1999) that the apparent reduction in contrast with increasing temperature observed by TRACE is in fact due to an increase in filling factor with temperature could be consistent with the possibility that different types of energy release may be occurring. We might expect that a spatially and temporally intermittent energy release process would lead to smaller filling factors than a more homogeneous mechanism.

References

Benz, A.O., Krucker, S., Acton, L.W. and Bastian, T.S., 1997, A&A, 320, 993

Berghmanns, D., Clette, F. & Moses, D., 1998, A&A, 336, 1039

Gomez, D., Martens, P.C.H. & Golub, L., 1993, ApJ, 405, 767.

Hollweg, J.V., 1983, Solar Wind V, NASA Conf. Publ. 2280, 5, ed. M. Neugebauer.

Kolmogorov, A.N., 1941, C.R. Dokl. Acad. Sci SSSR, 30,301.

Kraichnan, R.H., 1965, Phys. Fluids, Vol.8, no. 7, 1385.

Martens, P.C.H. & Gomez, D., 1992, PASJ, 44, L187.

Schrijver, C. et al., 1999, Solar Phys., submitted.

Solar filaments - Comparing multi-wavelength observations with magnetic modelling

B. Schmieder

Observatoire de Paris, Section Meudon
92195 Meudon Cedex Principal, France

Abstract. Multi-wavelength observations of a filament/prominence obtained during campaigns with the space missions (SOHO, Yohkoh, TRACE) open a new research field. Physical conditions of filaments and their environment (i.e. temperature, dynamics, electron density) provides important constraints on theories of formation, stability or instability. The fine structures of filament are discussed in the framework of magnetic configurations: Is the prominence field a sheared arcade or a twisted flux rope? What is the magnetic structure of the footpoints of prominences called also "barbs"? Are the field lines dipped or are they vertical?
We present some new developments of 3-D models of a bipolar magnetic field and twisted flux tube which explain the fine structures in prominences as well as the feet. The new models bring valuable information on the global solar magnetic field with direct implications for dynamo theories and on the helicity of the heliosphere.

1. Introduction

Solar prominences are cool structures ($\sim 10^4$ K). They are visible in the hydrogen Hα line, visible as large and bright structures over the limb. On the disk they are dark filaments overlying the bright chromosphere. The understanding of their nature requires studies in multiwavelengths which allow to cover a large temperature range and to analyse the environment of the prominence. Since long ago these objects have been observed in Hα line. Let us mention Deslandres and Hale who built spectroheliographs by the end of the

19^{th} century and the thesis of d'Azambuja and d'Azambuja (1948) which reported the main properties of filaments. Since that time, routine programs are performed i.e. the Meudon observations every day of the full disk in 3 wavelengths (Hα, Ca II K1, Ca II K3). In Hα and Ca II K3 we see respectively filaments on the disk and prominences at the limb (Figs. 1 and 2).

Progress has been achieved recently in prominences studies, with the development of high resolution telescopes and spectrographs on the ground (in Canaries Islands: THEMIS/MSDP, VTT/MSDP, LaPalma/SVST, in Ondrejov, in Bialkow, in Big Bear) and in space. We have a great opportunity with the launch of three space missions observing the Sun (Yohkoh since 1991, SOHO since 1996, TRACE since 1998). The instruments onboard the space missions observe in EUV lines and in soft X-rays. They are useful to study the transition region between the prominence and the corona and to detect the instability process leading to filament eruption and coronal mass ejection (CME).

In the next section I will review briefly the main properties of filaments, pointing out the problem of their formation (see book of Tandberg-Hanssen 1994). Then I will focus on the presentation of the magnetic field supporting the filaments against gravity and conclude by inserting prominences in a more global context relating them to the dynamo process below the photosphere on one hand and on the other end, to the large magnetic clouds approaching the Earth after CMEs.

	Quiescent Prominence	Remarks
length	60 - 600 Mm	less for active-region filament
wide	4 - 15 Mm	
distance between feet	30 Mm	size of the supergranules
density	10^{10} - 10^{11} cm^{-3}	less in prominence-corona region (10^8 - 10^9 in cavity)
temperature	5000 - 8000 K	higher T (PCTR) observed in UV lines
magnetic field	4 - 50 G	100 G in active-region prominence
angle (axis of prom./B)	15 - 25 degrees	Hanle effect
configuration	inverse	normal for active region filament
magnetic flux	2.5 $\times 10^{19}$ Mx	for active-region filament F = 10^{20} - 10^{21} Mx
flows	vertical 0.5 - 5 km/s, horizontal 10 - 20 km/s	60 km/s in active prominences
Diagnostics	Hydrogen lines (Hα - Lyman lines), Ca II radio $\lambda < 1$ cm	NLTE radiative transfer physical parameters (Nobeyama Observatory)

Table 1: Identity card of prominences.

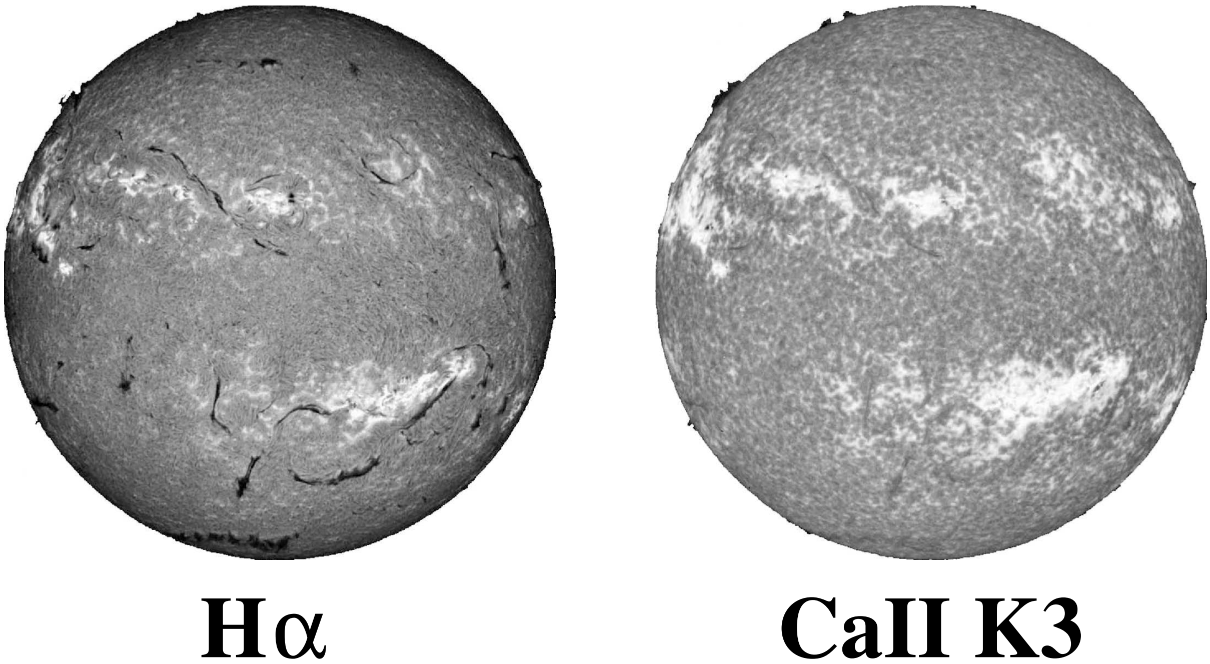

Figure 1: The chromosphere observed in the lines Hα of hydrogen and Ca K3 of ionized calcium as spectroheliograms obtained at Meudon. On the disk long dark structures are the filaments. Above the limb some dark prominences are well visible in K3. Bright areas correspond to plages. In K3 we see the regular network (Courtesy of the Observatoire de Paris).

2. Properties of filaments

Filaments have very specific characteristics in length and width; they are long (100Mm)- e.g. quiescent filament lying generally in the Quiet Sun or around the poles (polar-crown filaments) and short (10 Mm) and low lying inside active centers (Table 1). They lie over the inversion line of the photospheric longitudinal magnetic field component. The strength of the magnetic field can be weak on both sides of the inversion line: i.e. $\sim$ 100-200 G for quiescent filaments. The physical quantities of prominences are derived from the analysis of the spectral lines. Because prominences are formed by cool plasma ($\sim 10^4$K) they are mainly visible in optically thick lines (Hα, He 10830 Å) which require the resolution of the radiative transfer equations. The cool plasma absorbs the radiated light of the Sun and produces emissions at the same frequencies mainly by partial or complete radiative redistribution. At the limb we observe only the emission, on the disk we have to distinguish between the 2 processes and to take into account that the prominence is not completly optically thick. Sophisticated treatement have been performed using non LTE approach (Gouttebroze, Heinzel and Vial 1993). The SOHO/SUMER spectrograph has observed filaments and prominences in the Lyman series. Lyman lines show a central reversal in filaments due to the absorption of the radiation of the cool plasma.

The observations in coronal lines in wavelengths shorter than the cut-off of the Lyman continua of Hydrogen (< 911 Å) or He (< 550 Å), show dark areas at the locations of

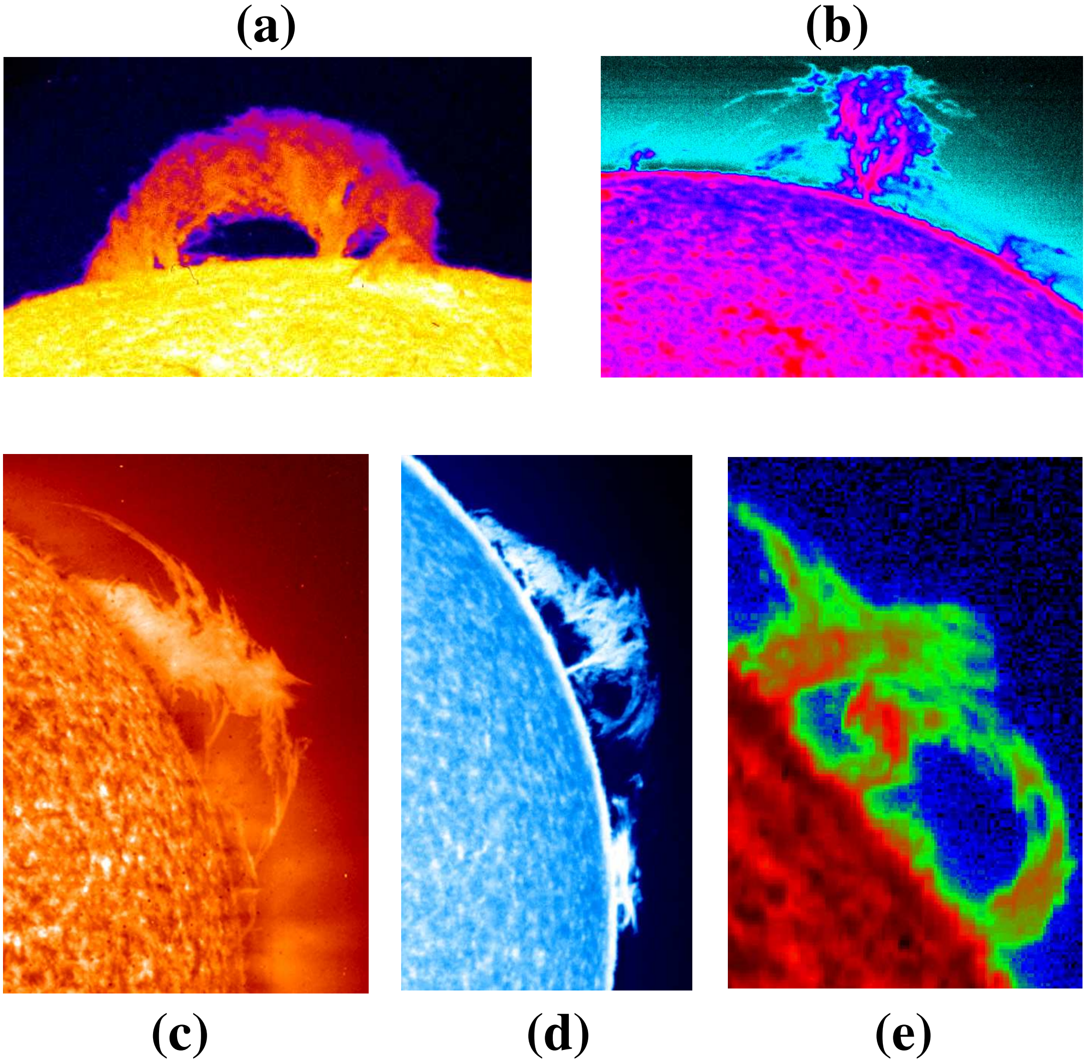

Figure 2: Observations of prominences in Hα (a), Ca II line (b) and (d) with the Meudon spectroheliograph in UV lines, (c) with EIT 304 Å and (e) with SUMER CIII line.

prominences. It is due to the absorption of this radiation (continua) by the cool plasma of the prominence. This phenomenon is well observed in coronal lines (Mg X) observed by SOHO/CDS spectrograph and by TRACE (171 Å and 195 Å) (Figure 3). Recent studies show that it is a good diagnostic to derive the hydrogen column density of the prominences (Kucera et al. 1998, Schmieder et al. 1999). The electron density is in fact difficult to estimate. Three orders of magnitude exist between the different determinations (10^9 to 10^{12} cm^{-3}). This discrepancy is due to the different methods of analysis or to the large variety of prominences or to the filling factor which is an unknown parameter.

The electron density is an important parameter because it is the clue to the interpretation of the stability of prominence. The scale height of a prominence is less than 500 km so it means that it is impossible to maintain plasma at 100 Mm high in a loop. Material will fall down immediately. This implies that the plasma pressure cannot provide the mechanism of support. So we need to consider other possible supports: dynamics, magnetic field or Alfvén waves.

The prominences observed as a whole object have a slow upflow of a few km/s and are relatively stable (Schmieder 1989, 1990). On a small scale it is nevertheless not true and the fibrils of filaments have longitudinal bidirectional flows (Fig. 4). That is difficult to undertand in a global approach (Schmieder et al. 1991, Zirker et al. 1998). So we have to consider seriously how the magnetic field supports the material (see next section). The instruments of SOHO (SUMER, EIT and CDS) are well adapted to observe the transition region betwen the filament and the corona (PCTR). EIT provides many movies of eruptive prominences in He II 304 Å (10^5 K) and shows how twisted are filaments as they erupt (Fig. 5).

In C IV and Si IV lines, the emission by the PCTR of filament is weak and difficult to be seen. Some fibrils were detected in filament channesl and were interpreted as legs of large loops overlying the prominences and heated by ohmic dissipation to 10^5 K temperature (Kucera et al. 1999). Statistical studies show that PCTR thickness is less than 100 km, which is under the spatial resolution of the instruments (Wiik et al. 1999).

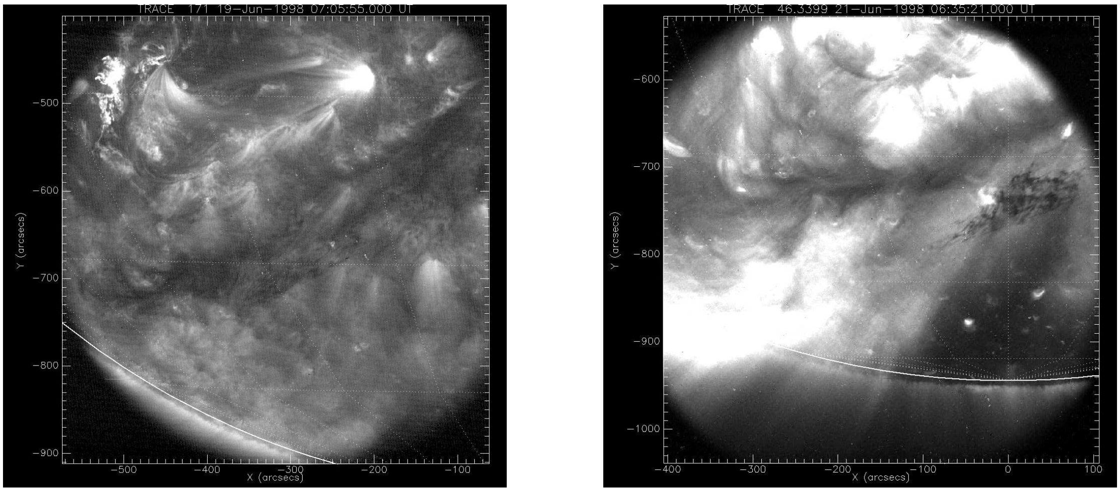

Figure 3: Polar crown filament observed with TRACE at 171 Å (left panel) on June 19 1998, (right panel) on June 21 1998. The filament is visible in the south of the filament channel because of perspective effects. The channel is dark because of lack of the coronal line emission, the filament is also dark because of the absorption of the coronal line by the cool plasma. North is up.

3. Magnetic field

3.1. Observations

3.1.1. Hanle effect

In prominences the Zeeman effect allows the measurement of the longitudinal component of the magnetic field (Kim 1990). Radio wavelengths provide information on the field

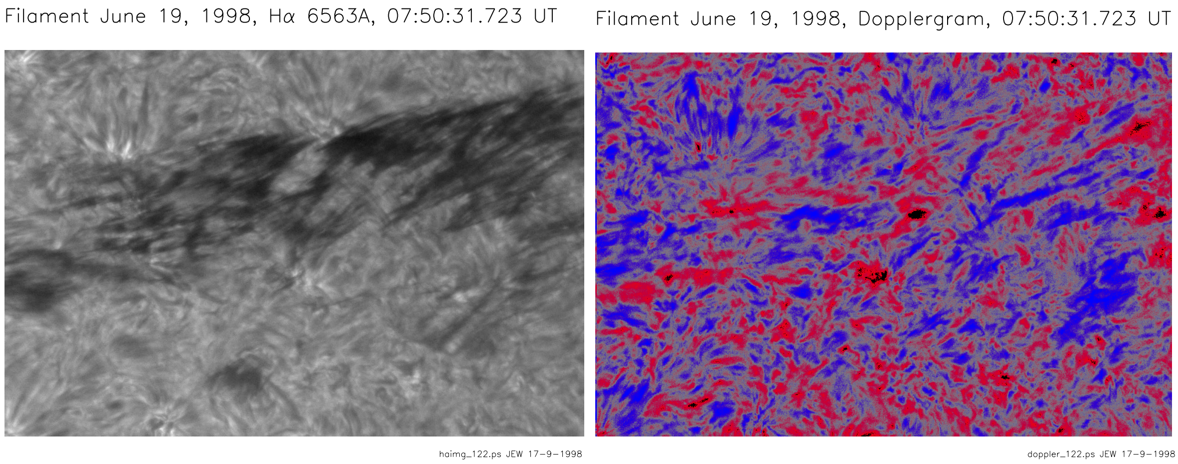

Figure 4: Polar crown filament observed in Hα on June 19 1998 by the SVST telescope in LaPalma ($100'' \times 250''$): (a) filament observed in Hα line center at 07:50:31 UT, (b) Doppler image derived from nearly simultaneous images recorded in H$\alpha \pm$ 0.25 Å. The North is more or less oriented towards the bottom of the image.

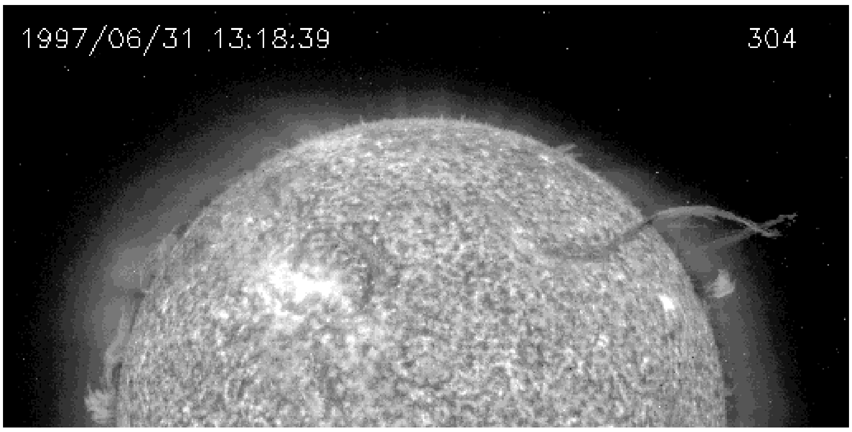

Figure 5: Eruptive twisted prominence observed by SOHO/EIT.

strength (Apushkinskii et al. 1990). The Hanle effect gives the three components of the field and the electron density from the polarization components in two spectral lines (Bommier et al. 1994). The main results of Hanle measurements are the following: the prominence field has the opposite direction to that expected from simple extrapolation of the photospheric field. It is called "Inverse type" (Leroy et al. 1984), contrary to the "Normal type" where the fields in prominences and photosphere have the same direction. 90% of prominences have the inverse type (Bommier et al. 1998). In that case the orthogonal component (B_{per}) is opposite to the field of a simple arcade and also the field component parallel to the prominence ($B_{//}$) is opposite to that of an arcade sheared by the differential rotation. The magnetic field in prominences is nearly horizontal field, homogeneous on the scale of a few arc seconds, and increasing with height (Leroy et al. 1983). The prominence fine structures are inclined by 20 to 30 degree towards the prominence main axis.

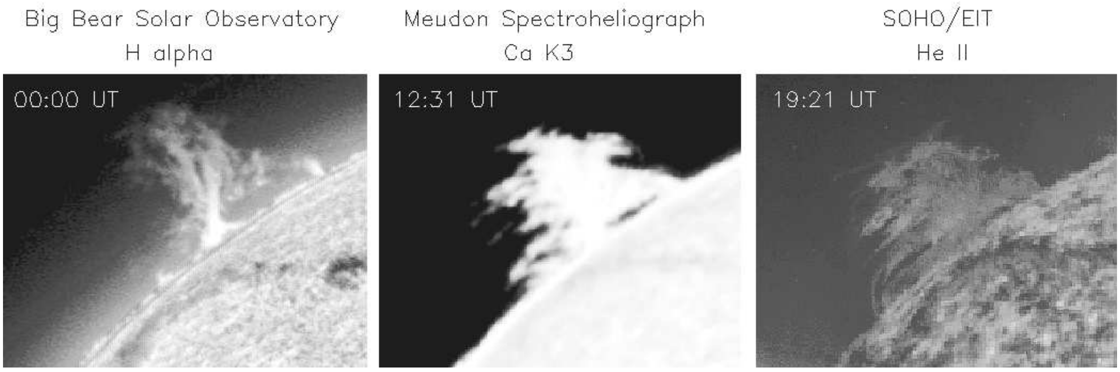

Figure 6: Example of a prominence observed in multi-wavelengths. It appears vertical in Hα and horizontal in He line.

3.1.2. Presence of magnetic dip

Let us assume that the cold material is supported by the magnetic field. If enough mass can be brought into the top of sheared magnetic arcade in less than one hour, the gravity force can bend the top of the field lines and form a dip (Dere et al. 1990, Fiedler and Hood 1993). The observations of dips are not evident but it could be suggested in some fine observations (Rompolt 1990). A long debate on the structures in prominences is still not clarified. Multi-wavelength observations show that prominence threads can appear vertical in Hα and horizontal in UV lines (Fig. 6). This has been explained as being due to the existence of long horiontal field lines, a part of them being heated to EUV temperatures while in the middle small dips are formed with cool plasma. Due to the perspective effect all the small dips in the different field lines could give the impression of the existence of a vertical structure (Aulanier et al. 1999, Kucera et al. 1999).

3.2. Magnetic configurations supporting prominences

Since the well known 2D model of Kippenhahn and Schlüter (1957), several models have been proposed in 2 1/2 D and then in 3D. Two types of models are considered: arcade-like configurations and twisted flux tubes.

3.2.1. Model in 3D with overlying arcade

Arcade models in 2 1/2 D cannot have a dip at the top of the field lines even when the magnetic shear increases (Amari et al. 1991). In 3D it can occur. The overlying arcade locally compresses the central part of an underlying sheared arcade (Antiochos et al. 1994). The latter model gives an inverse polarity prominence with a magnetic field nearly aligned with the photospheric inversion line. But the direction of the axial field will be wrong.

3.2.2. Quadrupolar configurations

These configurations naturally have a dip. Malherbe and Priest (1983) and later Démoulin and Priest (1993), Uchida (1998) developed such models. The presence of a corridor free of significant field is needed to have a prominence extension reaching the chromosphere and converging motions to provide mass. These models are perfectly adapted for active region filaments (Tang 1987) or filaments between two active regions (MacKay et al. 1998). The presence of "dual arcades" observed by Yohkoh/SXT might be a signature of magnetic reconnection in quadrupolar configurations (Uchida 1998).

3.2.3. Models in 3D with twisted flux tubes and "barbs"

This class of models provides the needed dipped magnetic field and seems to be well supported by recent observations. The twisted configuration can be obtained by photospheric twisting motions (Priest et al. 1989), by converging motions in a sheared arcade with magnetic reconnection at the inversion line (van Ballegooijen and Martens 1989), by resistive instability in a sheared arcade or by relaxation and accumulation of helicity (Démoulin and Priest 1989, Rust and Kumar 1994) or by emergence from the convective zone (Low 1994, 1996). Prominence feet appear as a direct consequence of the parasitic polarities present in the filament channel. Priest et al. (1996) used the emergence of small loops to create feet or "barbs". The feet would be due to the reconnection occurring between the emerging dipole and the main filament field. Aulanier and Démoulin (1998 a,b) showed that the feet appear naturally above secondary photospheric magnetic inversion lines produced by the parasitic polarities which create local quadrupolar configuration able to support the plasma in the feet.

3.2.4. 3D model of prominence with bald patch

A recent model has been developed by Aulanier et al. (1998c, 1999). These authors show the importance of field topology. They consider a bipolar configuration imposing a twisted flux tube by increasing the shear in the region. They use the equations of linear magnetohydrostatics (lmhs) for the extrapolation (Low 1992). Pressure and gravity are taken into account. They use directly the observed longitudinal fields, taken from magnetograms obtained by SOHO/MDI. They compare their field lines with the filament observations obtained on the ground (VTT, Tenerife) and in space (SUMER). They examine the dips of the field lines where material can be supported. They draw only the portion of the field lines dipped enough (2Mm). They find good agreement between the shape and location of the dipped field lines and the shape of the filament body (Fig. 7). MacKay et al. (1999) confirmed this model with a similar approach but using a relatively strong magnetic field bipole to represent the background which is not realistic for quiescent prominences.

4. Magnetic helicity and filaments

The observations show specific relationships of chirality among filaments, coronal arcades, active regions, coronal mass ejections and magnetic clouds.

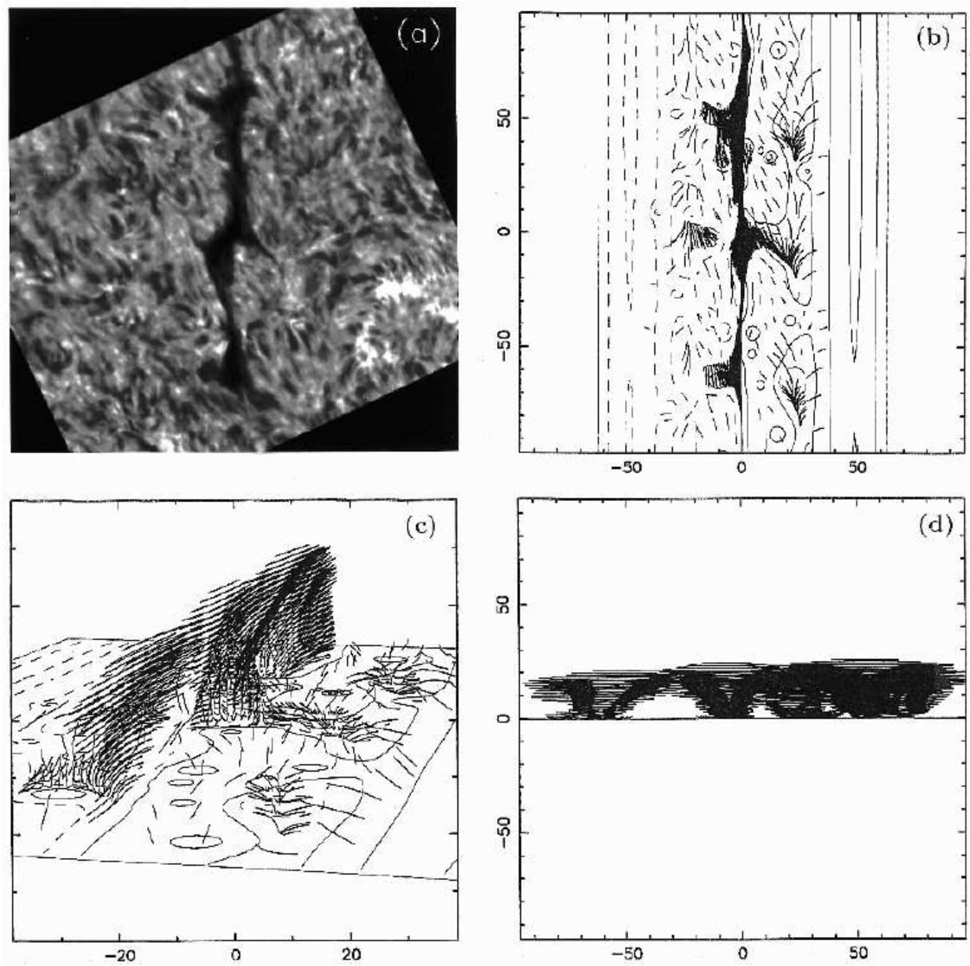

Figure 7: Model of bald patch filament in 3D: (a) Observations of a Hα filament with the MSDP spectrograph on the VTT at Tenerife, (b) MDI magnetogram and extrapolated magnetic field lines drawn only in the dips, (c) 3D view, (d) side view (Aulanier et al, 1998c).

4.1. Chirality of filament and fibrils

Filaments are always found above inversion lines of the photospheric magnetic field in regions, called corridors or filament channels, which are nearly free of chromospheric fibrils. They are also characterized on either side by the presence of Hα fibrils nearly aligned with the inversion line indicating a high magnetic shear (Foukal 1971, Rompolt 1990). The corridor is nearly free of vertical magnetic field flux except small parasitic polarities (Raadu et al. 1988, Martin 1990). At the locations of these small polarities we observed *the plagettes* from which fibrils stream parallel to the filament. Two morphological forms of filament channels and filaments have been identified. They are called *dextral and sinistral.* An observer standing on the positive polarity side of a dextral/sinistral filament would see the lateral feet pointing to the right/left along the filament channel.

For prominences these names correspond to right-bearing/left-bearing prominences if the prominence feet bear off to the right/left of the main axis of the prominence. All dextral filaments are right-bearing. Most quiescent filaments in the northern/southern hemisphere are *dextral/sinistral* at mid- and high latitudes, regardless of cycle (Martin et al. 1994, Martin and McAllister 1998). Observations show that there is a good correlation between the direction of the magnetic field along the filament as inferred from the plagettes and as inferred from the lateral prominence feet.

4.2. Coronal arcades

The X-ray observations made by Yohkoh/SXT have told much about the coronal arcades overlying filament channels (McAllister et al. 1998). The skew of the coronal arcades changes according to the hemisphere. Skew was defined as the acute angle between the loops and the polarity inversion or filament axis. If the arcade loops cross over the filament in the sense of threads of a left-hand/right-hand screw they defined the loops as left-skewed/right-skewed. Left skewed arcades overlie dextral filaments (Martin and McAllister et al. 1995).

4.3. Shear angle and sigmoids

Conspicuous fibrils are observed near sunspots penumbras. Richardson (1941), recognizing a similarity between fibril pattern and the pattern of iron fillings around bar magnets, made an extensive study of the orientation of the superpenumbra fibrils and found that the majority is clockwise for sunspots in the southern hemisphere. This was confirmed later by Rust and Martin (1994). On the other hand Seehafer (1990) estimated the electric current helicity in 16 active regions and concluded that the electric current helicity is predominantly positive/negative in the southern/northern hemisphere. This result was confirmed also from a comparison between Mees vector magnetograms and current-free configurations (Pevtsov et al. 1995).

Very large scale X-ray structures have been noticed to exhibit a slender S or backward-S shape as a function of hemisphere (Rust and Kumar 1994, Moore et al. 1997). Reverse S-shaped structures predominate in the northern hemisphere as do S-shaped structures in the southern hemisphere. In active regions such shape is called sigmoid, they are frequently observed in X-ray around the flare time showing strong shear (Rust and Kumar 1996, Canfield et al. 1999).

4.4. Twisted configurations

Filaments destabilize for different reasons. Emerging flux in filament channels can lead to disruption of the filament (Raadu et al. 1988). On the other hand they can be destabilized by some instabilities in the corona (Antiochos et al., 1999). Eruptive prominences appear commonly twisted (Fig. 5). Modeling a filament as an initially untwisted axial magnetic field aligned with the inversion field, Martin and McAllister (1998) claim that dextral filaments develop right-helical twist on the sun and that the corresponding interplanetary clouds have the helicity opposite to the CMEs after they have been detached from the Sun by reconnection. This solution is controversial and another solution of all these laws of chirality is proposed based on the idea that the filament lies in the lower portion of a large-scale helical magnetic field which supports the filament against gravity (Rust and Kumar 1994, Aulanier et al. 1998 c, 1999, MacKay et al. 1999).

4.5. Helical structure of magnetic cloud

Interplanetary clouds are the ejected parts of coronal mass ejections as first concluded by Marubashi (1986). Many such plasma clouds have helical structure detected by magnetometers on board spacecrafts (Burlaga 1991, Bothmer et al. 1996, Webb 1998). Gosling (1990) proposed that helical magnetic fields in interplanetary clouds originate from magnetic reconnection in ascending coronal arcades. Based on the same scenario, Martin and McAllister (1998) anticipate that left-skewed coronal arcades become left-helical CMEs and are detectable later as left-helical interplanetary clouds. Rust and Kumar (1994) found that the majority of interplanetary clouds with left/right-helical structures come from the northern/southern hemispheres, but they proposed that the helicity of the clouds reflects the helicity of the filaments before they erupt which in turn reflects the helicity of the solar dynamo generated fields.

5. Discussion on helicity

A natural way to explain how both magnetic field components, parallel and normal to the prominence, are inverse is to use a quadrupolar field sheared by the differential rotation (Priest et al. 1996). However, this gives a magnetic helicity dominance in each hemisphere opposite to observations. Van Ballegooijen et al. (1998) demonstrated that the differential rotation does not work correctly for the helicity conservation. Studying a switchback inversion line, they showed that the model taking into account the differential rotation predicts an opposite chirality on the 2 arms of the switchback which is contrary to the observations. Berger (1998) reviewed different statements that are well established to sketch a solution. Helicity is conserved in ideal MHD, and it is probably well conserved on the sun, so any positive helicity generated by plasma motions, for example, must be offset by negative helicity generation. Berger proposed to explain the sign of the helicity, namely, North hemisphere negative, South Hemisphere positive by taking into account the transfer of the helicity either into or from the solar wind or across the equator, beneath the surface. His solution to helicity in filaments is based on the emergence of twisted flux tubes. The same approach was advocated by Rust and Kumar (1994). Reconnection below the solar surface could create twisted flux tubes which emerge due to buoyancy. By transfer and redistribution of the helicity and by using faster rotation at the equator one can reproduce at least the observed global helicity pattern. Van Ballegooijen (1999) presented an MHD model which takes into account the solar differential rotation, the photospheric diffusion and flux cancellation in a 3D active region. After reconnection he formed a left/right helical flux rope in the North/South hemisphere from an untwisted emerging bipole.

Démoulin (1998) explained that the right sign of helicity could be obtained with Coriolis forces acting on diverging supergranular flows (Priest et al. 1989). This process is very efficient and can accumulate helicity in twisted tubes but since localized motions give neutralized currents, it is difficult to reproduce the dominance of one polarity as observed in each hemisphere.

If a local dynamo cannot give a good explanation, then global dynamo models should be investigated for their possible helicity-producing qualities (Seehafer 1998).

6. Conclusion

The large amount of data concerning helical features, from filaments to interplanetary clouds, have shown a great organizing principle of nature as originally pointed out by Rust (1994). We need models that can fit into a unified theory. We have shown the importance of twisted flux tube emergence, the presence of parasitic polarities in the inversion line corridor, the aligned fibrils in the filament corridor and all the chirality laws. Many questions are unsolved and we need further observations with multi-wavelength instruments to test the existing different proposed approachs.

References

Amari T., Démoulin P., Browning P., Hood A.W., Priest E.R. 1991, A&A, 241, 604

Antiochos S.K., Dahlburg R.B., Klimchuck J.A. 1994, ApJ, 420, L41

Antiochos S.K., DeVore C.R., Klimchuck J.A., 1999, ApJ, 510, 495

Anzer U. 1972, Solar Phys., 24, 324

Apushkinskii G.P., Nesterov N.S., Topchilo N.A., Tsyganov A.N. 1990, SvA, 34(5), 530

Aulanier G., Démoulin P., 1998a, Publications of the ASP, 150, 186

Aulanier G., Démoulin P., 1998b, A&A, 329, 1125

Aulanier G., Démoulin P., van Driel L., Mein P, deForest C. 1998c, A&A, 335, 309

Aulanier G., Démoulin P., Mein N., van Driel-Gesztelyi L., Mein P., Schmieder B. 1999, A&A, 342, 867

Berger M. 1998, Publications of the ASP, 150,102

Bommier V., Leroy J.L. 1998, Publications of the ASP, 150, 434

Bommier V., Landi Degl'Innocenti E., Leroy J.L., Sahal-Bréchot S., 1994, Solar Phys., 154, 231

Bothmer V., Desai M.I., Marsden R.G. et al. 1996, A&A, 316, 493

Burlaga L.F. 1991, in Physics of the Inner Heliosphere II, eds. R.Schwenn, E.Marsch, Springer Verlag, New York, 1

Canfield R., Hudson H., McKenzie D., 1999, Geophysical Research Letters, 26, 627

d'Azambuja L., d'Azambuja M. 1948, Annales de l'Observatoire de Paris, 6,7

Démoulin, P. 1998, Publications of the ASP, 150, 78

Démoulin P., Priest E.R. 1989, A&A, 214, 360

Démoulin P., Priest E.R. 1993, Solar Phys., 144, 283

Dere K.P., Schmieder B., Alissandrakis C. 1990, A&A, 233, 207

Fiedler R.A.S., Hood A.W. 1993, Solar Phys., 146, 297

Foukal P. 1971, Solar Phys., 19, 59

Gouttebroze P. Heinzel P., Vial J.C., 1993, Astron. and Astrophys. Suppl. Ser. 99, 513

Gosling J.T. 1990, in Physics of Magnetic Flux Ropes (eds) C.T.Russell, E.R. Priest, L.C.Lee, Geophys. Mono. Ser. 58, 343

Kim I.S. 1990, IAU Colloq. 117, Springer-Verlag, 49

Kippenhahn R., Schlüter A. 1957, Zs. Ap. 43, 36

Kucera T.A., Andretta V., Poland A.I. 1998, Solar Phys., 183, 107

Kucera T.A., Aulanier G., Schmieder B., Mein N. and J.C. Vial 1999, Solar Phys., 186, 259

Leroy J.L., Bommier V., Sahal-Bréchot S. 1983, Solar Phys., 83, 135

Leroy J.L., Bommier V., Sahal-Bréchot S. 1984, A&A, 131, 33

Low B.C. 1992, ApJ, 399, 300

Low B.C. 1994, Plasma Phys., 1, 1684

Low B.C. 1996, Solar Phys., 167, 217

MacKay D.H., Gaizauskas V., Ricckard G.J., Priest, E.R. 1998, ApJ, 486, 534

MacKay D.H., Longbottom A.W., Priest E.R., 1999, Solar Phys. 185, 87

McAllister A.H., Hundhausen A.J., MacKay D.H., Priest, E.R. 1998, Publications of the ASP, 150, 43

Malherbe J.M., Priest E.R. 1983, A&A, 123, 80

Marubashi K. 1997 in Coronal Mass ejections Geophys. Mono. Ser., 99, 147

Martin S.F. 1990, IAU Colloq. 117, Springer-Verlag, 1

Martin S.F., Bilimoria R., Tracadas P.W. 1994, in R. Rutten and C. Schrijvers (eds.), Solar Surface Magnetism, Kluwer Ac. Pub., 303

Martin S.F., Mc Allister A.H. 1995, in Proc. Colloq. IAU 153

Martin S.F., McAllister A.H. 1998, Publications of the ASP, 150, 419

Moore R.L., Schmieder B., Hathaway D.H., Tarbell T.D. 1997, Solar Phys., 176, 249

Pevtsov A.A., Canfield R.C., Metcalf T.R. 1995, ApJ, 440, L109

Priest E.R., Hood A.W., Anzer U. 1989, ApJ, 344, 1010

Priest E.R., Van Ballegooijen A.A., MacKay D.H. 1996, ApJ, 460, 530

Raadu M.A., Schmieder B., Mein N., Gesztelyi L. 1988, A&A, 197, 289

Richardson R.S. 1941, ApJ, 41, 24

Rompolt B. 1990, Hvar Obs. Bull. Vol. 14, 1, 37

Rust D.M. 1994, Geophys. Res. Lett. 21, 241

Rust D.M., Kumar A. 1994, Solar Phys., 155, 69

Rust D.M., Kumar A. 1996, ApJ, 464, L199

Rust D.M., Martin S.F. 1994, in Solar Active Region Evolution, Publications of the ASP 68, 337

Schmieder B. 1989, in E.R. Priest (ed.), *Dynamics and Structure of Quiescent Solar Prominences*, Kluwer Academic Publishers, Dordrecht, Holland, 15

Schmieder B. 1990, IAU Colloq. 117, Springer-Verlag, 85

Schmieder B., Kucera T., Heinzel P., Kotrć P. 1999, SPM meeting in Florence, ESA proceedings, SP-448, in press

Schmieder B., Raadu M.A., Wiik J.E. 1991, A&A, 252, 353

Seehafer N. 1990, Solar Phys., 125, 219

Seehafer N. 1998, Publications of the ASP, 150, 407

Tandberg-Hanssen E. 1994, the Nature of Solar Prominences, Kluwer Academic Publishers

Tang F. 1987, Solar Phys., 107, 233

Uchida Y. 1998, Publications of the ASP, 150, 163

van Ballegooijen A.A., Martens P.C.H. 1989, ApJ, 343, 971

van Ballegooijen A.A., Martens P.C.H. 1990, ApJ, 361, 283

van Ballegooijen A.A., Cartledge N.P., Priest E.R. 1998, Public. of the ASP, 150, 265

van Ballegooijen A.A., 1999, in Magnetic Helicity in Space and Laboratory Plasma, eds. Brown M.R., Canfield R.C., Pevtsov A.A. Geophys. Monogr. Ser., AGU Washington D.C., 213

Webb D. 1998, Publications of the ASP, 150, 463

Wiik J.E., Dammasch I., Schmieder B., Wilhelm K 1999, Solar Phys., 187, 405

Zirker J.B., Engvold O., Martin S.F., 1998, Nature, Vol 396, 440

Discussion

K.D. Leka: Two notes: The preference for active region helicity as a function of hemisphere is a weak relation at best, and it is not yet clear, given uncertainties in measurements, how well the relation really holds (see Leka, Solar Phys. 1999, 188, 3 and 21). Second comment: the hemispheric preference for filament handedness is for high latitude filaments only. Martin et al. found little or no relation for active region filaments. This, of course relates to comment (1) above.

B. Schmieder: On small scale it is difficult to derive only one value of shear for aportion of an active region but on a global point of view and integrated in time (several rotations) it seems that an active region conserves a specific helicity. Seehafer and more recently L.van Driel demonstrated this statement.

S. Antiochos: The differential rotation will inject helicity into the corona. Is this not enough to explain the observed helicity?

B. Schmieder: It could be a good idea to think about the differential rotation, but it appears that it leads to a magnetic helicity dominance in each hemisphere opposite to the observations.

Zs. Kővári: I wonder about the average lifetime of these prominences. Does the lifetime change with the size, are these properties correlated?

B. Schmieder: The lifetime of a prominence can reach few rotations (until 7 months). We distinguish two class of prominences in and outside active regions (see Table 1).

Theory of solar prominences

S.K. Antiochos

Code 7675, E. O. Hulburt Center for Space Research,
Naval Research Lab, Washington, DC, 20375-5352, USA

Abstract. We discuss the physical mechanisms for the formation, the gravitational support, and the eruption of solar prominences and filaments. We show that the formation of cool mass in the coronal is due to the thermal non-equilibrium of coronal loops that are heated preferentially near their footpoints. The gravitational support can be understood as a direct consequence of the differential shearing of a three-dimensional magnetic field. Finally, the eruption can be explained by the "breakout" model, in which magnetic reconnection leads to the explosive expansion of the sheared prominence field. We present results from numerical simulations which confirm each of these three fundamental mechanisms. Based on this work, we conclude that we are now approaching a true understanding of the basic physics of solar prominences.

Keywords: solar prominences, filament eruptions, magnetic reconnection

1. Introduction

Solar prominences and filaments are beautiful phenomena both in their appearance and in their physics (e.g., Tandberg-Hanssen 1995). They are commonly observed in Hα as large masses ($\sim 10^{16}$ g) of dense ($> 10^{11}$ cm^{-3}) chromospheric plasma floating high up in the tenuous ($\sim 10^{9}$ cm^{-3}) million-degree corona. Although most prominences have lifetimes of order days, some especially quiescent structures can last for months. Surprisingly, most prominences disappear by "falling up" as a filament eruption rather than by falling down onto the chromosphere. Large coronal mass ejections and two-ribbon flares are usually accompanied by prominence/filament eruption, consequently prominences play a key role in space weather. We conclude that understanding the fundamental physics of solar prominences is crucial not only for advancing our comprehension of solar activity, but also for understanding the Sun-Earth connection.

There are three obvious basic questions that must be addressed if we are to understand prominences/filaments:

1. How is the dense prominence mass supported against gravity?

2. Why does cool prominence mass form in the hot corona?

3. What causes prominences to erupt into interplanetary space?

We show below that the answer to each of these three questions lies in spatial inhomogeneity — of photospheric motions, of coronal heating, and of magnetic flux.

2. Gravitational support

Since the typical lifetime of prominence material is many orders of magnitude larger than the gravitational free-fall time, it is generally believed that the material must somehow be supported by the magnetic field (e.g., Kippenhahn & Schluter 1957; Kuperus & Raduu 1974). But in order for a cool condensation to sit stably on some field line, the field line must have a concave up geometry in the corona. This is, of course, completely opposite from what would be expected for a potential field due to a bipolar flux distribution at the photosphere. It is possible to obtain concave up field lines for quadrupolar flux distributions, but prominences are generally associated with bipolar regions. They overlie a single photospheric neutral line.

These considerations have led many authors to consider fairly complex models for the prominence magnetic field, such as models which involve twisted flux ropes embedded in some overlying bipolar arcade. The flux ropes are presumed to somehow form or emerge from below into the corona. But, prominences are very common and, hence, their magnetic structure must be straightforward to obtain. Furthermore, the twisted field indicative of a flux rope has never been observed, to our knowledge, except during eruption, even by the exquisite observations by TRACE. On the other hand, shear is clearly observed in both active region and quiescent prominences (e.g., Martin 1990; Schmieder et al 1996), and is strikingly visible in the TRACE images (Title, *private communication*).

We have shown how the concave up field line geometry necessary for prominence support can be simply explained as a natural consequence of spatially localized photospheric shear in 3D (Antiochos, Dahlburg & Klimchuk 1994; DeVore & Antiochos 2000). Figure 1, which is obtained from one of our 3D force-free field simulations, presents the essential features of our model. We start with a current-free dipole field and apply a shear flow at the photosphere that is concentrated near the neutral line of the dipole. The shear flow is parallel to and changes sign across the neutral line, and is large only near the neutral line. Note that this form for the magnetic shear is an observational fact (e.g., Gary et al 1987; Schmieder et al 1996), but its actual source is not important for our model. We use footpoint motions only because they are convenient to implement numerically. The shear could as well be created below the photosphere by convective motions, or the shear could be due to reconnection. The gray bottom grid in Figure 1 corresponds to the photosphere, and the color contours on this grid correspond to magnitude of the normal component of the field at the photosphere. The red – yellow contours on the near side of the Figure correspond to positive polarity, and the blue – green on the far side correspond to negative polarity. The form of the photospheric shear can be seen from these contours. The contours on opposite sides of and near the neutral line are stretched out in opposite directions.

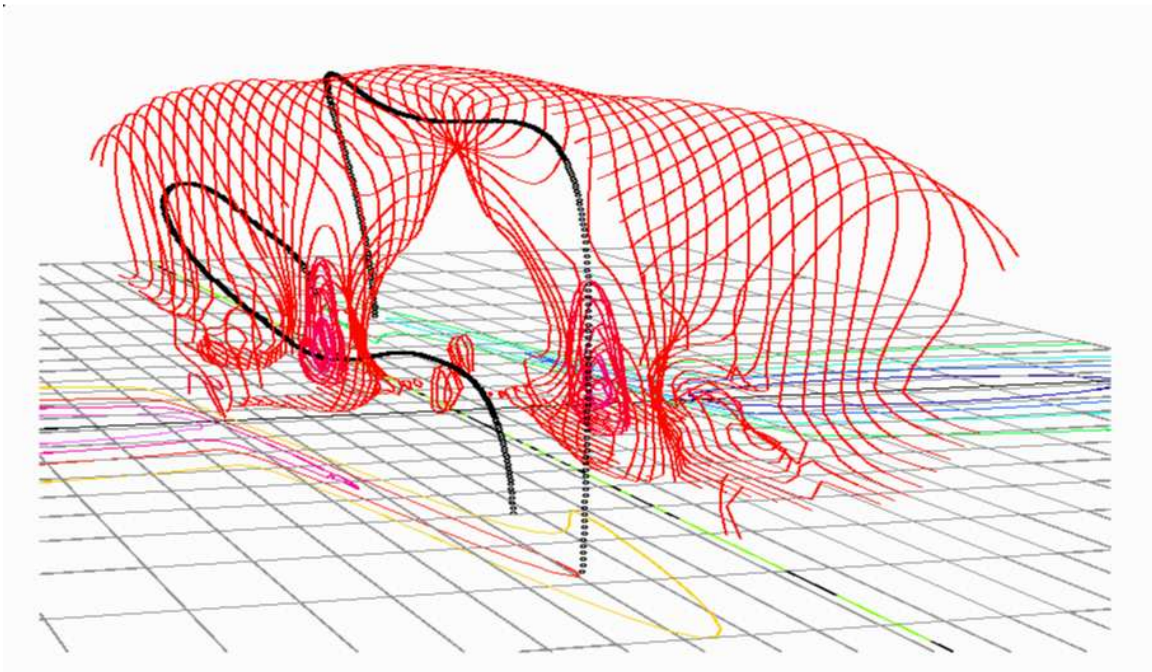

Figure 1: 3D sheared magnetic field model of a solar prominence.

Also shown in the Figure are two field lines whose footpoints lie in the strong shear region — thick black lines. Note that the lines are concave up in their midsections and, therefore, can support cool dense material in the corona. The origin of these "dips" in the field lines is due to the effect of the overlying unsheared field lines, which act to constrain the expansion of the sheared lines. The constrainment is strongest near the center of the system, where the photospheric flux is strongest, resulting in a dip near the center of the sheared lines. In other words, the unsheared flux pushes down harder on the sheared field lines near their middle, distorting them into a concave up shape.

The concave up regions of the field are shown by the mass of red contours. They correspond roughly to the shape of the prominence that this model predicts. Note that this shape has legs and an arch, very similar to what is observed for quiescent prominences. Furthermore, the model reproduces the inverse polarity that is observed in most prominences and also the characteristic "sigmoidal" shape for the field. Figure 2 shows the same force-free field as in Figure 1, but now the viewpoint is from above and we plot contours of inverse polarity. It is evident that the field lines have a sigmoidal shape and that the prominence is inverse polarity over the bulk of its volume. Another interesting agreement with observations (Martin & McAllister 1997) is that if we consider the neutral line to correspond to the main body of this prominence, we see from Figure 2 that the legs are "left-bearing", and from the form of the shear on the photosphere, the prominence is sinistral.

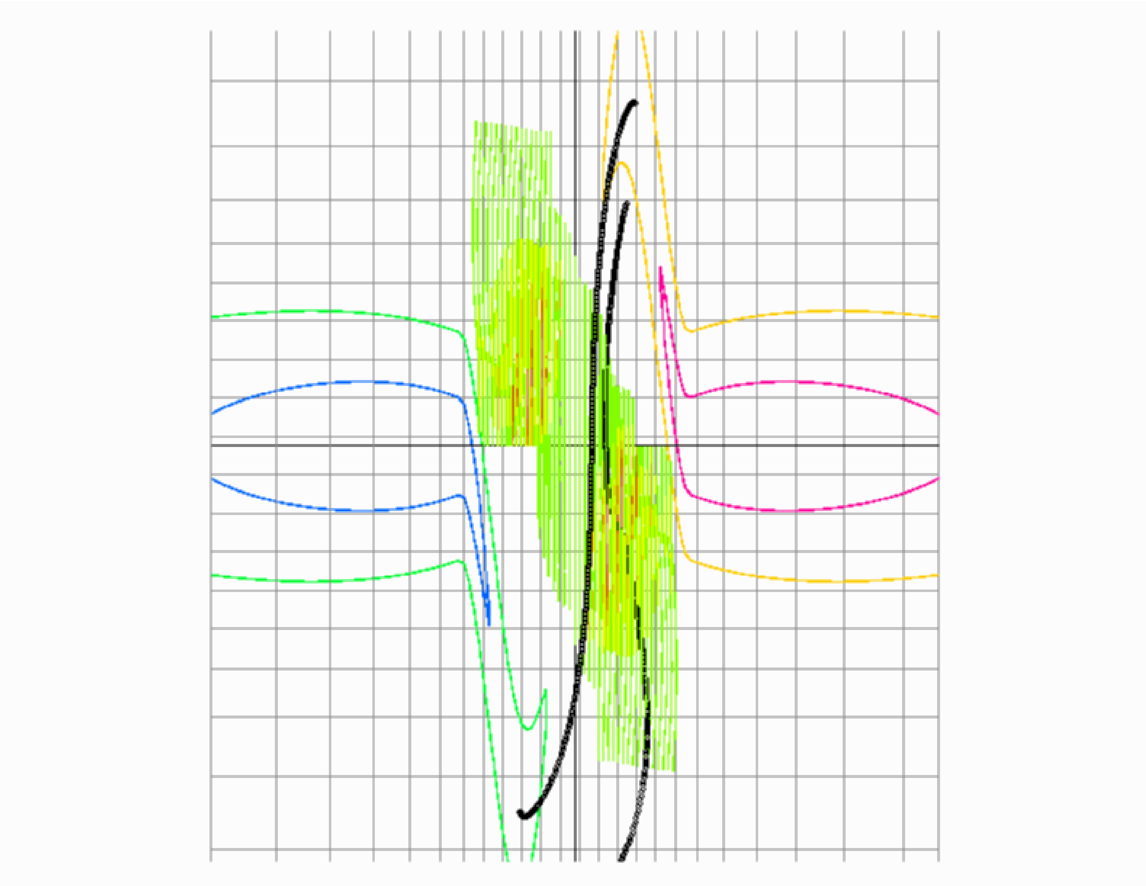

Figure 2: The prominence model of Figure 1 viewed from above.

In summary, this simple model appears to explain the origin of concave up field lines and all the major observed global features of prominence. All that the model requires is neutral line shear — twisted flux ropes need not apply! Of course, one could elaborate on our 3D shear model by adding small parasitic polarity regions (e.g. Aulanier & Demoulin 1998) or by including the effects of reconnection (DeVore & Antiochos 2000), but we now have the basic answer to our first question concerning gravitational support: Shear localized near the neutral line produces concave up field lines in 3D.

3. Condensation formation

In the previous section we considered the support of prominence condensations and argued that a sheared 3D field is likely to have field lines with dips in which the condensations can lie stably. The question remains, however, as to why condensations should form on such field lines. There is no obvious reason to expect a condensation from the usual models for coronal heating, even if the flux tube has a dip. For typical coronal temperatures ($T > 10^6$

K), the gravitational scale height ($> 5 \times 10^9$ cm) is much larger than the expected depth of a field line dip. Thus, as far as hot coronal plasma is concerned, gravity is negligible and the presence of a dip would have only a minor perturbation on the plasma structure.

It is clear, however, that prominence condensations are far from negligible. In fact, assuming a condensation size of $\sim 10^8$ cm and a density for the cool material $> 10^{11}$ cm^{-3}, we find that the mass of an individual condensation can be large compared to the hot coronal mass in the magnetic flux tube that the condensation occupies. Consequently, the condensations cannot be due to a simple thermal instability (e.g., Antiochos et al. 1985; Klimchuk, Antiochos & Mariska 1987) and cooling of coronal material, but must involve the transfer of chromospheric plasma into the corona.

Numerous models have been proposed for the formation of prominence condensations (e.g., Pikel'ner 1971; Engvold & Jensen 1977; Priest & Smith 1979; Ribes & Unno 1980; An, Bao, & Wu 1986; Poland & Mariska 1986; Mok et al., 1990), many involving the initiation of a condensation *via* an abrupt decrease in the coronal heating rate. Although this is a straightforward and attractive idea, it suffers a major drawback in that a large decrease in the heating inevitably results in a large decrease in the coronal mass. When the heating is decreased, loop material simply drains back onto the chromosphere (Poland & Mariska 1986), which is exactly the opposite of what is needed for a massive condensation in the corona.

The problem with invoking a heating decrease can also be seen by examining the usual scaling laws for quasi-static coronal loops (e.g., Rosner, Tucker & Vaiana 1978; Craig, McClymont & Underwood 1978; Vesecky, Antiochos & Underwood 1979). One finds that the coronal density, $N \propto E^{4/3}$ for a heating rate E that is constant per unit mass. Consequently, loops with decreased heating are expected to end up with low masses, rather than the large mass needed for prominence condensations.

We have proposed a novel solution to the problem of obtaining a massive condensation in a dipped loop (Antiochos & Klimchuk 1991). The key idea is that the heating has a strong spatial dependence; in particular, it is concentrated near the chromospheric footpoints of the loop, far from the dip. The effect of the localized heating is to drive a flow from both chromospheric footpoints into the dipped portion of the loop. This is most easily seen for the case of a loop that is symmetric about its midpoint. Due to the symmetry and to the presence of the dip, each loop half is physically similar to a complete, but asymmetric coronal loop that has a heating rate strongly localized near only one footpoint. It is well known that the only equilibrium solution for an asymmetric loop model with a localized heating near one base point is a steady-state flow from the heated footpoint towards the other one (Boris & Mariska 1982; Mariska & Boris 1983). Due to this flow the density and, therefore, the radiative losses in the dipped portion of the loop continue to increase until a thermal loss-of-equilibrium occurs and a large mass cools catastrophically to chromospheric temperatures.

We have verified our thermal non-equilibrium model for prominence condensation formation by a number of detailed numerical simulations (Antiochos & Klimchuk 1991; Dahlburg et al 1998; Antiochos et al 1999; Antiochos, MacNeice & Spicer 2000). Figure 3 shows the results of our most recent simulation. We considered a geometrically-symmetric dipped flux tube of total length 220,000 km, that initially had a spatially uniform heating

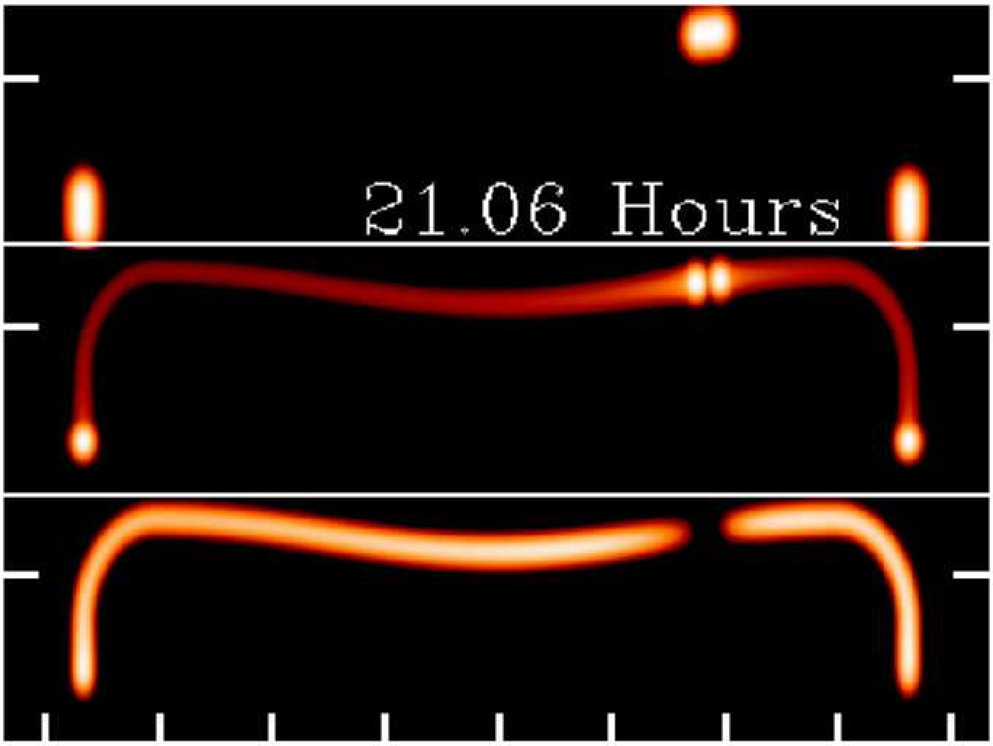

Figure 3: The Mg X (bottom panel), O V (middle panel) and H_α emission predicted by our prominence condensation model.

rate and was at coronal temperatures ($T \sim 10^6$ K) everywhere except at the footpoints. Then we applied a spatially localized heating that was maximum at the chromospheric footpoints and had a scale height of 10,000 km. In order to break any artificial symmetry, the localized heating at the right leg was taken to be 75% of that at the left. After 21 hours, the loop emission in Mg X, O V, and H_α is shown in Figure 3. It is evident that a prominence condensation, bright in H_α has formed. The condensation is bounded on each side by a transition region, visible in O V emission. Also, the condensation appears as a gap in the million degree Mg X radiation.

An interesting result is that the condensation does not sit stably in the concave up portion of the loop. Instead it moves toward the right apex with an average velocity of order 5 km/s and falls down onto the right chromosphere, (Antiochos, MacNeice & Spicer 2000). After a period of another 20 hours, another condensation forms to repeat the cycle again. Consequently, our model can account not only for the formation of condensation, but also for their recently measured dynamics (Zirker, Engvold & Martin 1998; Martin 1998). We conclude that we now have the answer to our second question concerning the origin of the mass: Prominence condensations form as a result of thermal non-equilibrium driven by a coronal heating that is spatially localized near the chromosphere.

4. Prominence eruption

Since the configuration of Figures 1 and 2 appears to be the correct magnetic structure of a prominence/filament, it is tempting to hypothesize that this configuration also leads to eruption, so that neutral line shear answers both our questions 1 and 3. In fact, the "tether cutting" model (e.g., Sturrock 1989; Moore & Roumeliotis 1992) proposes that continued shearing of this configuration will produce magnetic reconnection *below* the sheared field, thereby destroying the force balance between the sheared and overlying unsheared field and leading to an explosive eruption. Our numerical simulations of stressed bipolar fields, however, show no evidence for such eruptions (e.g., Klimchuk & Sturrock 1989; Dahlburg, Antiochos & Zang 1991; Roumeliotis et al. 1994). Recently, we have performed a very massive simulation of extreme shearing of a dipolar field, and although considerable reconnection occurred, we saw no evidence for eruption (DeVore & Antiochos 2000). The field does expand outward as a result of continued shearing, and this expansion can become exponentially fast for very large shear (e.g., Roumeliotis, Sturrock & Antiochos 1994; Mikic & Linker 1994; Sturrock, Roumeliotis & Antiochos 1995). This expansion process may well be able to account for many slow CMEs which never exceed the slow solar wind speed ≤ 400 km s^{-1}, but simple expansion cannot account for the fast $\sim 2,000$ km s^{-1} CME/eruptive flares associated with strong δ-sunspot regions. These appear in the field of view of the LASCO coronagraphs on SOHO with velocities much greater than the fast solar wind, and *slow down* in the upper corona (Sheeley, *private communication*).

CME/eruptive flares must be driven by an explosive release of magnetic energy, but the configuration of 1 does not appear to exhibit this type of behavior. The fundamental problem has been elucidated by Aly (1984,1991) and Sturrock (1991): a magnetically dominated flux system cannot have more energy in a closed configuration than in its fully open state. Consequently, the sheared field in our prominence model (Figures 1 and 2) cannot contain enough energy to erupt spontaneously, forcing the overlying unsheared field outward towards infinity as well.

Recently, we have proposed an idea "magnetic breakout" that solves this long-standing problem (Antiochos 1998; Antiochos, DeVore & Klimchuk 1999). The key to solving the energy limitation is to remove the unsheared overlying flux while keeping it closed at all times. This is impossible for a bipolar flux system like the field of Figures 1 and 2, but in a multipolar flux system, magnetic reconnection can do precisely this trick. Figure 4 shows the essential physics of our model. The magnetic topology consists of four distinct flux systems. Strongly sheared (dark blue) field lines are emerging at the equatorial neutral line and pushing outward. These field lines, which correspond to dipped prominence field, are being held down by the overlying, unsheared (light blue) field lines that are part of the same flux system. If this were the only flux system present, then no eruption could occur, but reconnection in the corona *above* the blue system converts blue and red flux into green flux, thereby removing it from overlying the equatorial neutral line and allowing the sheared field to "breakout". This reconnection is evident in the Figure. Our simulations (Antiochos, DeVore & Antiochos 1999) have verified that this model does circumvent (but not violate) the Aly-Sturrock energy limit and produce the magnetic free energy required to account for fast eruptions. Note also that, in agreement with observations, the lowest lying sheared field — down to the photospheric neutral line — can open up with the breakout model, a result which is not possible with tether cutting.

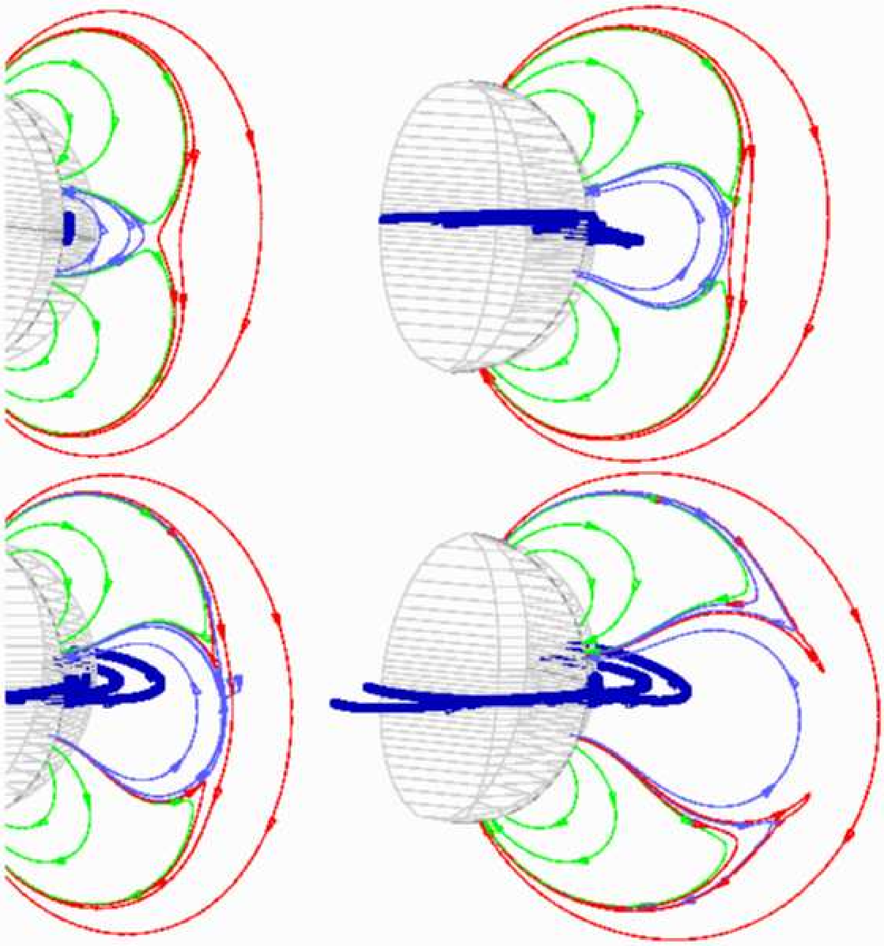

Figure 4: Magnetic field evolution from a "breakout" simulation.

The most important feature of the breakout model is that it produces an explosive eruption. The rate of upward expansion is controlled by the rate of reconnection at the null which, in turn, is controlled by the thickness of the current sheet at the null. But as the system expands outward, the current sheet becomes thinner and thinner, so that the reconnection proceeds ever faster. Hence, there is a natural feedback process between reconnection and expansion which leads to an exponentially growing evolution. This feedback process is evident in Figure 4. Initially, and for low shear, the red and blue field lines across the null are well separated, so that any reconnection that occurs is too slow to be significant to the evolution. Therefore, the shear and the magnetic free energy can build up to appreciable levels. As the shear builds up, however, the system expands outward and the current sheet region at the null becomes longer and thinner, which leads to faster reconnection. The reconnection removes unsheared constraining flux, leading to faster expansion. We conclude, therefore, that the configuration of Figure 4 represents a robust process for obtaining explosive eruption.

Another attractive feature of our "breakout" model is that it can explain why large eruptive flares usually are associated with the appearance of active region magnetic fields in certain unusual configurations: the so-called δ-spot active regions (Zirin 1988), in which two or more sunspot umbra of opposite polarity form within the same penumbra. Simple bipolar regions, on the other hand, are usually inactive. The key point is that the magnetic complexity of, at least, a δ-spot is needed in order to have in 3D a four flux system that is equivalent to the topology of Figure 4 (Antiochos 1998).

Although a great deal of work remains to be done on the breakout model, especially in 3D, the results so far are convincing. We believe that we now have the basic answer to our third question on the cause of prominence eruption: Reconnection of overlying unsheared flux with neighboring flux systems allows the sheared core field to explode outward.

5. Discussion

An interesting conclusion of the results described above is that in each case, spatial inhomogeneity played a vital role. For the gravitational support question, it was the spatial localization near the neutral line of the photospheric shear that led to the formation of concave up field lines in the corona. For the question of condensation formation, it was the localization of the heating near the chromosphere that led to thermal non-equilibrium. For the question of eruption, the multipolarity structure of the photospheric field was needed in order for reconnection and breakout to occur. The conclusion that inhomogeneity plays a key role in the physics of prominences emphasizes that large-scale numerical calculations are likely to be essential for understanding the Sun's activity.

Finally, we should emphasize that although we have presented an answer to the three basic questions concerning prominences, each of our answers has raised another, and perhaps more basic, question:

1. What is the origin of the magnetic shear?
2. What is the mechanism for heating coronal loops?
3. What is the nature of 3D reconnection?

It may well turn out that these far-reaching questions will also be answered by studying that beautiful phenomenon known as solar prominences.

Acknowledgements

Part of the work described in this paper was performed in collaboration of a number of colleagues, especially C. R. DeVore, J. A. Klimchuk, and P. M. MacNeice. This work was supported in part by ONR and NASA.

References

Aly, J.J. 1984, ApJ, 283, 349

Aly, J.J. 1991, ApJL, 375, L61

An, C.-H., Bao, J.J., & Wu, S.T. 1986, in Coronal and Prominence Plasmas, ed. A. Poland (NASA CP-2442), 51

Antiochos S.K., Shoub, E.C., An, C.-H., & Emslie A.G. 1985, ApJ, 298, 876

Antiochos S.K. & Klimchuk, J.A. 1991, ApJ, 378, 372

Antiochos, S.K., Dahlburg, R.B. & Klimchuk, J.A. 1994, ApJL, 420, L41

Antiochos, S.K. 1998, ApJL, 502, L181

Antiochos, S.K., DeVore, C. R. & Klimchuk, J. A. 1999, ApJ, 510, 485

Antiochos, S.K., MacNeice, P. J., Spicer, D. S., &

Klimchuk, J.A. 1999, ApJ, 512, 985

Antiochos, S.K., MacNeice, P.J., & Spicer, D.S. 2000, ApJ, in press

Aulanier, G. & Demoulin, P. 1998, A&A, 329, 1125

Boris, J.P., & Mariska, J. T. 1982, ApJ, 258, L49

Craig, I.J.D., McClymont, A.N., & Underwood, J.H. 1978, A&A, 70, 1

Dahlburg, R.B., Antiochos, S.K., & Zang T.A. 1991, ApJ, 383, 420

Dahlburg, R.B., Antiochos, S.K., & Klimchuk, J.A. 1998, ApJ, 495, 485

DeVore, C.R. & Antiochos, S.K. 2000, ApJ, in press

Engvold, O., & Jensen, E. 1977, Solar Phys., 52, 155

Gary, G.A., Moore, R.L., Hagyard, M.J., Haisch, B.M. 1987, ApJ, 314, 782

Greene, J.M. 1988, *J. Geophys. Res.*, 93, 8583

Kippenhahn, R. & Schluter, R. 1957, *Z. Astrophys.*, 43, 36

Klimchuk, J.A., Antiochos, S.K., & Mariska, J.T. 1987, ApJ, 320, 409

Klimchuk, J.A. & Sturrock, P.A. 1989, ApJ345, 1034

Kuperus, M. & Raadu, M.A. 1974, A&A, 31, 189

Mariska, J.T., & Boris, J.P. 1983, ApJ, 267, 409

Martin, S. 1990, in IAU Coll. 117, *Dynamics of Quiescent Prominences*, ed. V. Rudzdjak & E. Tandberg-Hanssed (Lecture Notes in Physics, Vol 363), 1

Martin, S. & McAllister, A.H. 1997, in Geophys. Monograph 99, *Coronal Mass ejections*, ed. N. Crooker, J. Joselyn, & K. Feynman, (Washington: AGU), 127

Martin, S.F. 1998, Solar Phys., 182, 107

Mikic, Z. & Linker, J.A. 1994, ApJ, 430, 898

Mok, Y., Drake, J.F., Schnack, D.D., & Van Hoven, G. 1990, ApJ, 359, 228

Moore, R.L. & Roumeliotis, G. 1992, *Eruptive Solar Flares*, ed. Z. Svestka, B.V. Jackson, & M.E. Machado (Berlin: Springer)

Pikel'ner, S.B. 1971, Solar Phys., 17, 44

Poland, A.I. & Mariska, J.T. 1986, Solar Phys., 104, 303

Priest, E.R., & Smith, E.A. 1979, Solar Phys., 64, 217

Ribes, E. & Unno, W. 1980, A&A, 91, 129

Rosner, R., Tucker, W.H., & Vaiana, G.S. 1978, ApJ, 220, 643

Roumeliotis, G., Sturrock, P.A., & Antiochos, S.K. 1994, ApJ, 423, 847

Schmieder, B., Demoulin, P., Aulanier, G., & Golub, L. 1996, ApJ, 467, 881

Sturrock, P.A. 1991, ApJ, 380, 655

Sturrock, P.A. 1989, Solar Phys., 121, 387

Sturrock, P.A., Roumeliotis, G. & Antiochos, S.K. 1995, ApJ, 443, 804

Tandberg-Hanssen, E. 1995, *The Nature of Solar Prominences*, (Dordrecht: Kluwer)

Vesecky, J.F., Antiochos, S.K., & Underwood, J.H. 1979, ApJ, 233, 987

Wolfson, R. 1993, ApJ, 418, 382

Zirker, J.B., Engvold, O., & Martin, S.F. 1998, Nature, 396, 440

Zirin, H. 1988, Astrophysics of the Sun (Cambridge Univ. Press: Cambridge)

Discussion

K.D. Leka: The model of the CME, the overlying field lines that you showed spanned from solar north to solar south with the prominence at the equator. Is this model and its general picture of the magnetic configuration/complexity applicable also to a single hemisphere, perhaps an active region and the surrounding overlying fields?

S. Antiochos: The breakout model does, indeed, apply to an active region. In fact, I believe that it is more suitable for fast CMEs originating from active regions than from quiet regions. I have argued (Antiochos 1998), that the topology of Figure 4 is exactly that of a delta-sunspot region. These are well-known to be the sources of strong eruptive flares.

N. Nitta: How does your model compare with the three-part structure of a CME? Why is the core slower than the frontal loop?

Is the strong field really a necessary condition for a CME, when we know that a major event (like the one on 14 April 1994) can happen in a quiescent area?

S. Antiochos: Since our code cannot follow the evolution beyond the initial acceleration phase, I cannot say whether a three part structure forms in the model or whether the core would expand slower than the front. However, it seems likely since the erupting field of Figure 4 divides naturally into unsheared-outer and sheared-core field.

A strong field is necessary for a fast CME, > 1000 km/s. Slow CMEs which accelerate only up to slow solar wind speeds do not need strong field.

Test on the parameter dependence of coronal heating models

P. Démoulin[1], C.H. Mandrini[2], J.A. Klimchuk[3]

[1] Observatoire de Paris, section Meudon, DASOP, UMR 8645 (CNRS), F-92195 Meudon Principal Cedex, France
[2] Instituto de Astronomía y Física del Espacio, IAFE, CC. 67 Suc. 28, 1428 Buenos Aires, Argentina
[3] Naval Research Laboratory, Code 7675, Washington DC 20375-5352, USA

Abstract. The motivation of this work has been to provide observational constraints on coronal heating models by testing their predictions for the heating rate as a function of several physical parameters.
In Mandrini et al. (1999), we have investigated how the magnetic field strength, $< B >$, of coronal flux tubes depends on the end-to-end length, L, of the tube. For flux tubes of intermediate length, $50 \leq L \leq 300$ Mm, corresponding to the soft X-ray loops in a study by Klimchuk & Porter (1995), we find a universal scaling law of the form $< B > \propto L^{\delta}$, where $\delta = -0.88 \pm 0.3$. By combining this with the Klimchuk & Porter result that the heating rate scales as L^{-2}, we can test different models of coronal heating. We find that models involving the gradual stressing of the magnetic field, by slow footpoint motions, are in generally better agreement with the observational constraints than are wave heating models.

1. Introduction

Since it was realized that the solar corona is two orders of magnitude hotter than the underlying photosphere, scientists have puzzled over the reason for these extreme conditions. A number of plausible ideas to characterize the physical mechanism have been proposed, including the dissipation of stressed, current-carrying magnetic fields or the dissipation of MHD waves. Recognizing that loops are the fundamental building blocks of the corona, Klimchuk & Porter (1995) attacked the coronal heating problem by determining scaling laws for loops observed by the Soft X-ray Telescope (SXT) aboard *Yohkoh* (see also Porter & Klimchuk, 1995). They found that loop temperature and length are statistically uncorrelated and that pressure varies inversely with length to approximately the first power. Since the lifetimes of the loops are much longer than their cooling times, the authors used quasistatic loop equilibrium theory to infer that the volumetric heating rate scales inversely with length to approximately the second power. This is an important result, since different coronal heating models make different predictions about what the scaling between heating rate and length should be. Klimchuk & Porter were unable to make definitive tests, however, because the model predictions depend upon the statistical relationship that exists between field strength and loop length, and this was unknown at the time of their study. All that could be said was that models are consistent with the SXT observations only if $B \propto L^{\delta}$, where B is the field strength, L is the length, and the power-law index δ is model dependent.

In order to test different models of coronal heating, Mandrini et al. (1999) have investigated how the magnetic field strength of coronal flux tubes depends on the end-to-end length of the tube. Using photospheric magnetograms from both observed and idealized active regions, we computed potential, linear force-free, and magnetostatic extrapolation models. For each model, we then determined the average coronal field strength, $< B >$, in approximately one thousand individual flux tubes with regularly spaced footpoints. Scatter plots of $< B >$ versus length, L, are characterized by a flat section for small L and a steeply declining section for large L. They are well described by a function of the form $< B >= C_1 + C_2 \ \log L + C_3/2 \ \log(L^2 + S^2)$, where $C_2 \approx 0$, $-3 \leq C_3 \leq -1$, and $40 \leq S \leq 240$ Mm is related to the characteristic size of the active region. There is a tendency for the magnitude of C_3 to decrease as the magnetic complexity of the region increases. For flux tubes of intermediate length, $50 \leq L \leq 300$ Mm, corresponding to the soft X-ray loops in a study by Klimchuk & Porter (1995), we find a universal scaling law of the form $< B > \propto L^{\delta}$, where $\delta = -0.88 \pm 0.3$.

Here, our goals are to combine the above result with the Klimchuk & Porter result that the heating rate scales as L^{-2}, in order to test different models of coronal heating.

2. An overview on coronal heating models

Models or theories of coronal heating can be divided into two main categories: stressing models, in which energy is extracted from coronal magnetic fields that are stressed by slow footpoint motions, and wave models, in which energy is deposited by waves that are incident from below. These are also sometimes referred to as direct current (DC) and alternating current (AC) models, respectively. Many models address the question of how the free magnetic energy or wave energy is dissipated, while others are concerned only with the origin of this energy and do not prescribe a specific dissipation mechanism. We now describe briefly a number of different models, first considering those in the stressing category and then considering those in the wave category. The models are listed in Table 1

	N^0	References	Scaling law	Parameters
Stressing Models (DC)				
Stochastic buildup	1	Sturrock & Uchida 1981,	$B^2L^{-2}V^2\tau$	
–		Berger 1991		
Critical angle	2	Parker 1988,	$B^2L^{-1}V\tan\theta$	
–		Berger 1993		
Critical twist	3	Galsgaard & Nordlund 1997	$B^2L^{-2}VR\phi$	
Reconnection $\propto v_A$	4	Parker 1983	$BL^{-2}\rho^{1/2}V^2R$	
Reconnection $\propto v_{A\perp}$	5	Parker 1983, modified	$B^{3/2}L^{-3/2}\rho^{1/4}V^{3/2}R^{1/2}$	
Current layers	6	van Ballegooijen 1986	$B^2L^{-2}V^2\tau\log R_m$	
–	7	Hendrix et al. 1996	$B^2L^{-2}V^2\tau S^{0.1}$	
–	8	Galsgaard & Nordlund 1996	$B^2L^{-2}V^2\tau$	
Current sheets	9	Aly & Amari 1997	$B^2L^{-1}V_{ph}^2\tau$	
Taylor relaxation	10	Heyvaerts & Priest 1984,	$B^2L^{-2}V_{ph}^2\tau$	
		Browning & Priest 1986,		
		Vekstein et al. 1993		
Turbulence with:				
Constant dissipation coefficients	11	Einaudi et al. 1996,	$B^{3/2}L^{-3/2}\rho^{1/4}V^{3/2}\mathrm{R}^{1/2}$	
		Dmitruk & Gómez 1997		
Closure	12	Heyvaerts & Priest 1992,	$B^{5/3}L^{-4/3}\rho^{1/6}V^{4/3}\mathrm{R}^{1/3}$	
		Inverarity et al. 1995,		
		Inverarity & Priest 1995a		
Closure + spectrum	13	Milano et al. 1997	$B^{s+1}L^{-1-s}\rho^{(1-s)/2}V^{2-s}\mathrm{R}^s$	$s=0.7, m=-1.$
	14			$s=1.1, m=-2.5$
Wave Models (AC)				
Resonance	15	Hollweg 1985	$B^{1+m}L^{-3-m}\rho^{-(1+m)/2}$	$m=-1.$
–	16			$m=-2.$
Resonant absorption	17	Ofman et al. 1995,	$B^{1+m}L^{-1-m}\rho^{-(1+m)/2}$	$m=-1.$
–	18	Ruderman et al. 1997		$m=-2.$
–	19	Halberstadt &	$B^{1+m}L^{-m}\rho^{-(m-1)/2}$	$m=-1.$
–	20	Goedbloed 1995		$m=-2.$
Current layers	21	Galsgaard & Nordlund 1996	$BL^{-1}\rho^{1/2}V^2$	
Turbulence	22	Inverarity & Priest 1995b	$B^{5/3}L^{-4/3}\mathrm{R}^{1/3}$	

Table 1: Summary of the scaling law for different models of coronal heating.

together with the scaling laws that they predict. The parameters included in these laws are defined either in this section or in §3. We note that the parameter R that appears in many of the scaling laws cannot always be interpreted straightforwardly as the loop radius (See the discussion in Mandrini et al., 1999).

2.1. Stressing models

Photospheric and subphotospheric motions displace magnetic footpoints in both random and systematic ways and can include both translational and rotational components. The magnetic free energy that is pumped into the field can be released in real time or stored in the field to be released later. Thus, the resulting plasma heating can be steady, quasi-steady, or highly episodic, depending on the model. Quasi-steady heating refers to situations where the time interval between heating events is short compared to the cooling time by radiation and thermal conduction.

Stochastic Buildup. Model 1 (Sturrock & Uchida 1981; Berger 1991) considers the random twisting of individual flux tubes. The energy grows linearly with time, on average, and is assumed to dissipate episodically at intervals that are long compared with the correlation time of the flow. The heating events can be large or small, and can eliminate all or part of the twist. This scaling law also applies to stochastic energy buildup resulting from random translation motions.

Critical Angle. When the random walk step size is not short compared to the correlation length, the field becomes entangled and braided, and the energy builds quadratically with time in a monotonic fashion. This is the scenario in model 2 (Parker 1988; Berger 1993), which supposes that heating occurs when a critical angle θ is reached between adjacent misaligned flux tubes. Parker suggests that a steady state is set up in which dissipation balances energy input to maintain the angle at or close to the critical value. In fact, the same scaling law applies even if the heating is highly episodic and the angle decreases substantially between events.

Critical Twist. Model 3 (Galsgaard & Nordlund 1997) is similar, except that energy release occurs when a flux tube reaches a critical twist angle, ϕ, perhaps due to the onset of a kink instability. Note that ϕ is the end-to-end angular rotation of the twisted tube, which is different from θ.

Reconnection. Magnetic reconnection may be responsible for the conversion of magnetic to thermal energy in the above models, but this is not explicitly treated. In model 4 (Parker 1983), it is the prescribed mechanism. It is assumed to occur at tangential discontinuities (current sheets) that are postulated to form even in simple magnetic configurations when footpoints are displaced by continuous motions. The scaling law is derived by equating the magnetic reconnection rate with the energy buildup rate. If we modify Parker's original derivation to account for the fact that the reconnection rate is likely to depend on the transverse field strength, rather than the total field strength, we obtain model 5, with a somewhat different scaling law.

Current Layers. There is considerable skepticism that current sheets will actually form from continuous footpoint motions unless the coronal magnetic field is sufficiently complex (contains nulls, separatrices, etc.). Nonetheless, there is widespread agreement that currents can easily become concentrated in layers of small but finite thickness. In model 6 (van Ballegooijen 1986), energy that is pumped into the field over large scales gradually goes to smaller and smaller scales until eventually the scale is small enough for Ohmic dissipation to be effective. Models 7 (Hendrix et al. 1996) and 8 (Galsgaard & Nordlund 1996) are fundamentally similar to model 6, except that they involve MHD simulations. Simple footpoint shearing motions are imposed at the boundary with the direction of motion rotating by 90^0 at time intervals selected randomly. Currents develop exponentially at stagnation points in the corona, but they are dissipated rather suddenly after growing for only about one correlation time of the driver. No significant braiding occurs.

Current Sheets. Model 9 (Aly & Amari 1997) considers the formation and destruction of true current sheets in magnetic configurations containing X-points. Such sheets appear and grow naturally from X-points in the presence of a steady flow. It is proposed that these sheets dissipate episodically, by magnetic reconnection, in a sequence of energy release events.

Taylor Relaxation. Model 10 (Heyvaerts & Priest 1984; Browning & Priest 1986; Vekstein, Priest & Steele 1993) makes use of Taylor's well known conjecture (1974) that magnetic fields relax via reconnection to the lowest energy state that conserves helicity—the linear force-free state. In this scenario, footpoint motions produce nonlinear force-free fields, and these fields episodically relax to the corresponding linear field having the same helicity, thereby releasing energy.

Turbulence. Turbulence may develop in the corona, where the Lundquist number exceeds the critical threshold by many orders of magnitude. Two different approaches have been used to study turbulent heating in the corona. Model 11 (Einaudi et al. 1996; Dmitruk & Gómez 1997) involves MHD simulations in a two-dimensional plane corresponding to a cross-sectional cut across a flux tube. The coefficients of resistivity and kinematic viscosity are constant and, for computational reasons, much larger than actual coronal values. Turbulence develops as part of the time-dependent solution and is not assumed *a priori*. Models 12 (Heyvaerts & Priest 1992; Inverarity, Priest & Heyvaerts 1995; Inverarity & Priest 1995a) and 13 (Milano, Gómez & Martens 1997) are fully three dimensional, but the nonlinear terms in the Equations are replaced by diffusion terms which mimic the effects of an assumed turbulence. The turbulent diffusion coefficients are free parameters and are determined self-consistently according to "closure models" that relate the magnitudes of the coefficients to the magnitude of the energy cascade and, hence, the magnitude of the energy input by footpoint driver motions. These motions are assumed to have a Kolmogorov spectrum in wavenumber ($\propto k^{-5/3}$), and model 13 also includes a power-law spectrum in frequency ($\propto \omega^m$). The parameter s in the scaling law is related to m as indicated in the last column of Table 1.

2.2. Wave models

Waves occur in coronal loops whenever the time scale of the motions is shorter than the end-to-end Alfvén travel time. Although waves can be generated directly in the corona, such as by bursty reconnection, we do not consider that situation here since the energy that powers the waves resides initially in the stressed coronal magnetic fields. We instead concentrate on models in which the waves are generated at the base of the corona, possibly by photospheric turbulence, and propagate upward to heat the corona.

Resonance. Because of the steep density and temperature gradients at the footpoints of coronal loops, wave energy can be both reflected and transmitted at the boundary. The loop acts as a driven, leaky, resonance cavity. Model 15 (Hollweg 1985) addresses the conditions that must be met in order for significant energy to be transmitted into the loop from below. The scaling law for this model depends on the power law index of the assumed driver frequency spectrum, m.

Resonant Absorption. Models 17–20 (Ofman, Davila & Steinolfson 1995; Ruderman et al. 1997; Halberstadt & Goedbloed 1995) consider a different aspect of loop resonance. Whenever the Alfvén velocity is nonuniform in a loop cross-section a phenomenon know as resonant absorption occurs. The wave amplitude is enormously enhanced in a narrow layer where the local Alfvén resonance frequency matches the frequency of the global loop oscillations. Gradients in the magnetic field and velocity are extremely large in this layer, and the wave energy is easily dissipated by Ohmic and viscous processes.

Current Layers. Model 21 (Galsgaard & Nordlund 1996) is basically the same model as model 8 but taken in the limit of rapid boundary excitations compared to the the end-to-end Alfvén travel time. Compared to previous wave models, one major difference is that the boundary condition is not described by a power-law spectrum in frequency, but rather by a series of shearing motions randomly modified.

Turbulence. Model 22 (Inverarity & Priest 1995b) is similar to model 12 except that the footpoint motions have a high enough frequency to produce waves rather than a quasistatic evolution.

3. How can observations test heating models?

The aim of coronal-heating models is to identify the mechanism responsible for the energy input at coronal heights. However, many of the hypotheses involved (e.g. the formation of small scale lengths) are not directly verifiable with present observations. One test that is typically applied to models is to compare the predicted heating rate with that obtained from observations. Several models pass this test successfully for both quiet Sun and active region conditions. The aim of our work is, finally, to provide more severe constrains by comparing the dependence given by models with those deduced from observations.

As shown in Table 1, most coronal heating models give a heating rate per unit volume which can be expressed in the following generic way:

$$H_m \propto B^a L^b \rho^c V^d R^e \,, \tag{1}$$

where B and ρ are the coronal field strength and plasma density, L is the loop length, V is the transverse velocity at the base of the corona, and R is the loop radius (for most models).

If B, ρ, V, and R have a known power-law dependence on L, Equation 1 reduces to the simple form

$$H_m \propto L^{\alpha_m} \,, \tag{2}$$

where the "m" subscript indicates a model quantity. This can be compared to the observed relationship

$$H \propto L^{\alpha} \tag{3}$$

determined from *Yohkoh* data by Porter & Klimchuk 1995. If α_m and α agree to within the uncertainties, then the model can be considered viable. Otherwise, it must be rejected. Porter & Klimchuk obtained independent estimates of α based the the observed relationships $P \propto L^{\beta}$ and $T \propto L^{\gamma}$. The pressure scaling gives a most probable value for α of -1.95 with a 90% confidence interval of [-3.11, -0.95], while the temperature scaling gives -2.00 and [-4.59, -0.67]. Note that the most probable values are essentially identical, and in §4. we refer to a single result.

3.1. Effects of boundary conditions

The quantities V and R in Eq.(1) refer to the base of the corona, which is separated from the photosphere by the chromosphere and transition region. On the other hand, the driver motions which displace the coronal magnetic field are associated with convection, or some other turbulent or organized flows that originate at or below the photosphere. How are V and R related in these two regions? One possibility, which we refer to as Case (a), is that the coronal and photospheric quantities are identical:

$$R = R_{ph}\,, V = V_{ph} \qquad \text{(Case (a))}\,. \tag{4}$$

This is the assumption made for nearly all published models.

A second possibility, Case (b), takes into account the well-known fact that the photospheric field is strongly concentrated in thin flux tubes. Magnetic flux conservation implies:

$$R \approx R_{ph}\sqrt{\frac{B_{ph}}{B}} \qquad \text{(Case (b))}\,. \tag{5}$$

Any braiding or shearing motions in the photosphere are transmitted to the bottom of corona with nearly the same amplitude. However, the velocity of twisting motions will be amplified due to the flux tube expansion (van Ballegooijen 1986). For a stationary twisting motion, the twisting velocity at the base of the corona is:

$$V \approx V_{ph}\sqrt{\frac{B_{ph}}{B}} \qquad \text{(Case (b))}\,. \tag{6}$$

Because plasma densities are so much larger in the photosphere than in the corona, it is reasonable to suppose that photospheric quantities are essentially unaffected by the physical conditions of the corona. This suggests that B_{ph}, R_{ph}, and V_{ph} are statistically independent of the coronal loop length, L. With this hypothesis, the power-law index in Eq.(2) has the form α_m given by:

$$\alpha_m = \delta a + b + \epsilon c \qquad \text{for Case (a)}\,, \tag{7}$$

and

$$\alpha_m = \delta(a - (d+e)/2) + b + \epsilon c \qquad \text{for Case (b)}\,, \tag{8}$$

where we have assumed that other parameters intrinsic to some of the models, are also statistically independent of the loop length L.

4. Test on the heating models

Fig.1 shows the values of α_m predicted by the different models in Table 1. The derivation of the error bars is explained in Mandrini et al (1999). The horizontal line in Fig.1 indicates the observed value, α, determined by Porter & Klimchuk. The shaded bands

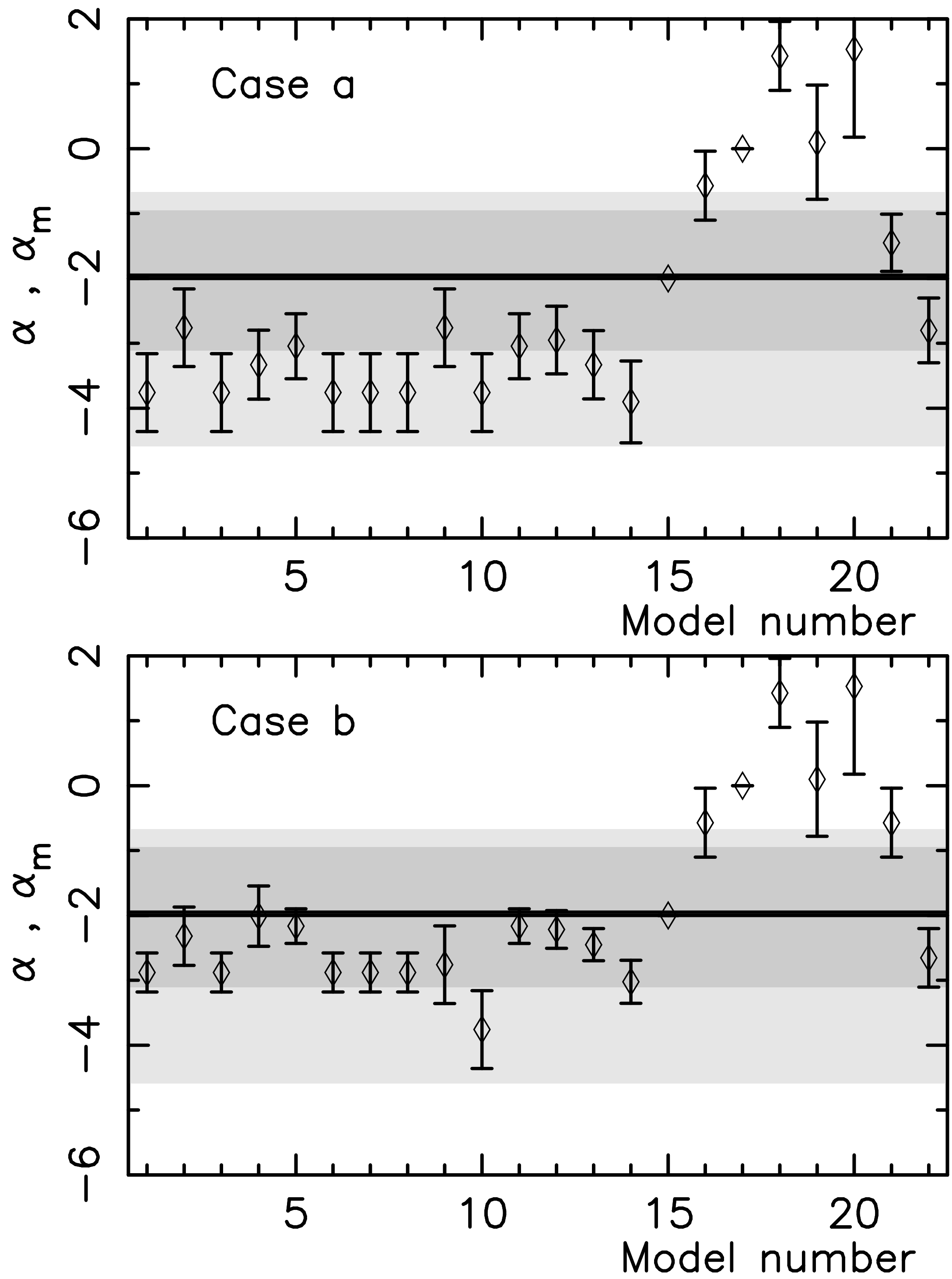

Figure 1: Comparison of the heating rate versus length scaling law, $H \propto L^{\alpha}$, as deduced from observations and models. The plotted points with error bars indicate the power-law index α_m predicted by the models listed in Table 1. The horizontal line at $\alpha = -2$ is the most probable value deduced from observations (Porter & Klimchuk, 1995), with the dark (resp. light) shaded band representing the 90% confidence interval associated with the pressure (resp. temperature) measurements.

indicate the 90% confidence intervals determined with the pressure scaling (dark, narrow band) and the temperature scaling (light, broad band). In order for a model to be strictly consistent with the *Yohkoh* observations, its error bar must overlap with the dark band. Only some of the models satisfy this requirement. However, in all but models 17–20, the disagreement is quite small, and given the approximate nature of the error estimations, it is not appropriate to reject these models as impossible.

We nonetheless find that some models are in better agreement with the observations than others. In particular, with the hypothesis of no flux expansion (Case (a)), models in which energy release occurs at a critical angle of the magnetic field (Parker 1988; Berger 1993; model 2) or which involve magnetic reconnection (Parker 1983; models 4 and 5; Aly & Amari 1997; model 9) or which involve turbulence (Einaudi et al. 1996; Dmitruk & Gómez 1997; Heyvaerts & Priest 1992; Inverarity, Priest & Heyvaerts 1995; Inverarity & Priest 1995a; models 11 and 12) predict α_m very close to the most probable value. Wave heating models, especially models 17-20, exhibit the poorest agreement with these observations with the remarkable exception of model 15 (Hollweg 1985) while models 21 and 22 (Galsgaard & Nordlund 1996; Inverarity & Priest 1995b) are both close to the most probable value of α.

Taking into account the magnetic flux expansion (Case (b)), nearly all the stressing models (except model 10 which involves Taylor relaxation) are closer to the most probable value determined by Porter & Klimchuk. This is a warning that flux-tube expansion should be treated in models (rather than the often used uniform field).

Acknowledgements

We thank Drs. Giorgio Einaudi, Daniel Gómez, Joe Hollweg, Leon Ofman, Grigory Vekstein, and Marco Velli for helpful discussions on their models. P.D. and C.H.M. acknowledge financial support from ECOS (France) and SECYT (Argentina) through their cooperative science program (A97U01). The work of J.A.K. was supported by NASA contract W-19,200.

References

Aly, J.J. & Amari, T. 1997, A&A, 319, 699

Berger, M.A. 1991, A&A, 252, 369

Berger, M.A. 1993, Phys. Rev. Lett., 70, 705

Browning, P.K. & Priest, E.R. 1986, A&A, 159, 129

Dmitruk, P. & Gómez, D.O., 1997, ApJ, 484, L83

Einaudi, G., Velli, M., Politano, H. & Pouquet, A. 1996, ApJ, 457, L113

Galsgaard, K. & Nordlund, A. 1996, JGR, 101, A6, 13445

Galsgaard, K. & Nordlund, A. 1997, JGR, 102, A1, 219

Halberstadt, G. & Goedbloed, J.P. 1995, A&A, 301, 559

Hendrix, D.L., Van Hoven, G., Mikić, Z. & Schnack, D.D. 1996, ApJ, 470, 1192

Heyvaerts, J. & Priest, E.R. 1984, A&A, 137, 63

Heyvaerts, J. & Priest, E.R. 1992, ApJ, 390, 297

Hollweg, J.V. 1985, in Adv. in Space Plasma Physics, ed. B. Buti (Singapore: World Scientific Pub. Co.), 77

Inverarity, G.W., Priest, E.R. & Heyvaerts, J. 1995, A&A, 293, 913

Inverarity, G.W. & Priest, E.R. 1995a, A&A, 296, 395

Inverarity, G.W. & Priest, E.R. 1995b, A&A, 302, 567

Klimchuk, J. A., & Porter, L. J. 1995, Nature, 377, 131

Mandrini, C.H., Démoulin, P., Klimchuk J.A., ApJ, 1999, in press

Milano, L.J., Gómez, D.O., Martens, P.C.H. 1997, ApJ, 490, 442

Ofman L., Davila, J.M. & Steinolfson R.S. 1995, ApJ, 444, 471

Parker, E.N. 1983, ApJ, 264, 642

Parker, E.N. 1988, ApJ, 330, 474

Parker, E.N. 1994, Spontaneous Current Sheets in Magnetic Fields, Oxford University Press, Oxford

Porter, L.J. & Klimchuk, J.A. 1995, ApJ, 454, 499

Ruderman, M.S., Berghmans, D., Goosens, M. & Poedts, S. 1997, A&A, 320, 305

Sturrock, P.A. & Uchida, Y. 1981, ApJ, 246, 331

van Ballegooijen, A.A. 1986, ApJ, 311, 1001

Vekstein, G.E., Priest, E.R. & Steele, C.D.C. 1993, ApJ, 417, 781

Discussion

S. Antiochos: How about the absolute magnitude of the heating as predicted by the models? Is that sufficient to explain the observed heating losses in coronal loops?

P. Démoulin: Most models in table I give easily the right order of energy input in the corona when using standart values of the solar atmosphere (others have been eliminated as possible explanation of the coronal heating, e.g. acoustic waves). However some models give a heating which is smaller than observed, e.g. a factor around 40 too low in the case of model 6 (van Ballegooijen 1986). For the wave models 15–20, there is a large uncertainty on the power law index m. With a flat spectrum ($m \approx 0$), there is enough power in the high frequency waves to heat the corona, but the index is likely to be negative (e.g. $m = -1$ for a Kolmogoroff photospheric spectrum) and, in this case, there is not enough available energy at the coronal loop resonance (see e.g. Parker, 1994, section 11.4). Finally, presently data are not precise enough to eliminate models in table I just on the magnitude of the coronal heating produced (an order of magnitude can be easily gained by shifting the parameters within the error bars).

Long-term evolution of an AR

L. van Driel-Gesztelyi[1,2]

[1] Konkoly Observatory, Budapest, Pf. 67, H–1525, Hungary
[2] Observatoire de Paris, DASOP, 92195 Meudon Cedex, France
Visiting professor at the University College London

Abstract. I summarize the results of a complex and comprehensive analysis of the evolution of an isolated active region (AR) in the period of July-November 1996. Using SOHO/MDI full-disc magnetic maps, we follow the magnetic evolution of the AR for several months. We extrapolate the photospheric magnetic fields in the linear force-free approximation and match the modelled field lines with the soft X-ray loops observed with the Yohkoh/SXT in order to diagnose the coronal magnetic shear. We find that while the turbulent motions diffuse the flux, the differential rotation, and possibly twisted flux emergence, increase the magnetic shear. Flares are observed during the first three rotations, while CME events (observed by SOHO/EIT and LASCO) originate from this AR from its emergence throughout its decay. Several early CMEs, while none of the late CMEs, are related to flare events above the GOES B1 level. We find that the late CMEs occur when the magnetic shear, after accumulating for four rotations, reaches a high level and saturates. We propose that CME activity serves as a valve through which the AR could get rid of excess shear and helicity.
Furthermore, we study the evolution of the emissivity and heating correlated with magnetic observables of the AR from its birth throughout its decay. Taking one "snapshot" per rotation at each consecutive central meridian passage (CMP) of the AR, outside the time of flares, we analyse multi-wavelength and multi-instrument data obtained from SOHO (MDI and SUMER), Yohkoh (SXT), GOES and 10.7 cm radio data from DRAO, Canada. We find that the magnetic flux density - emitted radiation relations follow a power-law with exponents which appear to depend on the formation temperature (height) of the emission.

Keywords: solar activity, active region evolution. magnetic field, magnetic shear, flare, CME

1. Introduction

During the second half of 1996, solar activity was dominated by a single active region on the southern hemisphere, which was identified as NOAA AR 7978 when it emerged in July. This "last best region" of the cycle (Harvey and Hudson, 1997) provided a rare opportunity for various studies (e.g. (Orlando et al, 1999, Oláh et al, 1999), mainly, because of the lack of other active regions on the Sun its evolution was relatively undisturbed. The evolution of active regions in each and every detail reflects the evolution of the magnetic field which emerges from below, interacts with its magnetic environment, gets dispersed by persistent large-scale flows and more rapidly evolving supergranular and granular convective flows, and furthermore, gets sheared by the differential rotation (van Driel-Gesztelyi, 1998).

Theoretical MHD models have shown that magnetic shear and twist, exceeding a critical threshold, can lead to the destabilization of large-scale coronal arcades (Amari *et al*, 1996; Mikič & Linker, 1997), indicating that they can be considered to be candidates for the initiation of CMEs. In order to test the theoretical predictions we study, for six solar rotations, the occurrence of flare and CME events originating from an AR in the context of the evolution of the coronal magnetic shear.

It is a generally accepted idea that magnetic field plays an important role in heating the solar atmosphere, thus its evolution of an active region must influence the amount of radiation emitted by them. At least two major recent papers dealt with the relations between radiative output and magnetic observables of solar active regions. Fisher et al (1998), using a great combined sample of Yohkoh/SXT images and HSP (Hawaii) vector magnetograms, analysed the relationship between different magnetic observables and soft X-ray emission. They found that the X-ray luminosity is best correlated with the total unsigned magnetic flux of a given AR. Harvey and White (1999) analysed Ca II K images and Kitt Peak magnetograms and found that the Ca II K (residual) intensity is proportional to the half-power of the magnetic flux density. However, none of these important works dealt explicitly with the evolutionary aspect of active regions, what we aim here.

In former papers (van Driel-Gesztelyi et al, 1999a, Mandrini et al, 1999) we studied the long-term evolution of the magnetic non-potentiality combined with flare and CME activity of this AR. In another paper, using multi-wavelength and multi-instrument data, we analysed the evolution of the heating and emissivity of NOAA 7978 from its birth throughout its decay between July and December 1996 (van Driel-Gesztelyi et al, 1999b). Here, summarizing the above former results, I make an attempt to form a global image of long-term active region evolution.

2. Data

During the period of August-October NOAA 7978 was practically the only sizable AR on the Sun, which allowed us the use of one-dimensional datasets like GOES soft X-ray and

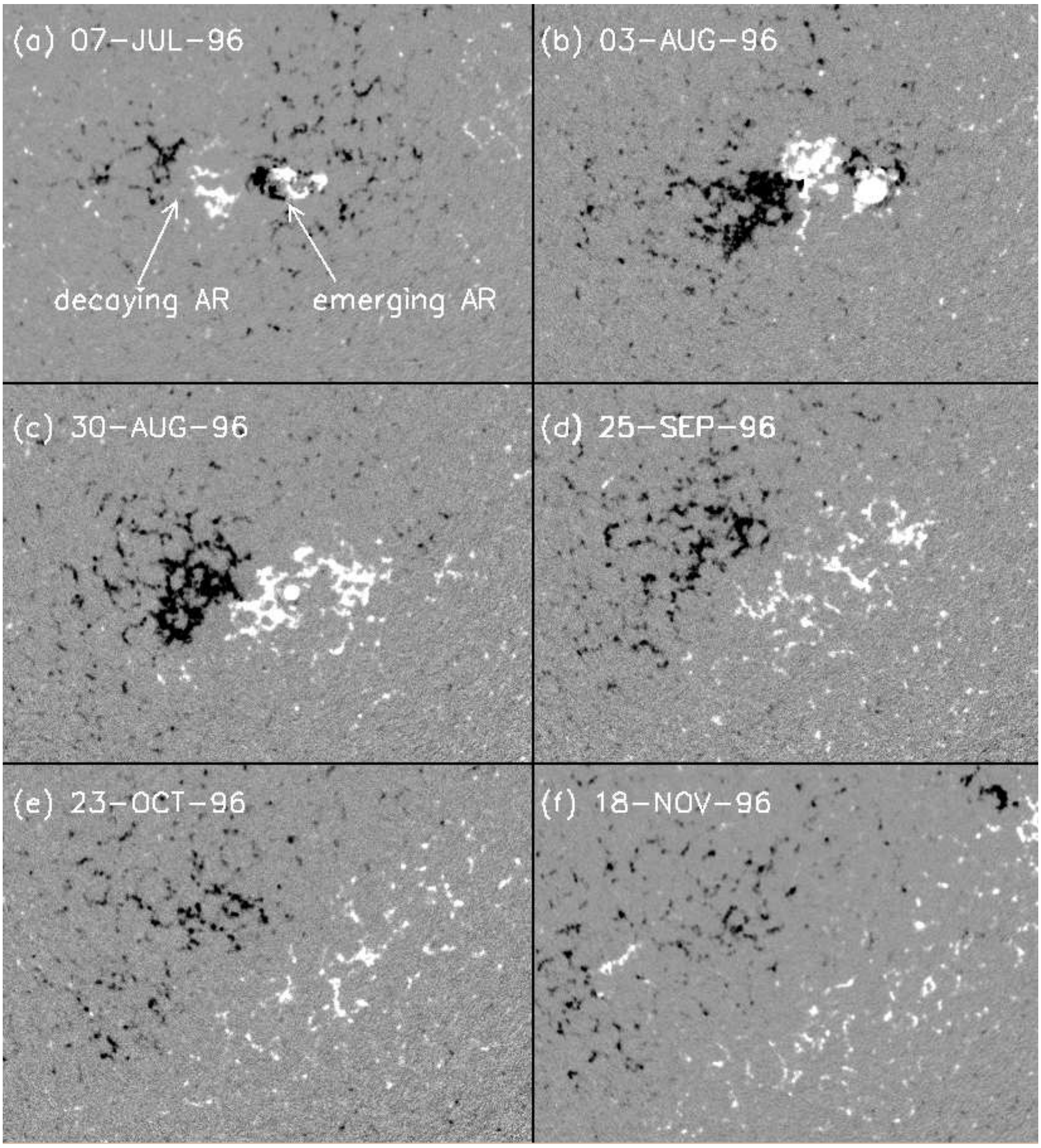

Figure 1: SOHO/MDI magnetic maps show the evolution of the magnetic field distribution of an active region during six months around the time of consecutive central meridian passages (CMPs) of the AR. NOAA AR 7978 was vigorously emerging between 6-10 July, then its decay could be followed for at least six months. Sunspots were present in the AR for two following rotations (CMPs at 2 Aug. and 30 Aug.). The diffusion of the magnetic field is very apparent. The direction of the inversion line is gradually bending about 45°. It is remarkable that any magnetic irregularity in the diffusing bipolar structure is quickly wiped out, presumably by effective flux cancellation processes, the dominant polarity prevails. Note the disappearance of the positive fields of the decaying AR west of the emerging AR between the first and second rotations.

DRAO 10.8 cm radio data besides the two-dimensional SOHO (MDI and SUMER) and Yohkoh/SXT images.

MDI (Michelson Doppler Imager) is one of the twelve experiments on board SOHO, which measures the photospheric manifestation of solar oscillation (Scherrer et al, 1995). Besides the dopplergrams it records the line-of-sight magnetic field, making full-disk magnetograms every 96 minutes. For this analysis we use level-1.5 5-minute averaged data.

SUMER (Solar Ultraviolet Measurements of Emitted Radiation, Wilhelm et al, 1995) performs high-resolution spectral imaging of the Sun at several EUV emission lines. For the present study we use full-disk scans taken in the S VIa 933 Å and SVIb 944 Å lines ($T \approx 2 \times 10^5$ K), which are recorded on different parts of detector A: S VIa on KBr, S VIb on MCP bare. Intensities are calibrated.

The grazing incidence soft X-ray telescope (SXT, Tsuneta et al, 1991) on board of Yohkoh provides images in the 3-60 Å wavelength range. The use of pairs of thin metal filters permits temperature and emission measure analysis of the corona. For this study, we used the thin Al (Al.1) and the aluminum-magnesium sandwich (AlMg) filters.

Geostationary Orbiting Environmental Satellites (GOES) provide soft X-ray irradiance measurements in the 1-8 Å flux range in Wm^{-2}. For our analysis we use low-channel data of the X-ray Sensors (XRS) on board the GOES-9 satellite.

Daily 10.7 cm solar radio flux measurements were recorded at the Dominion Radio Astrophysical Observatory (DRAO) at Pentincton, Canada (Tapping and Charrois, 1994). The daily flux was measured at 17:00, 20:00 and 23:00 UT. The data is given in solar flux units (10^{22} $\mathrm{Wm}^{-2}\mathrm{Hz}^{-1}$) or 10^4 Janskys. Note that both the DRAO and the GOES data were calibrated to 1 AU distance.

3. Magnetic non-potentiality and flare & CME activity of the AR

3.1. Magnetic modelling

We have modelled the field of the AR during six rotations. The modelling has been carried out in the linear force free approach ($\vec{\nabla} \times \vec{B} = \alpha \vec{B}$; α constant) using the extrapolation method described in Démoulin *et al.*, (1997). MDI magnetic field maps at central meridian passage (CMP) have been used as boundary conditions. The free parameter for the model, α, has been chosen in order to fit the shape of the observed SXT loops. We found it impossible to match all the SXT loops at a given time with the same value of α (Figs 2 & 3). In all cases there exists a gradient in the North - South direction. Table 2 shows the evolution of α for six rotations. Keeping the limitations of such diagnostics in mind, we find that AR 7978 emerged in a non-potential state, with the helicity sign corresponding to the southern hemisphere ($\alpha > 0$, see Pevtsov *et al*, 1995). It emerged very close to a pre-existing AR with high helicity in the opposite sense. The latter had vanished by the second rotation. Furthermore, the shear increased from the second to the fourth rotation and then it saturated.

Date 1996	α at the North 10^{-2} Mm^{-1}	α at the South 10^{-2} Mm^{-1}	α of the decaying AR 10^{-2} Mm^{-1}
07 Jul	1.0	–	-5.0
02 Aug	0.75	0.30	–
30 Aug	1.1	0.75	–
25 Sep	1.4	1.00	–
23 Oct	1.4	0.90	–
18 Nov	–	0.90	–

Table 1: Evolution of the shear in the AR – lfff extrapolations.

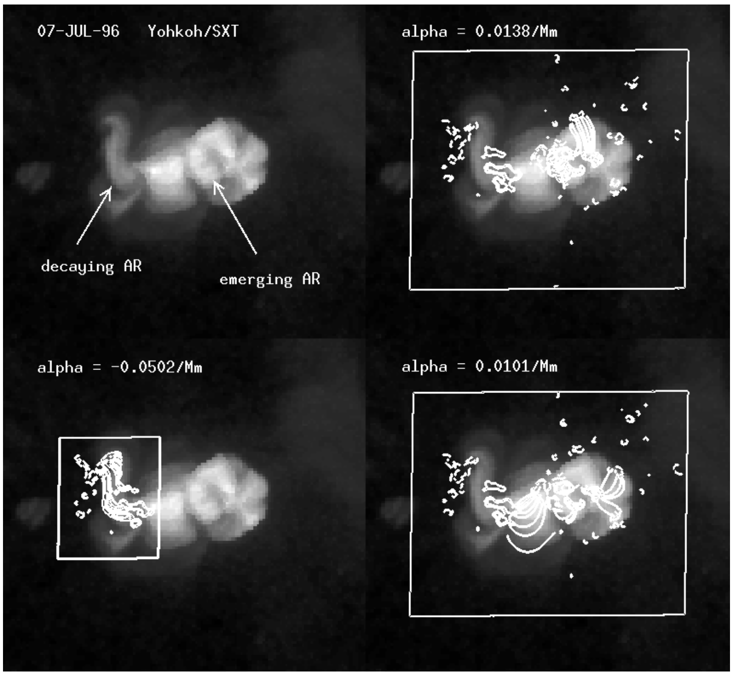

Figure 2: Extrapolated magnetic field lines fitted to coronal loops (SOHO/MDI and Yohkoh/SXT) during the emergence of the AR. The flux appeared already in a non-potential state ($\alpha > 0$). Its interaction with a highly non-potential decaying region ($\alpha < 0$) led to several flares, e.g. the X2.6 flare and CME event on 9 July.

3.2. Flare and CME activity of the AR

Solar activity during the second half of 1996 was dominated by a single active region on the southern hemisphere. The emergence of NOAA AR 7978 was well observed with the SOHO/MDI between 6-10 July 1996, and after that its decay could be followed for at least six more rotations. Table 1 shows that during the vigorous emergence and two following rotations, the AR produced numerous flares (including an X2.6 flare and CME event on July 9, see Dryer *et al.*, 1998) until the disappearance of the main spots by September (see Fig. 1). On the other hand, CME activity, which was at first in several cases related to flare events, continued at a high level for the next three rotations (for an example of the non-flare-related CMEs see e.g van Driel-Gesztelyi *et al*, 1998). The data sources of Table 1 are the GOES X-ray and optical event catalog (http://www.lmsal.com/SXT/operations.html) as well as SOHO/EIT & SOHO/LASCO observations analysed by us (for the LASCO CME list see http://lasco-www.nrl.navy.mil/cmelist.html).

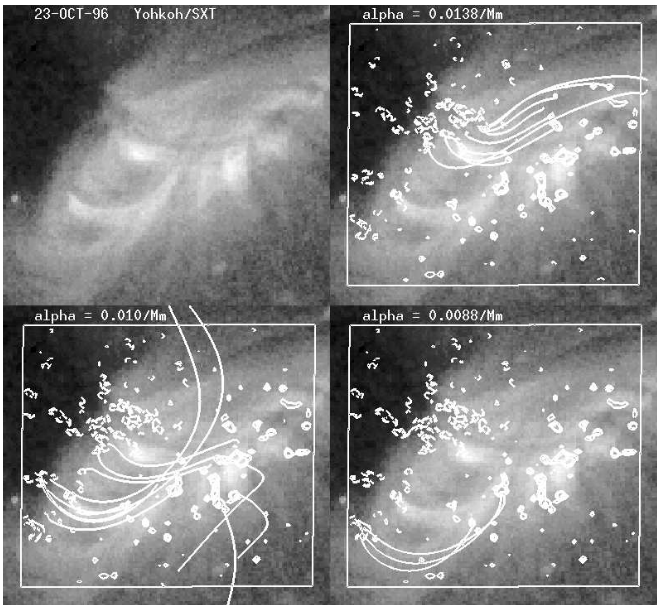

Figure 3: Extrapolated magnetic field lines fitted to coronal loops (SOHO/MDI and Yohkoh/SXT) during the decay phase (fifth rotation) of the AR. Note that α is not uniform and it is high (cf. Table 2).

No. of rot.	Date of CMP 1996	Flares (GOES) X	M	C	B	Type III radio bursts	CME	CME +Flare
1st	07 July	01	02	14	11	2	4	4
2nd	02 Aug.	–	–	–	16	–	8	1
3rd	30 Aug.	–	–	01	08	–	7	2
4th	25 Sep.	–	–	–	–	–	3	–
5th	23 Oct.	–	–	–	–	–	4	–
6th	18 Nov.	–	–	–	–	–	6	–
7th	16 Dec.	–	–	–	–	–	6	–

Table 2: Flare and CME activity in the AR during seven rotations.

4. Emissivity evolution

4.1. Method

Using the images we measured the magnetic flux and the emitted radiation of the active region during the emergence and six more consecutive central meridian passages. We drew the magnetic boundary of the AR "by hand", relying on the detection by the human eye of the steep magnetic field gradient at the boundary using magnetic maps displayed in the same dynamic range (Figs. 1 and 2). We admit that such method brings in some subjective errors, but after carrying out several series of measurements, we did not find greater than about 10 % scatter for the magnetic area and flux. We also used a rectangular area of about 1.6 10^{11} km^2 around the AR for magnetic flux measurements in order to follow the interaction of the newly emerging flux with the pre-existing magnetic environment. This area was always adjusted to the changing solar-terrestrial distance during this half-year period.

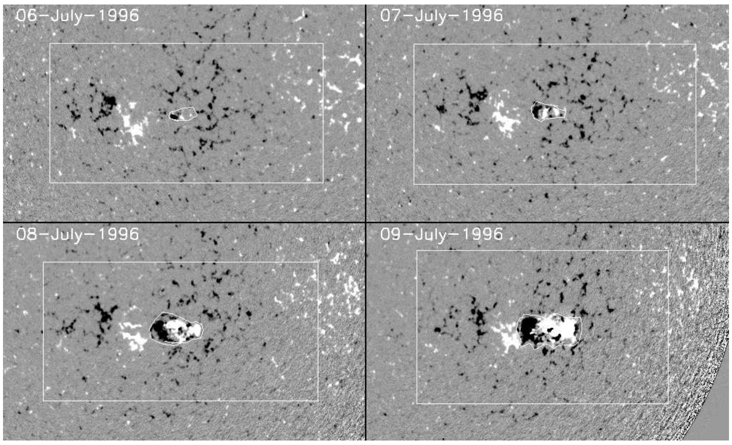

Figure 4: SOHO/MDI magnetic maps show the emergence of NOAA AR 7978, with contours which outline the magnetic area of the growing AR, and another larger area around the AR in which the magnetic flux was measured.

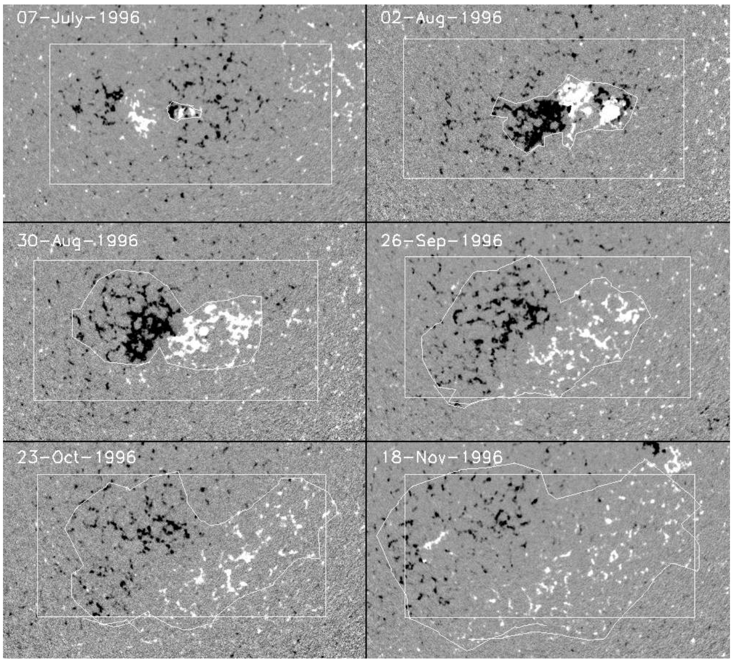

Figure 5: SOHO/MDI magnetic maps show the evolution of NOAA AR 7978 during six solar rotations around the times of central meridian passage. The contours outline the magnetic area of the decaying AR, of which the magnetic flux is getting dispersed. The rectangular area which provided another set of magnetic flux measurements.

The emitted radiation, emission measure and temperature were measured inside the magnetic boundaries of the AR in the images taken closest in time to the central meridian passages.

4.2. Results

We find that the magnetic area of the AR increased roughly linearly at a rate of 1.25 $10^4 \pm 500$ km^{2}sec^{-1}. At the beginning, the X-ray emitting area was larger than the magnetic area, due to interaction of the emerging flux with pre-existing magnetic fields around the AR, i.e. to the formation of bright reconnected loops but it fell behind after the 5th rotation when the magnetic field got very dispersed.

Following the evolution of the magnetic flux in a fixed area of 1.6 10^{11} km^2 containing the growing AR we find an about 20% flux unbalance, due to the fact that the AR emerged in a dominantly negative polarity environment. The total (unsigned) flux inside

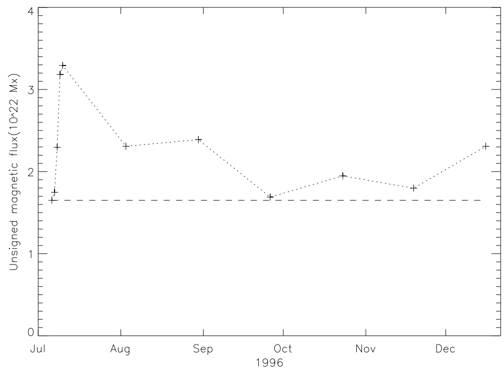

Figure 6: Evolution of the total (unsigned) magnetic flux in a fixed area of 1.6 10^{11} km^2 containing the growing AR. Note that by the fourth rotation the total flux returned to the pre-emergence level.

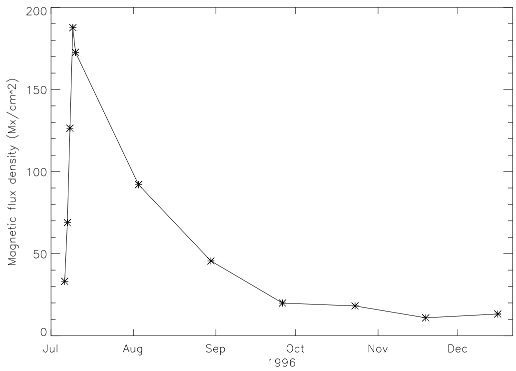

Figure 7: Evolution of the magnetic flux density in the AR versus time. Similarities in the temporal evolution of the magnetic flux density in the AR and the GOES soft X-ray flux suggest physical relationship.

the rectangular area increased two-fold due to the emergence of the AR of 1.5 10^{22} Mx, and it nearly returned to the starting level (i.e. to the total flux in the "box" before the flux emergence) by the fourth rotation (Fig. 3). The increase of the flux in October and after that was due to new flux emergence, i.e. the appearance of minor ARs inside or at the boundary of the decaying AR.

The magnetic flux density (B averaged over the entire AR) reached the highest level (188 Mx cm^{-2}) by the 4th day of the emergence and decreased steadily after that (Fig. 4).

The soft X-ray irradiance (GOES-9) increased steeply during the flux emergence and decreased during the decay phase (outside of flare times). During the evolution process the emissivity did not seem to correlate closely with the area or the total magnetic flux (Fig. 5). The magnetic flux which emerged to form the AR disappeared relatively slowly, followed by an increase after the 4th rotation (Fig. 3), while the SXR emission showed a steep and more steady decrease. On the other hand, intensity, emission measure and temperature shows a better correlation with the magnetic flux density in the AR. We find that the magnetic flux density versus intensity, emission measure and temperature ($\mid B \mid$ vs I, EM and T) of the AR relations follow a power law. These log-log curves show a roughly linear dependence with different slopes. The soft X-ray emission appears to be proportional with the 1.1-1.3 power of the magnetic flux density, while the transition region lines seem to have a power smaller than one (Figs. 6-9).

5. Discussion and conclusions

The flares and CMEs from the early stage of the AR evolution appear to be due to the interaction (cancellation) between the emerging and the pre-existing fields possessing important helicity in the opposite sense. We attribute the shear increase between the

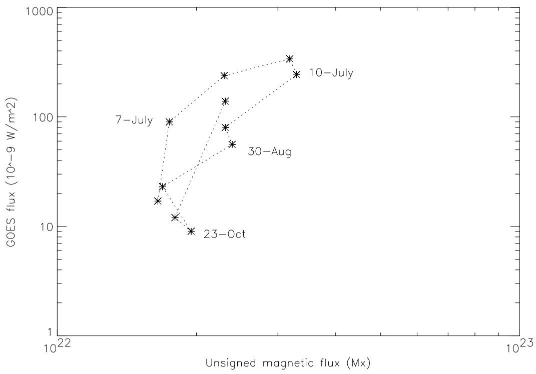

Figure 8: Total magnetic flux over a fixed area of 1.6 10^{11} km^2 around the AR versus the GOES soft X-ray flux indicates a general dependence of the coronal emission on the total magnetic flux. However, roughly the same total flux may relate to very different emission values, depending on the evolutionary stage of the AR.

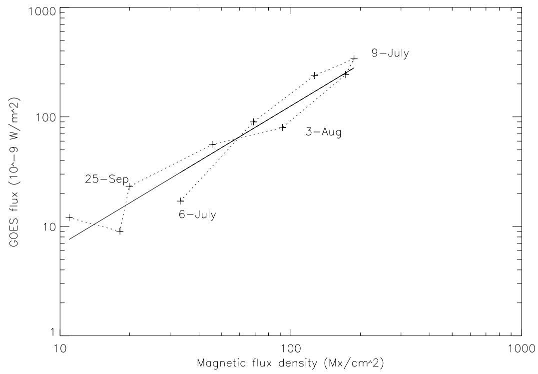

Figure 9: Log-log curve of the magnetic flux density and GOES soft X-ray flux shows a linear function between the two. The X-ray emission appears to be proportional to the 1.3 ± 0.1 power of the magnetic flux density. Note that flux emergence and AR decay may have somewhat different slopes.

second and fourth rotations to twisted flux emergence and shearing by differential rotation. The effect of the differential rotation and even of the emergence of twisted flux did not cease even after four rotations. Still, our results show that the non-potentiality of the AR did not increase any further. We suggest that the shear and helicity which amounted beyond the threshold level was carried away by the CMEs, as suggested by the theory (e.g. Amari *et al*, 1996; Mikič & Linker, 1997).

We find that during the long-term evolution of the AR the magnetic flux density versus intensity, emission measure and temperature ($\mid B \mid$ vs I, EM and T) of the AR relations follow a power-law. The log-log curves of these observables are roughly linear with different slopes for coronal and transition line emission. There is even some difference between the slopes of GOES and Yohkoh/SXT data. Though both of these instruments observe in the soft-X-ray domain, the two wavelength ranges are not identical. The GOES/XRS "window" in the soft channel is between 1-8 Å (Hanser and Sellers 1996, Bornmann et al. 1996), while that of Yohkoh/SXT is in the range $\sim 3-45$ Å at 1% of peak response (Tsuneta et al. 1991). The passbands of the SXT filters used are about $\sim 3-35$ Å (Al.1) and $\sim 3-30$ Å (AlMg). The shorter the wavelength, the higher the temperature, thus GOES "sees" the hottest, SXT with the Al.1 filter the coolest coronal plasma (although the Al.1 and AlMg filters have a similar passband). The exponents follow the same trend: we see the highest one in case of GOES (1.3 ± 0.1) and the lowest with the SXT Al.1 filter, though the difference between the two SXT filters may not be significant (1.07 ± 0.09 for the Al.1 filter and 1.13 ± 0.1 for the AlMg filter). When we go to lower temperature and look at the slopes of the $\mid B \mid$ versus emission in the SVI lines as observed with SUMER, we find that these transition region lines (T $\approx 2 \times 10^5$ K) have a weaker response to the changing magnetic flux density than the soft X-ray radiation. The scatter is large in the data and there is a difference between the S VIa and the S VIb lines, but the

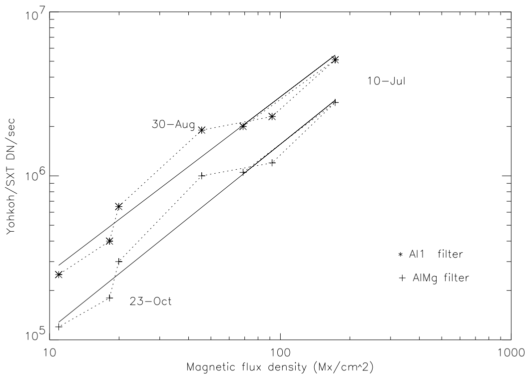

Figure 10: Log-log curves of the magnetic flux density and Yohkoh/SXT DN numbers indicate linearity. The X-ray emission appears to be proportional to the 1.1 ± 0.1 power of the magnetic flux density. Note that this value is somewhat lower than that of the same relation for the GOES flux (cf. Fig. 6 and Table 1).

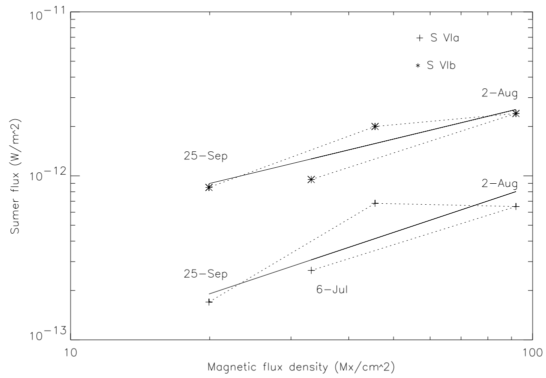

Figure 11: Log-log curves of SUMER S VI line intensities versus magnetic flux density, though the scatter is high for the S VIa line, suggest power laws with exponents of 0.9 ± 0.4 and 0.7 ± 0.2 for these transition region lines – lower values than in the case of the X-ray emission.

exponents are definitely lower than what we found with the SXR radiation. Though the present analysis does not cover a wide range of spectral lines, our results suggest that the exponent in the power law $I \sim \mid B \mid^{exp}$ depends on the formation temperature (or altitude) of the emission. The flattest slope (0.68 ± 0.10) was found with the 10.7 cm radio flux, which has a brightness temperature of $3\ 10^4 K$, but probably at least partially it is of non-thermal origin.

An interesting result is the power-law relation between the magnetic flux density and the soft X-ray temperature: $T \sim \mid B \mid^{0.24 \pm 0.03}$, thus the coronal temperature of the AR is proportional to the quarter power of the magnetic flux density (Fig. 10). The Yohkoh/SXT emission measure seems to have a strong response to the changing magnetic flux density; we found $EM \sim \mid B \mid^{1.3 \pm 0.1}$.

Our findings seem to contradict results by Fisher et al. (1998), who found that the X-ray luminosity of ARs is best correlated with their total unsigned magnetic flux. However, the latter authors dealt with active regions of the same evolutionary stages: all of them were relatively young, and spotless ARs with dispersed magnetic fields were not represented in their sample. Their results simply show that the greater the magnetic flux content of a young AR, the stonger it emits (X-ray) radiation. Studying the evolutionary aspect of emissivity after a given magnetic flux emergence provides an extension of their result. The emissivity of a given total magnetic flux shows dependence on how closely the flux is packed. Also, an evolving active region presents a case when both the total magnetic flux *and* the magnetic flux density are changing.

Recent results by Harvey and White (1999) are in good agreement with our findings and expand the wavelength range studied by us. They found that Ca II K intensity in active regions and plages is proportional to the half-power of the magnetic flux density. The

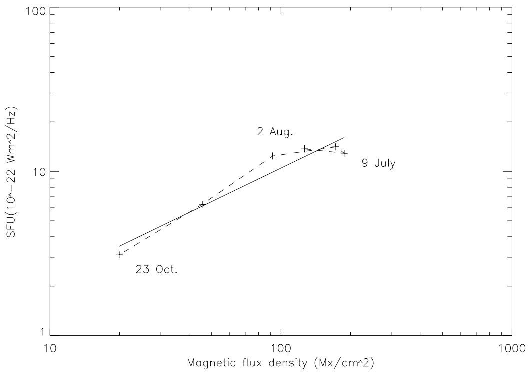

Figure 12: Log-log curve of the residual 10.7 cm radio emission (DRAO) versus magnetic flux density suggests a power law with 0.68 ± 0.10. Note that 10.7 cm radio emission is used as proxi for chromospheric activity, its brightness temperature is about 3 $10^4 K$.

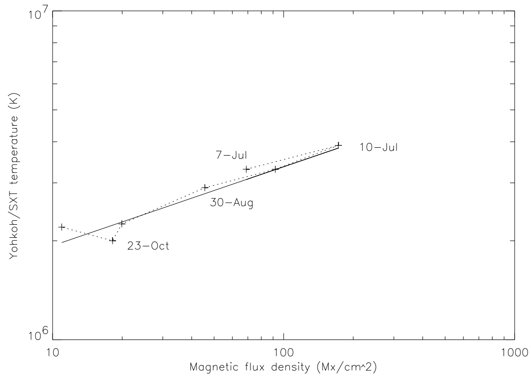

Figure 13: Log-log curve of the Yohkoh/ SXT temperature values versus magnetic flux density indicates a power of 0.24 ± 0.03, i.e. that the coronal temperature of the AR is proportional to the quarter power of the magnetic flux density.

$\mid B \mid$ vs I relation in this cool chromospheric line adds another value to the exponent list given in Table 1, and confirm our suggestion that the exponent depends on the formation temperature (or height in the atmosphere) of the emission.

The results presented above on the long-term evolution of an isolated AR confirmed the introductory sentence, i.e. that the evolution of active regions in each and every detail reflects the evolution of the magnetic field. We have already learned a lot about this AR, but there are still several unanswered questions. We saw that non-potentiality evolves in the active region and that it is related to its flare and CME activity. However, it is not yet explored how much is the contribution of the differential rotation in building up the observed shear and how much can be attributed to a continuing emergence of the twisted flux tube, which formed the AR. As for the emissivity evolution, the wavelength range of the emissivity measurements clearly need to be extended towards the chromospheric and transition-region lines, and the physics behind the discovered power-law dependences betwwen the magnetic flux density and other observables should be explored. The Sun provided us with an almost perfect subject for such evolutionary oriented studies, thus we should make the most of it.

Acknowledgements

I thank the organizers of the meeting for the wonderful "eclipse experience", a mixture of science, enchantment and fun. I thank all my collaborators, B. Thompson, C.H. Mandrini, P. Démoulin, S. Orlando, S. Plunkett, C. Bocchialini, K. Oláh, Zs. Kővári, G. Aulanier, C. DeForest, B. Schmieder, J. Khan and A. Fludra, who helped to realize this ambitious and diverse project, the Yohkoh Team and the MSSL YDAC for the Yohkoh/SXT data, and the SOHO/MDI consortium for the magnetograms. I acknowledge the usefulness of the

Instrument	Temperature	Exponent
GOES 1-8 Å soft X-rays	5-6 10^6 K	1.3 ± 0.1
Yohkoh/SXT 3-35 Å	2-4 10^6 K	1.1 ± 0.1
SUMER S VIa	2 10^5 K	0.94 ± 0.36
SUMER S VIb	2 10^5 K	0.68 ± 0.24
DRAO 10.7 cm radio	3 10^4 K	0.68 ± 0.10

Table 3: Exponents of the power-law describing the magnetic flux density – intensity relations.

Parameter	Exponent
Yohkoh/SXT emission measure	1.32 ± 0.13
Yohkoh/SXT temperature	0.24 ± 0.03

Table 4: Exponents of the power-law describing the magnetic flux density – emission measure and temperature relations.

2nd SOHO/Yohkoh CDAW held at Orsay, France, initiating this project. I acknowledge the Hungarian Government grants OTKA T-026165 and AKP 97-58 2,2.

References

Amari, T., Luciani, J.F., Aly, J.J., and Tagger, M.: 1996, ApJ, 466, L39.

Bornmann, P.L., Speich, D., Hirman, J., Matheson, L., Grubb, R., Garcia, H., Viereck, R., 1996, in Edward R. Washwell (ed.) "GOES-8 and Beyond", Proc. SPIE Vol. 2812, p. 291.

Démoulin, P., Bagalá, L.G. Mandrini, C.H., Hénoux, J.C., and Rovira, M.G.: 1997, A&A, 325, 305.

Dryer, M. and 23 co-authors: 1998, Solar Phys., 181, 159.

Fisher G.H, Longcope D.W., Metcalf T.R., Pevtsov A.A.: 1998, Ap.J., 508, 885.

Hanser, F.A., Sellers, F.B., 1996, in Edward R. Washwell (ed.) "GOES-8 and Beyond", Proc. SPIE Vol. 2812, p. 344.

Harvey, K.L., Hudson. H.S., 1997, in T. Watanabe, T. Kosugi, A.C. Sterling (eds.): "Observational Plasma Astrophysics: Five Years of Yohkoh and Beyond", Kluwer, 315.

Harvey, K.L., White, O.R., 1999, ApJ., 515, 812.

Mandrini, C.H., van Driel-Gesztelyi, L., Thompson, B., Plunkett, S., Démoulin, P., Aulanier, G., 1999, Intern. Geophys., in press

Mikič, Z. and Linker, J.A.: 1997, in "Coronal Mass Ejections", Geophysical Monograph 99, American Geophys. Union. 57.

Oláh, K., van Driel-Gesztelyi, L., Kővári, Zs., Bartus, J.: 1999, Astron. Astrophys. 344, 163.

Orlando, S., Khan, J., van Driel-Gesztelyi L., Thompson, B., Fludra, A., Foing, B., Adv. Space Res., in press
Pevtsov, A.A., Canfield, R.C., and Metcalf, T.R.: 1995, ApJ, 440, L109.
Scherrer, P.H., and 12 co-authors: 1995, Solar Phys. 162, 129.
Tapping, K.F., Charrois D.P., 1994, Solar Phys., 150, 305.
Tsuneta, S., and 12 co-authors: 1991, Solar Phys. 136, 37.
van Driel-Gesztelyi L.: 1998, in C. Alissandrakis and B. Schmieder (eds.) "Three Dimensional Structure of Solar Active Regions", ASP Conf. Ser., 155, 202.
van Driel-Gesztelyi L., Schmieder B., Aulanier, G., Démoulin, P., Martens, P.C.H., Zarro, D., De Forest C., Thompson B., Saint Cyr, C., Kucera T., Burkepile, J.T., White, O.R., Hanaoka, Y., and Nitta, N.: 1998, in D. Webb, D. Rust and B. Schmieder (eds.) "New Perspectives on Solar Prominences", Proc. IAU Coll. 167, ASP Conf. Ser., 150, 366.
van Driel-Gesztelyi L., Mandrini, C.H., Thompson, B., Plunkett, S., Aulanier, G., Démoulin, P., Schmieder, B., and DeForest, C.: 1999, Proc. 3rd ASPE, ASP Conf. Ser., 184, 302.
van Driel-Gesztelyi L., Thompson B., Démoulin, P., Orlando, S., Bocchialini K., Oláh K., Kővári, Z., DeForest, C., Khan J., Fludra A., and Mandrini C.: 1999, "Long-term evolution of the emissivity and heating in a solar active region" Proc. SOHO-8, ESA Publ. SP-446, 663.
Wilhelm, K., and 15 co-authors: 1995, Solar Phys. 162, 189.

Discussion

S. Antiochos: Does the decrease in X-ray emission with the corresponding increase in area in agree with the $I \sim L^{-2}$ result found by Pascal?

L. van Driel: The first rough calculations show that the two results are compatible. We are presently working on a more precise answer.

S. Antiochos: Was there a change in the speed of the CMEs during the evolution of the AR?

L. van Driel: During the flux emergence phase several of the CMEs which originated from this AR were fast flare-related ones , while after the disappearance of the sunspots they were mainly related to filament eruption, thus they belonged to the slow CME category. Like this we can say that in general the speed of the CMEs decreased during the long-term evolution of the AR.

S. Solanki: How large was the spatial box used to determine the total magnetic flux?

L. van Driel: The area of the spatial box was 1.6×10^{11} km^2.

S. Solanki: How does the presence of an older active region influence the estimate of the change in flux of the newly emerged active region?

L. van Driel: We see that the positive (leading) magnetic polarity of the older active region disappeared by the second rotation presumably by flux cancellation. The counterpart of the cancelling positive polarity had to mainly belong to the negative (following) polarity of the new emerging active region. Thus, the evolution of the magnetic flux of the newly emerged active region can not be regarded undisturbed at the beginning.

K. Oláh: The shape of the flux variation curve of the active region reminds me to the shape of a stellar flare though in a much longer time scale. Do you see any possible correlation between this shape and the fact that the number of flares were also decreasing as the active region decayed? Could overlapping flare events result in this kind of behaviour?

L. van Driel: The total emitted flux of the active region carries the combined effects of flaring and heating defined by the scaling laws. The remark on the flare-like shape of the flux versus time is an interesting observation and deserves further consideration.

Active region dynamics

L.K. Harra[1], S.A. Matthews[1], H. Hara[2] and K. Ichimoto[2]

[1] Mullard Space Science Laboratory, University College London, Holmbury St. Mary, Dorking, Surrey RH5 6NT, U.K.
[2] National Astronomical Observatory, Mitaka, Tokyo 181, Japan

Abstract. It has been frequently observed that in solar active regions the measured line widths are larger than those based on thermal equilibrium widths. This excess width (characterised as non-thermal velocity, V_{nt}) has been proposed as a signature of the heating mechanism. The behaviour of the V_{nt} at coronal temperatures has not produced consistent results with values ranging from 0 to 100 km/s. We investigate this problem by using joint observations from Norikura Solar Observatory, Japan and the Coronal Diagnostic Spectrometer (CDS) on SOHO. We find that values of V_{nt} range between 10 – 20 km/s. We analyse the dynamical behaviour of different temperature loops and find that for loops with Log $T_e < 5.8$, the variability $\propto T_e^{0.39}$. This is comparable to the dependence of non-thermal velocity on temperature which we have determined to be $V_{nt} \propto T_e^{0.35}$. This suggests that the excess line broadening is caused by highly dynamical behaviour in the transition region for active regions. These results have significant implications for potential heating mechanisms and these are discussed.

1. Introduction

It is well observed that in flaring and non-flaring active regions the line widths are found to be in excess of the thermal width. This excess width has been termed *non-thermal velocity* (V_{nt}) and it is thought to be an indicator of the coronal heating mechanism. Transition region observations in both active regions and the quiet Sun (e.g. Boland et al. 1975, Doschek et al. 1976 and Mariska et al. 1978) show that the non-thermal velocity

(V_{nt}) increases with increasing temperature ($V_{nt} \propto T_e^{1/4}$ for $\log T_e < 5.8$). This behaviour is predicted from an Alfvén or acoustic wave propagating without energy dissipation.

However as coronal temperatures are reached the relationship becomes less clear. For coronal active region observations a wide range of values of V_{nt} (10–100 km/s) have been derived for temperatures ranging between 1–6.2 MK. Although the dependence of V_{nt} with temperature below $\log T_e = 5.8$ has been verified, the behaviour above $\log T_e > 5.8$ is still not well understood. One of the assumptions that is generally made in the case of active regions is to assume that there is no temperature gradient and the active region is isothermal.

Another possibility to explain the excess line broadening is that there are multi-directional Doppler flows which could be a result of the superposition of flows in many magnetic flux tubes which are not spatially resolved. In active regions it has been found that cool transition region loops coexist with hot coronal loops (e.g. Orall 1981, Matthews and Harra-Murnion 1997). These various observations dictate that caution has to be used in assuming a link between the transition region emission and its relation to the coronal emission.

Different temperature loops in active regions have been found to show very different characteristics. The transition region cool loops (< 1 MK) are in general more dynamic than the hotter loops (> 1 MK). If this is the case then the dependence of V_{nt} with temperature in active regions may be due to the different classes of loops which exist, and cannot be due to a wave which travels through the different temperature layers.

In this paper, we determine the values of V_{nt} in an active region without assuming that the region is isothermal in the radial direction. This is achieved by making use of the temperature diagnostic and spatial information available from the Coronal Diagnostic Spectrometer (CDS), and the measurements of the line widths from the Norikura Solar Observatory. We investigate the behaviour of different temperatures loops and relate this to the dependence of V_{nt} with temperature.

2. Observations

For the calculation of the V_{nt} at coronal temperatures we employed data from an observing campaign which took place from the 23 August – 31 August 1997 using the 25 cm coronagraph at the Norikura Solar Observatory and the CDS. CDS observed in a variety of lines enabling us to calculate the spatial distribution of temperatures. The Norikura spectrograph provides high resolution spectral imaging data in the Fe XIV 5303 Å line which provides accurate line widths. Combining CDS and Norikura observations permits the determination of V_{nt} without assuming a single fixed temperature throughout the active region.

For the determination of the dynamical behaviour of loops as a function of temperature the CDS was used. A time sequence was carried out on 17th Jan 1998, which covered lines formed over a range of temperatures from the cool transition region to the hot corona.

3. Non-thermal velocity of coronal loops

The non-thermal velocity was derived from the temperature obtained from CDS and the line widths from Norikura coronagraph. Non-thermal velocity is defined as $V_{nt}= [2k(T_D - T_e)/m_i]^{1/2}$, where T_D is the Doppler temperature derived from the total observed line width, T_e is the electron temperature obtained from line ratio diagnostics and m_i is the mass of the ion considered. In all cases the total width of the lines (T_D) is larger than the thermal width as calculated from the electron temperature.

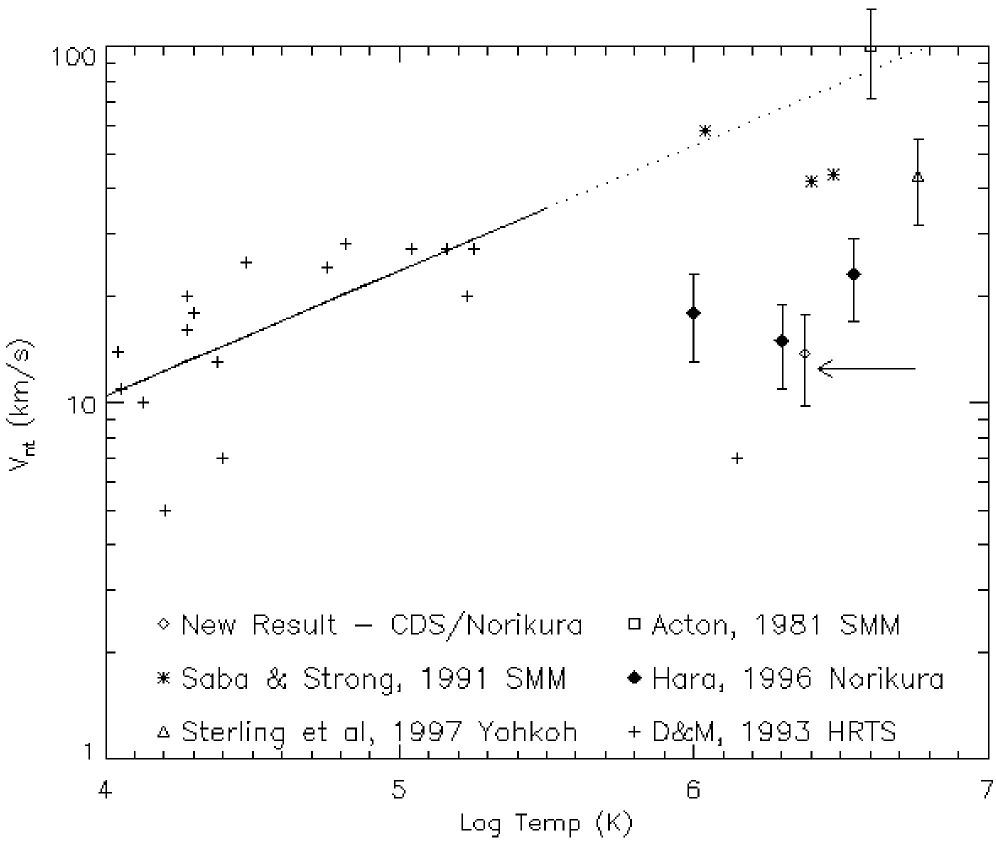

Figure 1: This plot illustrates the variation of V_{nt} with temperature. Values of V_{nt} from previous observations are shown alongwith our new result (indicated with an arrow). The errors from this result are derived from fitting the histogram of the spread of non-thermal velocities derived over the overlapping region of the Norikura and CDS FOV and deriving the FWHM of the spread of V_{nt}.

Fig. 1 illustrates the variation of the line broadening with temperature. The temperature plot shows data from previous observations alongwith our derived value. The behaviour below $\log T_e = 5.7$ has been shown many times to increase with increasing temperature. However as temperatures above $\log T_e = 6$ are reached, the relationship becomes less clear with a wide range of values being derived. Our averaged data shows a magnitude of V_{nt} = 13.8±1.2 km/s which is lower than previously calculated, suggesting that the V_{nt} reaches a maximum and starts to decrease as coronal temperatures are reached. The

V_{nt} value decreases when the assumption that the temperature is isothermal in the radial direction is removed. This is true for active regions at $\log T_e \approx 6.4$. Dmitruk, Gomez and DeLuca (1998) have carried out numercial simulations of an externally driven 2-D magnetohydrodynamic (MHD) system to model the dynamics of a coronal loop. Their derived value of V_{nt} is 16 km/s which is consistent with our results. They suggest that the larger values of V_{nt} observed by Saba and Strong (1991) correspond to hotter and larger active regions. Our observations could only be carried out for $\log T_e \approx 6.4$. Above this temperature, it is possible that the V_{nt} values may start to increase again. A large statistical study would be have to be carried out to determine whether the higher values derived at higher temperatures are due to poor (or no) spatial resolution, assumption of radial isothermality, or magnetically complex regions.

It has been well observed (e.g. Kjeldseth-Moe and Brekke 1998) that high-lying loops with temperatures below $\log T = 5.8$ are much more dynamic and unstable than loops with $\log T > 6$. This is expected since this particualr class of high-lying cool loops have heights which are larger than the scale heights predicted from their temperatures. In the next section we investigate the dynamical behaviour of active region loops at different temperatures and relate this to the dependence of V_{nt} with temperature.

4. Loop dynamics

As mentioned in the introduction it is now well observed that not only do cool (< 1 MK) loops exist, but they are also more dynamic than their hotter counterparts. In this section we quantify how dynamic the behaviour is in each temperature regime. No previous attempt has been made to directly relate the dynamical behaviour of loops with $\log T_e < 5.8$ to temperature.

To achieve this, a CDS time series sequence (EPHAR_4 s10267) was carried out on the 17 Jan 1998 at a small active region on the limb in order to quantify the dynamics of the different temperature loops. Fig. 2 shows sample images in the OV and Mg X lines over a period of ≈ 5 hours with a cadence of ≈ 7 mins. As expected the OV loop shows rapid changes, whereas the Mg X loop stays relatively static.

To demonstrate the changes in the structures with time, the correlation (linear Pearson correlation coeffient, r) of each image relative to the first image observed has been calculated , where x is the intensity in the x direction and y is the intensity along the slit, where r=1 defines a complete positive correlation and r=0 defines no correlation. The correlation decreases with time for both the hot (Mg X) and the cool (O V) loops – however the O V loop fluctuates greatly. This behaviour has been observed in many active region studies with CDS. The variability is defined as the standard deviation (σ) of the derivative of the correlation with respect to time ($\sigma(dr/dt)$). Fig. 3 shows the variability with temperature. This provides a measurement of how much the loop structure varies in the different temperature loops.

The behaviour of the variability with temperature is similar to the behaviour of the line broadening with temperature (Fig. 1). Both relationships are linear with *variability* $\propto T_e^{0.39}$ and $V_{nt} \propto T_e^{0.35}$. Below $\log T_e = 5.8$, both the variability and the V_{nt} show positive

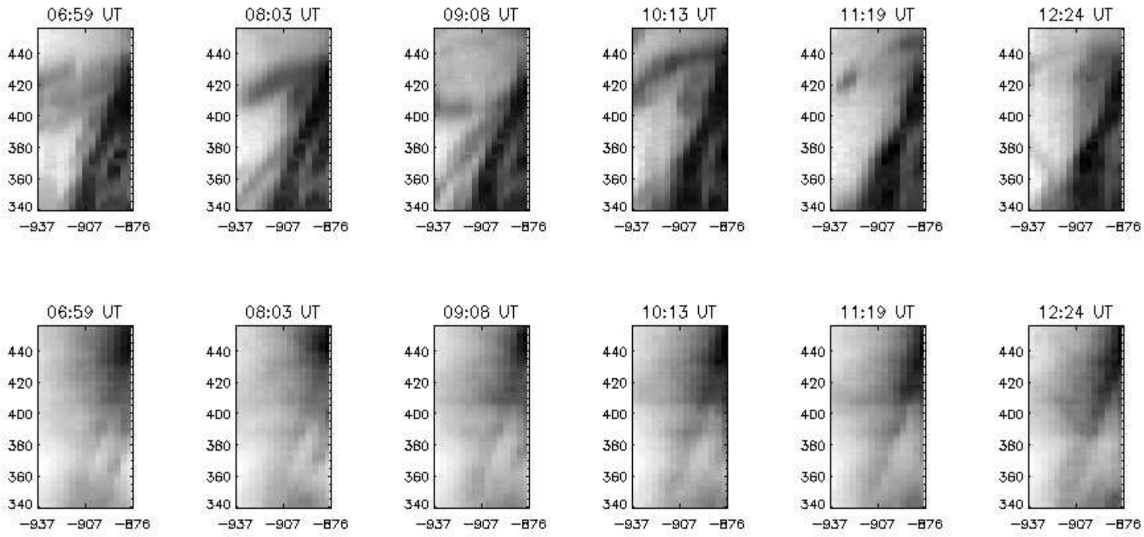

Figure 2: A time series of images in the O V line (top) and Mg X line (bottom). The scale is in arcsecs. The OV images show frequent changes in loops brightening and disappearing. The Mg X structure remain relatively stable throughout the time series.

gradients of approximately the same value suggesting that the line broadening is due to multi-directional flows. Consequently, the heating mechanism for the cool loops must be a transient, random mechanism, which produces flows in all directions.

5. Discussion

The behaviour of line broadening in the active region corona is not well understood. Making use of the diagnostic capabilities of CDS along with the accurate line widths from the Norikura Solar Observatory, Japan, we have been able to measure the non-thermal velocities accurately without assuming that the active region is isothermal throughout the loop structures. The results indicate that there is a distinct change in the behaviour of V_{nt} with temperature as coronal temperatures are reached. As coronal values are reached the V_{nt} does not continue to increase with temperature, but decreases dramatically, which is consistent with some previous observations. The values we have derived are consistent with values determined by Dmitruk, Gomez and DeLuca (1998) using 2D MHD simulations. They also expect V_{nt} to increase with increasing temperature for coronal loops. In Fig. 1 for $\log T_e > 6.4$, there is a trend for V_{nt} to increase with increasing temperature. However, this would need to be clarified by carrying out a large statistical study over a wide range of different temperature active regions using a range of different coronal lines for analysis.

There are two options to explain the dynamic cold loops. The first is that they exist as a progressive stage to the hotter loops and secondly that they are entirely separate entities. Both of these options are discussed in the following subsections in light of our results.

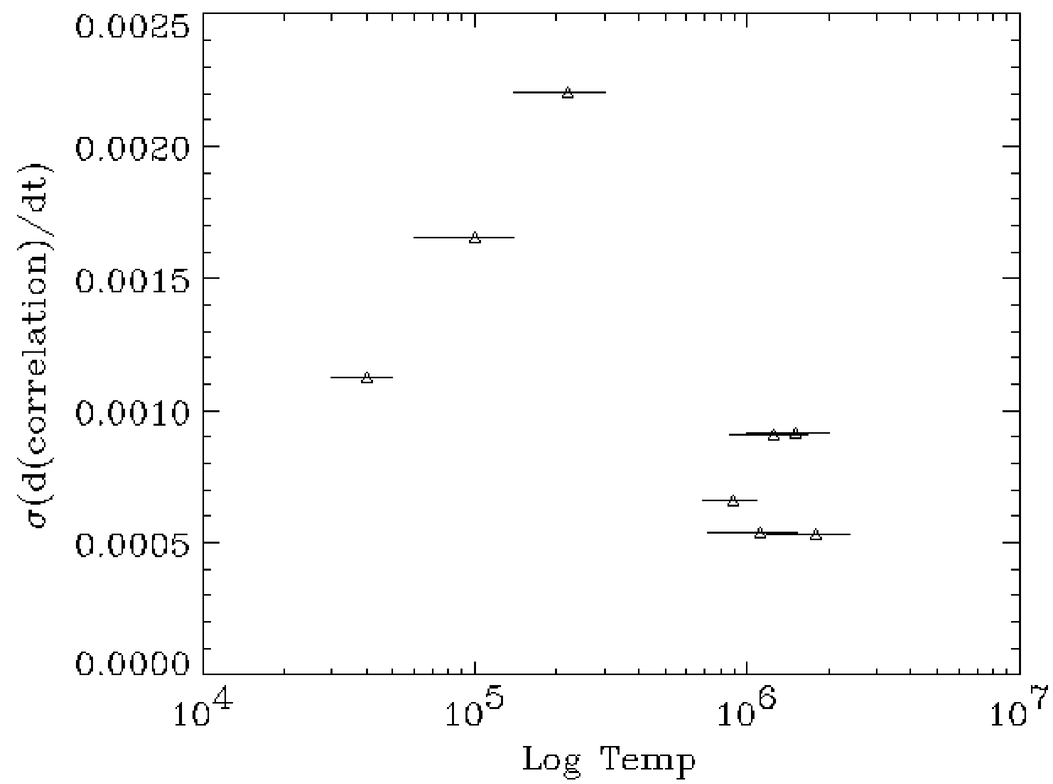

Figure 3: The time variability ($\sigma(dr/dt)$) of the different temperature loops.

6. Conclusion

In summary we found that the value of the V_{nt} at around 2 MK ranges between 10 – 20 km/s. This value was determined by using temperature diagnostics rather than assuming an electron temperature. This confirms that V_{nt} does not continue to increase with temperature beyond 1 MK, but decreases from 40 km/s at $\log T_e = 5.6$ to 15 km/s at $\log T_e = 6.3$. There is some evidence in other work that above $\log T_e = 6.6$ (see Fig. 1), that the V_{nt} starts to increase again with temperature.

With the recent observations from SOHO confirming the existence of cool transition region loops, we investigated the relationship that the behaviour of these loops have to the V_{nt} values. We can no longer assume that the transition region emission in active regions is a transitional layer between the surface and the hot coronal loops. We investigated one of the properties which would most likely affect the line widths - the dynamics of the different temperature loop systems. We found similar relationships between the variability and V_{nt} as a function of temperature ($\log T_e < 5.8$). This suggests that the V_{nt} is due to multiple Doppler flows which are superimposed. Above 1 MK the relationship was not as clear. It is possible that since there is no relationship between the variability and V_{nt} that a different heating mechanism exists. However there were a limited number of data points to confirm this.

Acknowledgements

LKHM and SAM would like to thank PPARC for postdoctoral funding. We are grateful to the referee for improving the clarity of the paper.

References

Boland, B.C., et al, 1975, MNRAS, 171, 697.

Dmitruk, P., Gomez, D.O., DeLuca, E.E., 1998, ApJ, 505, 974.

Doschek, G.A., Feldman, U., VanHoosier, M.E., and Bartoe, J.D.F., 1976, ApJS, 31, 417.

Kjeldseth-Moe, O., and Brekke, P., 1998, Solar Phys., accepted.

Mariska, J.T., Feldman, U. & Doschek, G.A., 1978, ApJ, 226, 698

Matthews, S.A. and Harra-Murnion, L.K., 1997, Solar Phys, 175, 541-551.

Orall, F.Q., 1981, 'A Monograph from Skylab Solar Workshop III', Colorado Associated University Press

Saba, J.L.R and Strong, K.T., 1991, ApJ, 375, 789

Discussion

S. Solanki: Did you determine the correlation coefficient over the whole CDs "image", or just over the off-limb part?

L. Harra: The correlation coefficient is determined just over the off-limb part of the active region.

S. Antiochos: Could it be that the observed T dependence of the Vnt is due to the cooling of hot loops?

L. Harra: What is clear is that there is some relationship between the cool and hot loops. Whether it is that the cool loops are dynamic enough and produce enough energy to heat the corona, or whether the hot loops are cooling down is hard to ascertain from the observations. The cooling times of the coronal loops have been measured and are too long to explain the cool loops.

The relation between hot and cool loops

N.V. Nitta

Lockheed Martin Solar and Astrophysics Laboratory,
O/L9-41, B/252, Palo Alto, CA 94304, U.S.A.

Abstract. In order to trace the origin of the hot ($\gtrsim$ 2.5 MK) corona above active regions, we compare images from *Yohkoh*/SXT and TRACE. A typical SXT snapshot of an active region shows the bright core surrounded by diffuse emission. In time sequence SXT images, bright X-ray structures easily recognized as loops are often found to follow minor brightenings and to undergo structural changes on time scales that can be shorter than the expected cooling times. These loops do not show up in TRACE coronal images before, during or after they are seen in SXT images, indicating their origin to be different from 1-2 MK loops. The data suggest that heating and cooling of the diffuse loops may occur dynamically.

1. Introduction

From space-bourne observations, it has been known for three decades that the solar corona is structured into closed loops, which are believed to delineate magnetic field lines. How these loops are heated is still a mystery, even though various types of theory have been proposed. A serious ambiguity on testing theory against observations comes from the multi-thermal nature of the corona, as obvious from images that are taken by instruments with different temperature sensitivities (e.g., Yoshida et al. 1995; Di Matteo et al.). The hot ($T \gtrsim$2.5 MK) corona appears quite different from the cooler ($T \sim$1 MK) corona. Does the cooler emission represent only the bases of hot loops and their transient (heating or cooling) states, or do cool loops exist on their own? If the latter is the case, theory must explain the heating of both hot and cool loops. Therefore it is important to study the spatial and temporal relationships between hot and cool loops, by analyzing images with different temperature sensitivities over times that are longer than the life times of the loops.

In this paper, we compare images from the *Yohkoh* Soft X-ray Telescope (SXT; Tsuneta et al. 1991) with those from TRACE (Handy et al. 1999). The initial results from TRACE can be found in Golub et al. (1999) and Schrijver et al. (1999). Besides the higher spatial resolution, a major advantage of TRACE over the Extreme-Ultraviolet Imaging Telescope (EIT; Delaboudinière et al. 1995) on the *Solar Heliospheric Observatory* (*SOHO*) is the availability of images in multiple EUV wavelengths at a good cadence. EIT observations normally concentrate on one wavelength (typically 195 Å), taking images in other channels only four times a day. As we see in Section 3, the temperature response of the TRACE 284 Å channel somewhat overlaps that of SXT compared with other channels. The 284 Å images, not extensively analyzed up to now, may be important for understanding the different appearances of the corona in SXT and TRACE 171 Å/195 Å images.

2. High-temperature loops

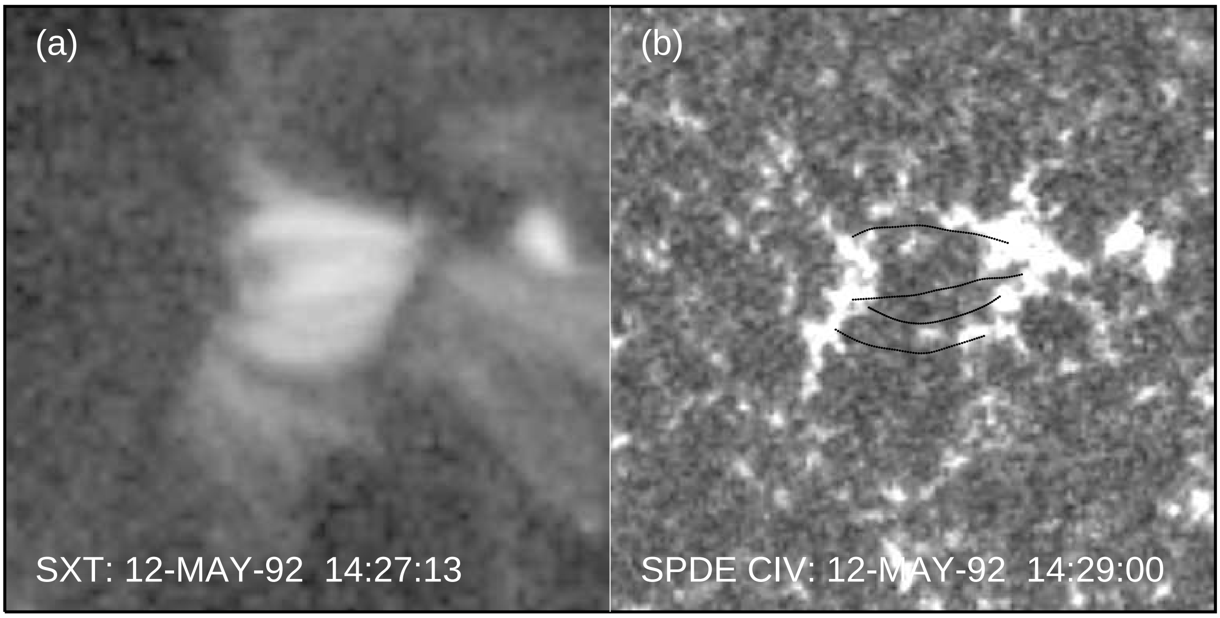

Figure 1: (a) Example of well-defined but steady loops in an SXT image. The loops are traced, and overplotted on a UV image that includes the C IV doublet at 1550 Å, as shown in (b). They appear to anchor at areas that are bright in the UV image.

Steady or quasi-steady loops in SXT images have been extensively studied (e.g., Porter & Klimchuk 1995; Kano & Tsuneta 1996) and their heating and cooling have been discussed in terms of simple models that put the measurements in the context of the well-known scaling law (Rosner, Tucker, & Vaiana 1978). An example of such loops is given in Figure 1(a), in which individual loops are readily recognizable. Their bases seem to be on bright patches in a broadband UV image (Figure 1(b)) from the Solar Plasma Diagnostic Experiment (SPDE) rocket payload (Damé et al. 1996) that includes the C IV doublet at 1550 Å. The bright areas in the UV image is considered to be due to heat conduction from the upper part of the loops. Based on a quick look at SXT time sequence images, these loops existed without significant changes for a few hours. We need to make some assumptions as to their geometry, however, to estimate how long these loops are (an important parameter for the scaling law), because we do not know how much they are inclined with respect to the vertical (c.f., Nitta, van Driel-Gesztelyi, & Harra-Murnion 1999).

We looked for steady and clearly defined loops in 15 active regions that had reasonably good TRACE 284 Å coverage between June 1998 and June 1999. We found that there were not many clearly defined loops in these regions. Most of these loops showed high or decreasing brightness. This indicates that these loops were preceded by small flarings that might have been identified with so-called transient brightenings (Shimizu et al. 1992). Indeed, it turns out that some of the loops studied by Kano & Tsuneta (1996) show significant variations in the X-ray intensity and even structural changes during the intervals of a few hours. Given longer decay times than rise times of the brightenings, it is likely that at least some SXT loops correspond to "postflare" loops of transient brightenings that happened during data gaps.

As in an example shown in Section 4, an active region often consists of a bright core, which appears to be due to occasional brightenings, surrounded by diffuse and fainter emission, which probably represents unidentifiable loops. Because we cannot easily trace the loops, it is hard to locate their bases. We will come back to these diffuse loops in Section 5.

3. Response

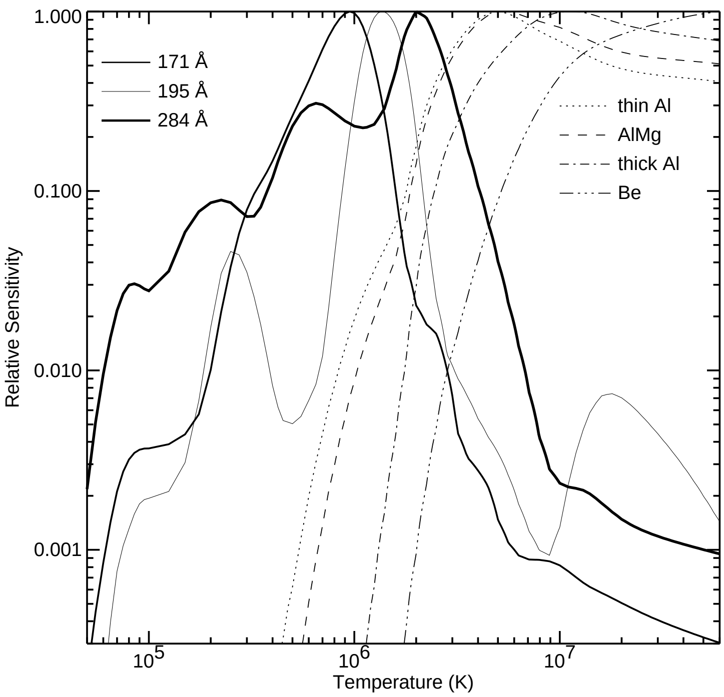

Figure 2: Comparison of normalized responses of SXT and TRACE with temperature.

In Figure 2, we compare the responses with temperature of SXT and TRACE in different filters and channels. As well known for the difference between grazing incidence and normal incidence telescopes, SXT has broader and less peaked responses than TRACE. The plot also confirms that SXT, even in the thinnest (thin aluminum or Al 1265 Å) filter, is more sensitive to hot plasma than all the coronal channels of TRACE. The 284 Å channel is closest to SXT, and its overlap with SXT may depend on the amount of (2.5–3) MK plasma relative to $\sim$2 MK plasma along the line of sight. The 284 Å channel has substantial sensitivities to temperature below 1 MK. The 195 Å channel has enhanced sensitivity above 10 MK, but it is not relevant for usual active region loops. The different appearance of the solar corona in SXT and TRACE (or EIT) images comes from these different responses with temperature.

4. Coalignment of SXT and TRACE images

In Figure 3, we show what we believe to be coaligned SXT and TRACE 171 Å images of an active region (AR 8518). As of September 1999, we could not automatically coalign these images because the pointing information for either instrument appeared to be not consistent. Therefore, we used an EIT (195 Å) full-disk image taken close in time, with which both an SXT full-disk image and a TRACE 195 Å image were coaligned by matching various features. Relative offsets among TRACE images in different wavelenghts are well understood.

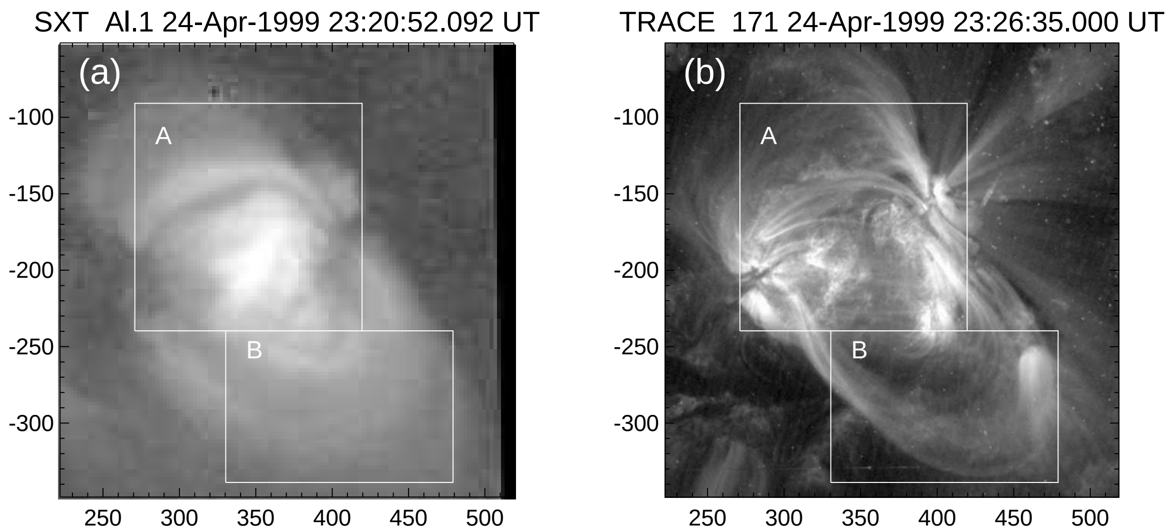

Figure 3: SXT and TRACE 171 Å images of AR 8518. Sub-regions A and B are expanded in Figures 4 and 5. The coordinates are in arcseconds from disk center.

In the course of this exercise, we also confirmed that the pixel sizes of these three instruments are consistent with the official values; 2.62″ for EIT (uncorrected for the fact that *SOHO* is orbiting around the L1 point), 2.46″ for SXT and 0.50″ for TRACE. There is a plan of generating a new pointing database for TRACE images within SolarSoftware,

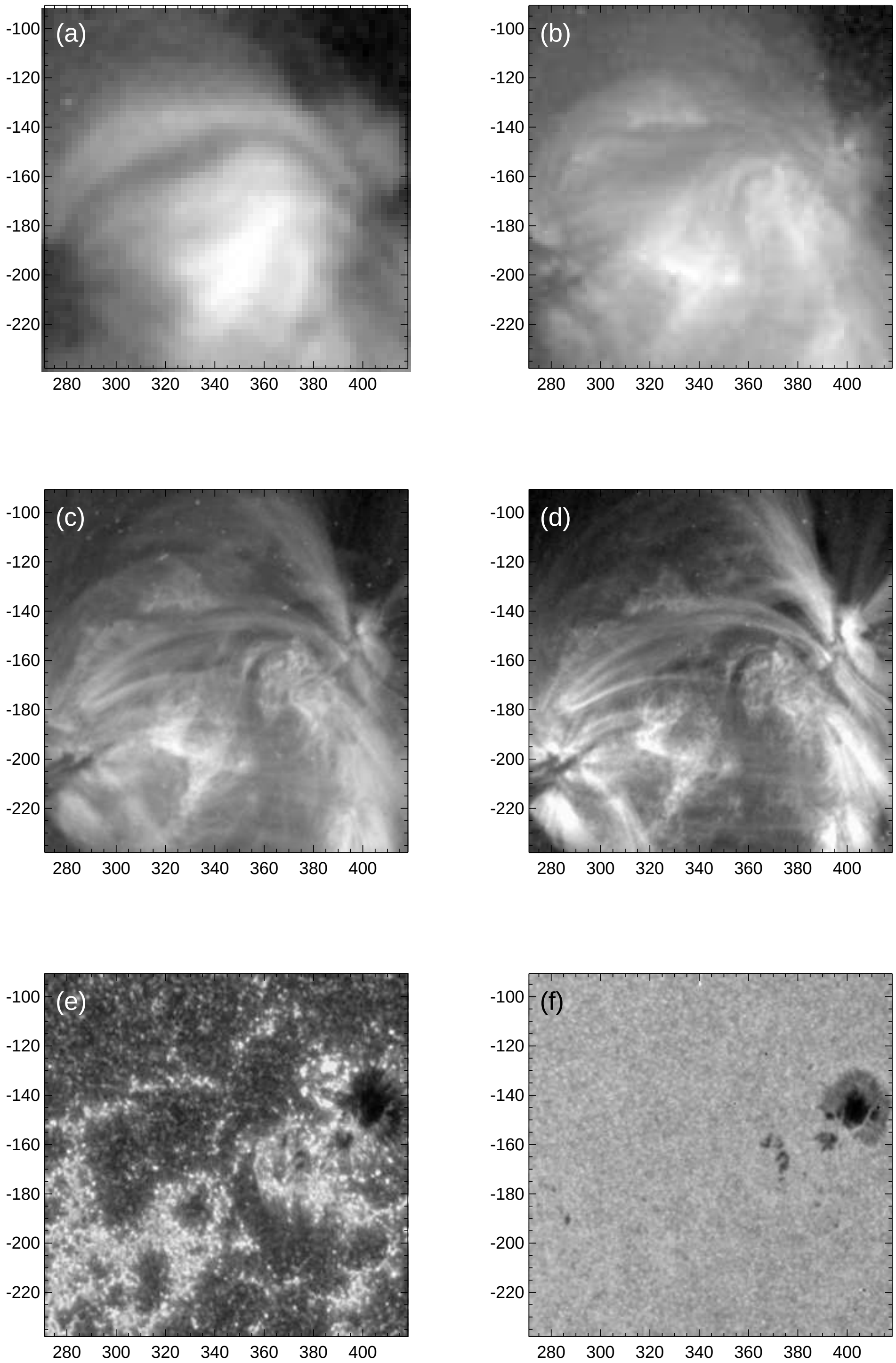

Figure 4: Images of sub-region A. (a) SXT thin Al filter (23:20:52 UT), (b) TRACE 284 Å (23:26:09 UT), (c) TRACE 195 Å (23:27:07 UT), (d) TRACE 171 Å (23:26:35 UT), (e) TRACE 1600 Å (23:25:30 UT), and (f) TRACE white-light (23:25:34 UT).

on the basis of cross correlations with EIT images taken close in time (Freeland 1999, private communication).

5. Comparisons of SXT and TRACE images

The SXT image in Figure 3 shows that the region consisted of the bright central part and the surrounding part of diffuse emission. Although the SXT and TRACE images have different bright regions, the overall shape of the active region in these images is quite similar. We make closer comparisons of two areas as indicated in Figure 3.

Figure 4 replicates the images in Figure 3 extracted and blown up for sub-region A, together with TRACE images in other channels, taken between 23:20 UT and 23:30 UT. The western legs of the bright SXT loops seem to be anchored at small pores to the southeast of the main spot (Figure 4(f)). These loops are not seen even in the 284 Å image, in which the bright patches appear to represent their bases, as in the 195 Å and 171 Å images. Part of these patches may be regarded as "moss" (Berger et al. 1999; Fletcher & De Pontieu 1999), which is likely to be low-lying structures at the base of high-pressure loops (Peres, Reale, & Golub 1994). Concerning the larger loop structure to the north, its appearance is similar but not quite the same in the SXT and 284 Å images. Note that moss in the 171 Å image (Figure 4(d)) exists even under the middle of this loop structure. The 195 Å and 171 Å images reveal different E-W loops, probably lower in height. These images also show legs of a few large-scale loops, including the one that emanates from the main sunspot (c.f., Schrijver et al. 1999), which never show up in SXT images. The bases or footpoints of all these loops seem to be bright in the 1600 Å broadband image.

Images of the southern part (sub-region B) are shown in Figure 5. This completely spot-free area (Figure 5(f)) is characterized by diffuse emission in the SXT image. It probably represents ensemble of low density loops or loops with small filling factor. Its appearance is quite different in images of Figures 5(a)–(d). Bright areas do exist in the 1600 Å image, which appear to be associated with the 171 Å moss. However, we cannot tell whether there are shorter loops beneath the diffuse emission in the SXT image, whose bases may match the moss. More detailed study of the moss may shed light on the issue of the filling factor of the SXT loops (Porter & Klimchuk 1995).

6. Evolution of loops

According to the SXT time sequence images, the central part of AR 8518 repeatedly brightened, but the bright loops of Figure 4(a) (not as readily recognizable as those in Figure 1) were formed between 22:24 UT and 23:18 UT. The time of their disappearance is not known due to a long (∼2 hours) data gap, but based on the past activity the loops seen in the images of 25 April 01:25 UT were probably different ones. In Figure 6, we show TRACE time sequence images of the central part of the region (approximately matching sub-region A) over three hours. We do not identify the bright loops in any of

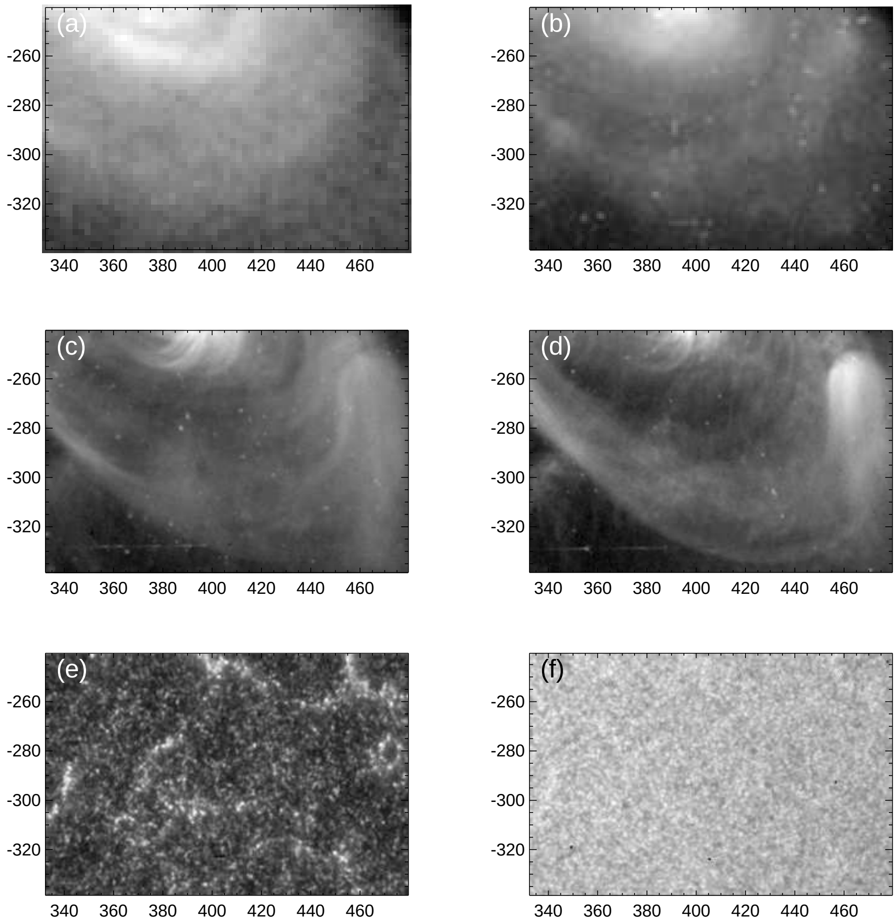

Figure 5: Images of sub-region B. The image types are same as Figure 4.

these images. This is also further confirmed in the high cadence (30–40 s) movie in the 171 Å channel.

The changes of the southern part of the region seemed to be slower. For example, the diffuse loops in SXT images became brighter over a few hours. Figure 7 compares SXT images with TRACE 284 Å and 171 Å images during the period of increasing brightness. At the same time, the volume filled with hot plasma was increasing. But the corresponding or underlying loop structure in TRACE 171 Å images appeared to shrink. This can be more readily seen in a movie representation. In the northern part of the region, another set of loops (including those in Figures 4(a)–(d) north of the bright SXT loops) were also found to be in motion, as studied by Priest & Schrijver (1999). These observations indicate that heating and cooling of loops can take place dynamically (c.f., Wang et al. 1997).

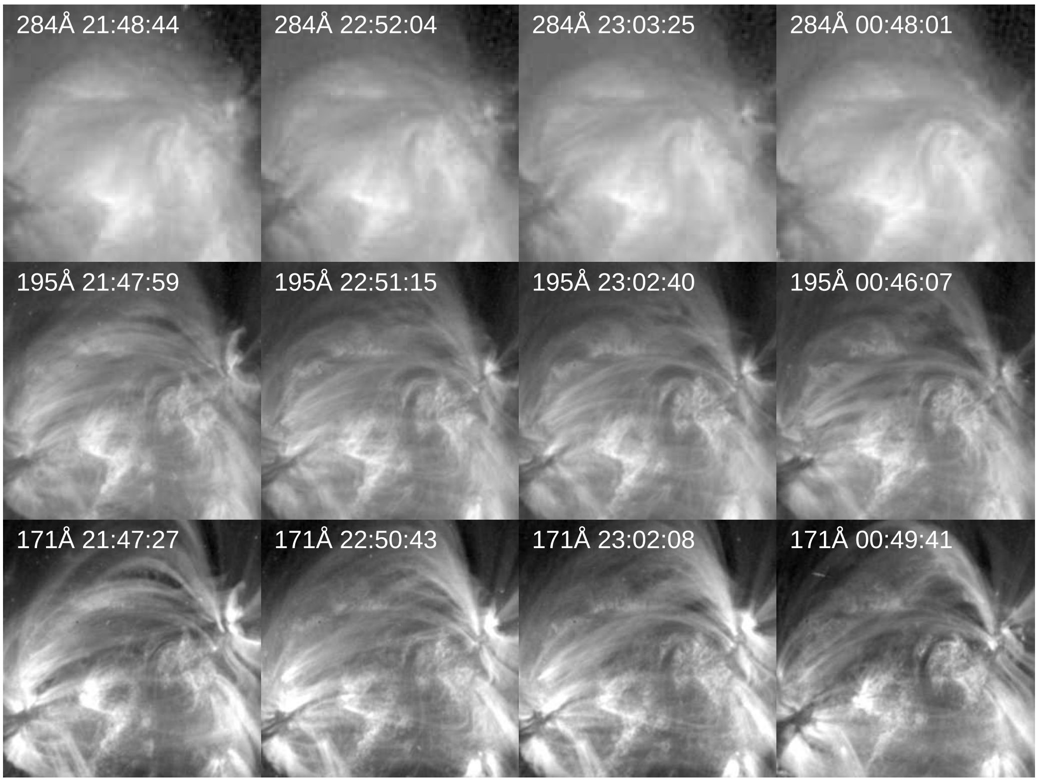

Figure 6: TRACE 284 Å, 195 Å, and 171 Å images (from top to bottom) of the central part of AR 8518. No counterparts of the bright SXT loops in Figure 4 are found.

7. Discussion

In spite of the fact that SXT and EIT have been operational for more than eight years and 3.5 years, respectively, there has not been much work (but see Nagata 2000) to discuss the relation between the $\gtrsim$2.5 MK and (1-2) MK coronae or coronal loops including their temporal variations. Our study presented more observational evidence that hot and cool loops are physically independent, which was recently discussed by Aschwanden et al. (1999) and Lenz et al. (1999) in terms of the much smaller conductive loss in cool loops than the radiative loss, indicating that they are not in steady state.

We found to our surprise that a clearly defined SXT loop tends to be not steady, often observed while it is becoming fainter. This implies that the loop corresponds to the post flare loop of a small flare or transient brightening (Shimizu et al. 1992), whose (fast) rise may not be observed by SXT. If the SXT loop results from large-scale magnetic reconnection as does a flare, according to many investigators, the same loop may not have to be seen *earlier* at lower temperatures. The reason we do not see the loop *later* may indicate that heating is turned off relatively early. If we consider a flare-like heating scenario in terms of the temperature-density diagram (Jakimiec et al. 1992; Brown 1996), the temperature rises first, followed by an increase in density due to chromospheric evaporation provided the heat input continues. Then the steady state is established, and the loop will be found to follow the scaling law (Rosner, Tucker, & Vaiana 1978). However, without the sustained heat input, the loop may cool down quickly to be invisible even to TRACE.

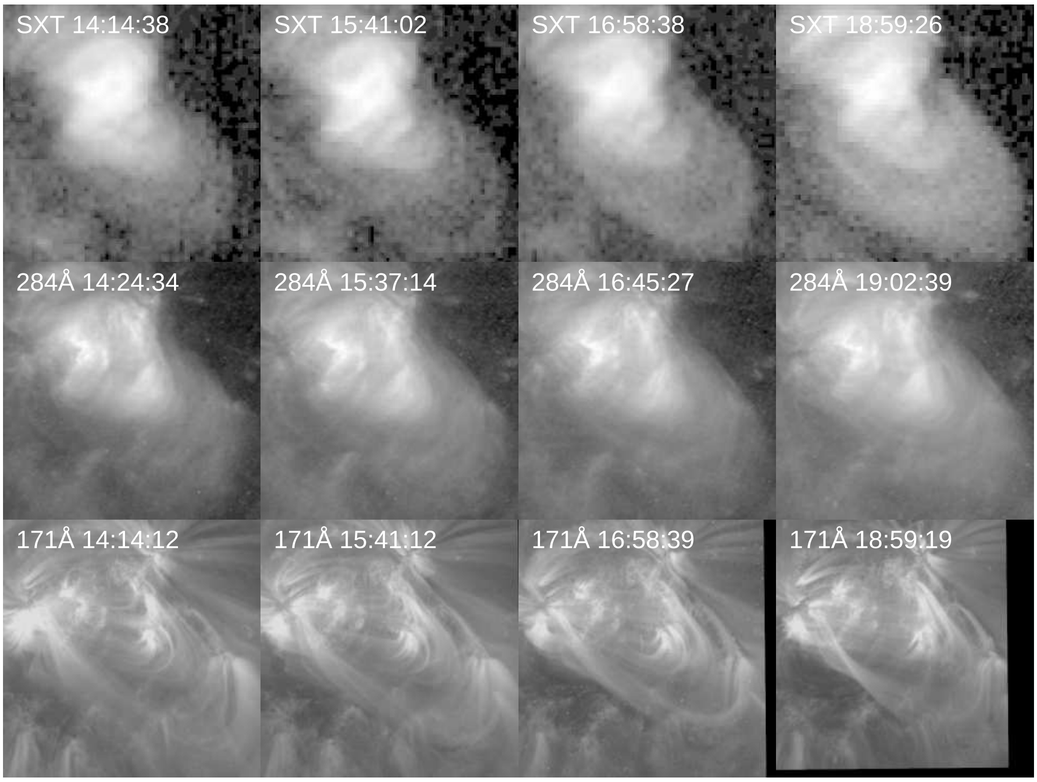

Figure 7: SXT thin Al, TRACE 284 Å, and 171 Å images (from top to bottom) of the southern part of the region (field of view of $2.5' \times 2.5'$), while the SXT diffuse loops were gradually brightening.

The flare origin of the active region loop was indeed suggested in a high temperature region cospatial with a mini cusp as discovered by Yoshida & Tsuneta (1996).

Acknowledgements

The work by NVN has been supported by NASA contract NAS 8-40801. The author is grateful to the organizers of the workshop "The Sun and Sun-like stars" for their hospitality.

References

Aschwanden, M.J., Newmark, J.S., Delaboudinière, J.-P., Neupert, W.M., Klimchuk, J.A., Gary, G.A., Portier-Fozzani, F., & Zucker, A. 1999, ApJ, 515, 842

Berger, T.E., De Pontieu, B., Schrijver, C.J., & Title, A.M. 1999, ApJ, 519, L97

Brown, S.F. 1996, A&A, 305, 649

Damé, L., Martić, Brown, W.A., Bruner, M.E., Strong, K., Suematsu, Y., Tsuneta, S., and Schmieder, B. 1996, Adv. Space Res., 17 (4/5), 189

Delaboudinière, J.-P. et al. 1995, Sol. Phys. 162, 291
Di Matteo, V., Reale, F., Peres, G., & Golub, L. 1999, A&A, 342, 563
Fletcher, L. & De Pontieu, B. 1999, ApJ, 520, L135
Freeland, S.L. & Handy, B.N. 1998, Sol. Phys., 182, 497
Golub, L. et al. 1999, Phys. of Plasma, 6, 2205
Handy, B.N. et al. 1999, Sol. Phys., 187, 229
Jakimiec, J., Sylwester, B., Sylwester, J., Serio, S., Peres, G., & Reale, F. 1992, A&A, 253, 269
Kano, R. & Tsuneta, S. 1996, PASJ, 48, 535
Lenz, D.D., Deluca, E.E., Golub, L., Rosner, R., & Bookbinder, J.A. 1999, ApJ, 517, L155
Nagata, S. 2000, PhD thesis, Univ. Tokyo
Nitta, N., van Driel-Gesztelyi, L., & Harra-Murnion, L.K. 1999, Sol. Phys., 189, 181
Peres, G., Reale, F., & Golub, L. 1994, ApJ, 422, 412
Porter, L.J. & Klimchuk, J.A. 1995, ApJ, 454, 499
Priest, E.R. & Schrijver, C.J. 1999, Sol. Phys., in press
Rosner, R., Tucker, W.H., & Vaiana, G.S. 1978, ApJ, 220, 643
Schrijver, C.J. et al. 1999, Sol. Phys., 187, 261
Shimizu, T., Tsuneta, S., Acton, L.W., Lemen, J.R., & Uchida, Y. 1992, PASJ, 44, L147
Tsuneta, S. et al. 1991, Sol. Phys., 136, 37
Wang, J., Shibata, K., Nitta, N., Slater, G.L., Savy, S., & Ogawara, Y. 1996, ApJ, 478, L41
Yoshida, T., Tsuneta, S., Golub, L., & Strong, K. 1995, PASJ, 47, L15
Yoshida, T. & Tsuneta, S. 1996, ApJ, 459, 342

Discussion

S. Antiochos: Isn't the "moss" observed by TRACE the footprints of the SXT loops?

N. Nitta: First of all, the same feature was already identified by previous observations including NIXT and EIT. TRACE revealed it very clearly. Yes, it is almost always associated with X-ray emission with a wide range of intensity and concentration, but I personally consider it difficult to say that it is located at the footpoints of X-ray loops. The reason is partly that the ends of SXT loops should be considerably higher than the real footpoints and more importantly that individual loops are not recognized where X-ray emission is diffuse.

P. Démoulin: An increase in coronal heating induces an increase in the loop density (through chromospeheric evaporation) more dramatically than an increase in the maximum temperature (and temperature in most of the loop): It is then difficult to bring a "TRACE loop" to a YOHKOH loop.

N. Nitta: Although I am not completely sure how much truth the so-called scaling law tells us (given huge uncertainty in the measured temperature and length), the density of a steady loop is proportional to square of the temperature. Therefore, to bring a 1 MK loop to 4 MK, one needs to provide 16 times as much mass. This will happen only in non-steady state, e.g., in a flare-like heating. The loop's repsonse to such a heating is well described in a T-N diagram. When the heat input goes back to the level of steady heating, the loop will cool very fast, and it may stay the TRACE temperature range only for a short time. This is probably why we do not see the cooled SXT loop in TRACE images.

Summary:
The Sun, the stars, and total eclipses

K.D. Leka

Colorado Research Associates/NWRA
3380 Mitchell Ln., Boulder, CO, USA

Abstract. This diverse group of scientists has traveled from around the globe on the event of a total solar eclipse over Szombathely, Hungary to experience a most bedazzling spectacle. With this gathering we take the opportunity to examine new results in solar physics and in the physics of Sun-like stars. In this summary I will highlight pervasive themes and connections which emerged in the talks and posters presented.

This meeting is being held on the occasion of a total solar eclipse - a relatively rare and beautiful event, and one for which a gathering to try and understand aspects of solar physics is appropriate. Still, the Sun is a star, very similar to numerous other stars we can observe, albeit as point sources only. It is constructive for solar physicists to remember the Sun's place in the rest of the Universe, and for stellar astronomers to take advantage of knowledge gained by studying one particular star whose surface can be resolved. Of course any gathering of researchers from such diverse backgrounds quickly becomes instructional in a more mundane way ("Gould Belt"? "Prominence Barbs"?), as we are all forced to define (and defend!) our jargon across both disciplines and languages.

Highlights of the talks and posters (in the humble opinion of this solar astronomer) begin with observations of stellar (hence solar) formation. Of specific interest is the transition which takes place during the evolution from proto-stellar to main-sequence states.

Activity, as manifest by variations in radiative output on both short and long timescales, characterizes the Sun and other stars of similar size/age to our Sun. Such variations are manifest in all wavelengths from variations in X-ray coronal emission, to optical photospheric/chromospheric signatures of sun/star spots and plage, to radio signals from solar storms (see van Driel, p95). The signatures of activity as measured in these varied wavelengths is a common thread in solar and stellar physics, the Sun providing a close-up view of the emission sources, (see Nitta, p117; Schmieder, p57; Knaack *et al.*, p45) and the stellar neighbors providing variety and extreme examples for comparison with the solar case.

Magnetic fields are the most profound common thread. Magnetic fields act like "flies on a pole" to transfer angular momentum in tidally locked binary systems (see Maceroni *et al.*, p15), and during stellar formation. Yet closer to the stellar surface we now know that fields which have been twisted so as to carry excess energy provide the likely source of solar energetic phenomena such as flares and coronal mass ejections (see van Driel-Gesztelyi, p95). By extension and Occam's razor, we infer that this process is the basis for similar events observed in solar analogue stars.

Again, the Sun is our fiducial, due to the fact that we can resolve spatial detail from its photosphere up through its corona. We can discern the emission processes at different temperatures and wavelengths, and from these observations determine power-laws or other scaling rules which then serve as proxies for interpreting the observations of unresolvable objects (see Matthews *et al.*, p53; Oláh, p25). We know from solar observations that magnetic fields are manifest on the Sun's photosphere at the smallest scales and the largest spotted active regions. Hence, the photometric changes brought on by large magnetic flux concentrations are key diagnostics to placing the Sun amongst active stars, and *vice versa* (see Oláh, p25; Knaack *et al.*, p45).

Both modeling efforts and observational capabilities have advanced now to where solar and stellar astronomers can compare notes most easily. Modelers and observers can now challenge each other with predictions and counter-examples. We have seen this here in the presentations by Antiochos, Schmieder, Démoulin, Leka, and Knaack.

As for this meeting, the talks and posters have sparked questions over toasts of Tockaj and discussions over delicious bowls of goulash. No doubt at least a few pieces of future research will be guided and pushed by the presentations we have heard and seen.

But to the eclipse! For millennia, humans have observed the sun and gazed at the stars partly because of their intrinsic beauty. The total solar eclipses visible on the Earth violate the principle universality to some degree, for it is a rare coincidence that our Moon and Sun are so close in size and have the exact orbital elements so as to produce the Diamond Ring, the visible prominences, and the spectacular vision of the corona. From the earliest observations of eclipses, solar physics was in part born - the naming of the chromosphere, the first observations of coronal mass ejections. Let us tomorrow stand in awe and appreciation of the universe around us as we watch and wonder at the last total solar eclipse of this century.

[And it was indeed spectacular, despite a thin cloud cover. Afterwards the wine and food flowed and plans began for the next total eclipse in 2001. Not a soul was disappointed, and most were completely spellbound. A fitting close to a very memorable meeting.]